BRNO UNIVERSITY OF TECHNOLOGY

VYSOKÉ UČENÍ TECHNICKÉ V BRNĚ

FACULTY OF MECHANICAL ENGINEERING

FAKULTA STROJNÍHO INŽENÝRSTVÍ

INSTITUTE OF AEROSPACE ENGINEERING

LETECKÝ ÚSTAV

URBAN AIR MOBILITY VTOL PERSONAL VEHICLE DESIGN

NÁVRH PILOTOVANÉHO VZNÁŠEDLA PRO URBAN AIR MOBILITY

MASTER'S THESIS

DIPLOMOVÁ PRÁCE

AUTHOR — Bc. Marek Polčák

AUTOR PRÁCE

SUPERVISOR — Ing. Robert Popela, Ph.D.

VEDOUCÍ PRÁCE

BRNO 2022

BRNO UNIVERSITY OF TECHNOLOGY
FACULTY OF MECHANICAL ENGINEERING

Assignment Master's Thesis

Institut:	Institute of Aerospace Engineering
Student:	**Bc. Marek Polčák**
Degree programm:	Aerospace Technology
Branch:	Aircraft Design
Supervisor:	**Ing. Robert Popela, Ph.D.**
Academic year:	2021/22

As provided for by the Act No. 111/98 Coll. on higher education institutions and the BUT Study and Examination Regulations, the director of the Institute hereby assigns the following topic of Master's Thesis:

Urban Air Mobility VTOL personal vehicle design

Brief Description:

Main goal is conceptual design of Urban Air Mobility VTOL personal vehicle combining features of multicopter drone and motorbike. Structural design and analysis of main frame shall be performed. System level components selection and their integration analysis, control and stability, performance analysis shal be performed as well. Particular analysis and design of control system is important task to be performed.

Master's Thesis goals:

Recherche of existing Urban Air Mobility concepts, selection of components, design and structural analysis of frame, weight and balance analysis, performance and stability analysis, design of control system.

Recommended bibliography:

QUAN, Q. Introduction to Multicopter Design and Control. 2017. ISBN 9789811033827. Dostupné z: doi:10.1007/978-981-10-3382-7.

LEISHMAN, J. G. Principles of helicopter aerodynamics. Second edition.; Reprinted. Cambridge: Cambridge University Press, 2008, xxxvii, 826 stran : ilustrace. ISBN 978-1-107-01335-3.

BOUABDALLAH, S.,SIEGWART R. Full control of a quadrotor. In: 2007 IEEE/RSJ International Conference on Intelligent Robots and Systems [online]. IEEE, 2007, s. 153-158 [cit. 2020-10-20]. ISBN 9781424409112.

RAYMER, D.,P., Aircraft Design: A Conceptual Approach (Aiaa Education Series), American Institute of Aeronautics and Astonautics, ISBN-13: 978-1600869112.

Deadline for submission Master's Thesis is given by the Schedule of the Academic year 2021/22

In Brno,

L. S.

doc. Ing. Jaroslav Juračka, Ph.D. Director of the Institute	doc. Ing. Jaroslav Katolický, Ph.D. FME dean

ABSTRACT

The thesis deals with a conceptual design of a rotorcraft in the configuration of a multicopter, which has the design features of a motorcycle. Initial input parameters and requirements for conceptual design were based on statistical research of similar existing concepts. Afterwards, suitable components of propulsion system were chosen to fit the proposed design and flight performance requirements. UAM vehicle was designed as a coaxial quadcopter. Multicopter was designed as a composite construction combining aluminium space frame and composite ducts, which cover the propellers. Centre of gravity was calculated to ensure that its position lies exactly between front and rear rotors, which has a significant impact on stability. Structural strength of important components was then checked using FEM. Besides the structural analysis of a space frame, great deal of emphasis has been placed on structural analysis of composite ducts. This analysis helped to define inner structure and ensure that it withstands given load. Since the multicopter may benefit from ground effect benefits, its impact was evaluated by CFD analysis in three different distances from the ground. Positive influence of ground effect was evaluated based on extended battery endurance at hover for different payloads. Forward flight performance of designed UAM VTOL vehicle was carried out together with the estimation of drag coefficient of the multicopter with a pilot using CFD for different pitch angles. Obtained drag coefficient were then used for the calculation of multicopter forward flight speed dependency on pitch angle and battery endurance. In the end, two proposals of flight controller were presented together with possible control system and sensors, which could be used.

Keywords

UAM, VTOL, Multicopter, Conceptual design, Composites, FEM, CFD, Ground effect

ABSTRAKT

Diplomová práce se věnuje koncepčnímu návrhu pilotovatelného prostředku pro UAM. V průběhu návrhu byla vyvíjena snaha zachovat původní myšlenku létajícího motocyklu, což vedlo ke zvolení konfigurace multikoptéry. Na základě statistického průzkumu stávajících konceptů a vstupních požadavků bylo možné odhadnout vstupy pro první iteraci návrhu propulzního systému, který sestává z výběru vrtulí, motorů, kontrolérů a předběžného návrhu baterie. Nakonec byla zvolena konfigurace koaxiální kvadrokoptéry.

Klíčovou částí koncepčního návrhu je samotná konstrukce, která je navržena jako prutový duralový rám s krytovými prvky z uhlíkového kompozitu. Motory s vrtulemi jsou uchyceny v nosných prstencích, které přináší aerodynamické a konstrukční výhody. Tyto prstence jsou také navrženy z uhlíkového kompozitu, jejichž vrstvová skladba byla navržena tak, aby dokázala bezpečně přenést dané zatížení.

Pevnost navržené prutové konstrukce a kompozitních prstenců byla poté zkontrolována pomocí výpočtu metodou konečných prvků. Pevnostní analýza prutové konstrukce pomohla snížit celkovou hmotnost úpravou průřezu použitých kruhových profilů. MKP analýza kompozitního prstence byla provedena pro dynamické zatížení při přechodu do dopředného letu a byla klíčovým nástrojem pro definici vhodné skladby laminátu kompozitních prstenců tak, aby se docílilo kompromisu mezi hmotností a dostatečnou pevností. Největší důraz musel být kladen na napojení prstenců na centrální prutovou konstrukci, jelikož je využito mechanických spojů, které vytváří silné koncentrátory napětí. V těchto místech bylo zapotřebí silně zesílit laminát a využít zalaminovaný duralový plát, jenž pomohl zvýšit pevnost v těchto místech. Kromě kompozitních dílů prstenec využívá duralové součásti, které byly také zkontrolovány výpočtem.

VTOL prostředky mohou silně využívat výhod přízemního efektu. K výpočtu letových výkonů ve visu s vlivem přízemního efektu, byla provedena CFD analýza. Vliv přízemního efektu byl zkoumán ve visu ve třech různých vzdálenostech od země. Vliv přízemního efektu na letové výkony byl vyhodnocen na základě výdrže baterie ve visu, pro který je třeba generovat menší tah a spotřebovávat méně elektrické energie, než by bylo třeba ve větší vzdálenosti od země. Druhá část aerodynamických výpočtů se věnovala určení součinitele odporu v dopředném letu, jenž byl zkoumán ve třech různých naklopeních. Výsledky byly dále využity pro výpočet závislosti rychlosti letu na úhlu naklopení, výdrže baterie a dolet.

V závěrečné části práce byly navrženy dva možné způsoby provedení řízení a bylo shrnuto přístrojového vybavení, které by umožnilo bezpečný let.

Klíčová slova

UAM, VTOL, Multikoptéra, Koncepční návrh, Kompozity, MKP, CFD, Přízemní efekt

BIBLIOGRAPHIC CITATION

POLČÁK, Marek. *Návrh pilotovaného vznášedla pro Urban Air Mobility* [online]. Brno, 2022 [cit. 2022-05-15]. Dostupné z: https://www.vutbr.cz/studenti/zav-prace/detail/137148. Diplomová práce. Vysoké učení technické v Brně, Fakulta strojního inženýrství, Letecký ústav. Vedoucí práce Robert Popela.

DECLARATION

I declare that this thesis is the result of my own work under the guidance of my supervisor and all literature and electronic sources used for the research are cited in the list of literature.

In Brno, 19th May 2022

.....

Marek Polčák

ACKNOWLEDGMENT

I would like to thank my supervisor Ing. Robert Popela Ph.D. for his guidance and valuable tips during my work on the thesis, Ing. Jan Šplíchal Ph.D. for his support during FEM structural analysis, Ing. Robert Grim for his help during preparation of mesh for CFD analysis. Another thanks belongs to Ing. Tomáš Mejzlík for giving me an opportunity to work in his company and evolve my knowledge of propeller aerodynamics.

The biggest thanks belong to my family for all the help and support during my university studies and to my girlfriend Helena Kotoulová for her support and patience.

Contents

1 A BRIEF HISTORY OF ROTORCRAFT

The dream of flying filled a human mind since the ancient times and through the history the dreams became reality. Since the birds are using their wings to fly, another possible approach for generating lift, using rotational movement of propellers, was for centuries far beyond human understanding. Reasons were not only the lack of understanding but also the unsuitable technology, as Igor Sikorsky proposed in his autobiography. Even though a sign of usage was in ancient China in the form of feather toys similar to the principle of maple seeds, as a first conceptual design of a rotorcraft was created by Leonardo Da Vinci in the end of 15th century. Even though the concept itself was unrealizable, it showed a significant improvement of aerodynamics understanding. Literal notes describe its movement by *"rotation with speed screw boring through air and climbing high*". Design showed the understanding of principle of light-weight structures at lower air density compared to water.[1]

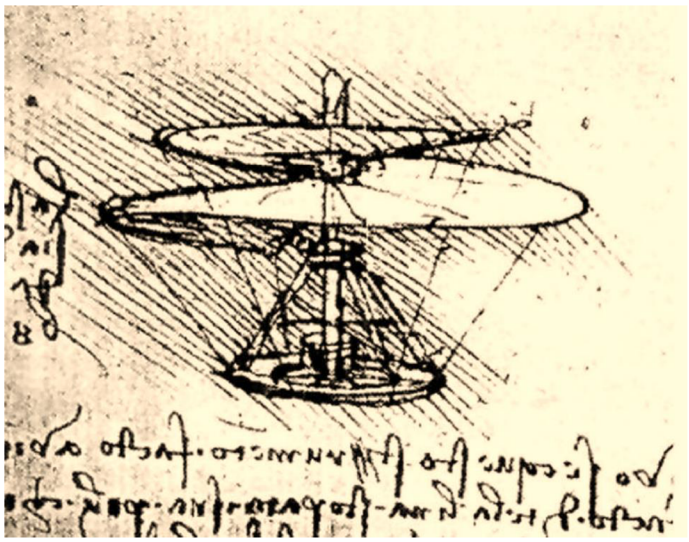

Figure 1.1 Conceptual design of helicopter by Leonardo da Vinci [1]

After centuries without known practical research in the art of flying beside the air balloons came in the 20th century with the first flights of heavier-than-air aircrafts. The first manned flight happened in 1903, when the Wright brothers flew 120 feet with their Wright Flyer. Four years later, French inventor Paul Cornu performed first vertical flight, which was achieved with a relatively simple construction consisting of two rotors actuated by a combustion engine. Until 1930s there were several attempts of vertical flights, but all projects suffered from non-existence of powerful engine. First success with the rotorcraft was the Juan de la Ciervas's Autogiro, which made a flight across English Channel using exclusively the autorotation for vertical thrust generation. After the engines improved, autogyros began to be outshined by helicopters, since they began to show their advantages. One of the first commercially successful helicopter was Sikorsky R-4, designed by Igor Sikorsky, who worked with the rotorcraft principle since the beginning of 19th century. This helicopter was the first successful aircraft with the tail rotor, which prevailed over other configurations of rotorcraft until today.[1]

Multicopters are nowadays used for various purposes and are taken as an innovation of 21st century. In the last decade, multicopters capable of carrying bigger payload are being designed

and they are in several ways similar to a concept, which came to existence already in the year 1958, when the U.S. army announced a competition for a design of Flying Jeep. Several companies applied to this competition. Curtiss-Wright created possibly a first coaxial quadcopter VZ-7, which could be seen in the picture below, and another companies, like Chrysler came with a concept of the dualcopter. These concepts were not used in action and these concepts ended up in a drawer. A possible reason of cancelation was a difficult distribution of the combustion engine power.[2]

Figure 1.2 Curtiss -Wright VZ-7 Flying jeep [2]

Nowadays, a concept of multicopter is coming back to the fashion, since there is a plenty of small quadcopters almost anyone can afford. Rising popularity of these aircrafts is possible due to the affordable and available components and also the technological progress in computer technology. With the increasing size of electric motors, controllers and batteries, multicopters are capable of carrying heavier loads equal to the weight of several people. New concept of transportation called Urban Air Mobility (UAM) is emerging rapidly and it is expected to be a direct competitor to small helicopters and ultralights.

2 URBAN AIR MOBILITY (UAM)

Traffic jams in the crowded cities are undesirable parts of our lives and a possible way out is UAM. UAM aircrafts are designed for the air movement in the city to shorten the traveling time. In the streets of a metropolis there is not enough space for conventional airplanes, which need long runways to take off and land, because of that the VTOL (Vertical Take-Off and Landing) concept is highly beneficial and is used by the majority of UAM projects. However, several approaches are used for the forward flight as following picture shows. After vertical take-off, VTOL aircraft can be designed as winged aircraft with vectored thrust, which means that all rotors tilt for cruise phase. Some of the concepts use some rotors only for VTOL phase and afterwards use only few of them for forward flight. Both approaches may use a beneficial impact of distributed propulsion. Last and very common possibility is to use a multicopter concept.[3]

Figure 2.1 UAM types from the propulsion system perspective [3]

However, passenger transportation is not the only application, which UAM projects focus on. Scope of several projects is on emergency vehicles, which could save lives because of faster transport of injured or sick people into the hospital. At the situations of fire or other disaster UAM vehicles may be used for firefighting or observation of the incident area.[3]

Safety is a main concern due to the aerial movement over the crowded areas. Therefore, for the UAM platforms, a special corridor is considered. UAM concepts should be also possible to prove their reliability. In order to protect the pilot, maximal speed should be limited by design parameters or the flight controller and the aircraft should possess advanced avionics, which would control the aircraft in dangerous situations to prevent a tragedy. Another disadvantage which is connected with UAM is the noise, which may disturb the inhabitants. Main noise generators of the VTOL aircrafts are the propulsions systems, even though they use usually electric motors, which are relatively silent in comparison with propellers, which generate the noise. Beside these attributes which may affect the reputation of UAM among the population is also a possible loss of privacy and unaffordability as a survey showed.[3]

Designing a safe UAM vehicles should be a main concern, but building a reliable infrastructure for safe landing spots is also very important. UAM can pay off mainly in bigger cities, which are better prepared for the application. Survey results from [3] show that Prague is a seventh most suitable city in Europe for UAM. Main reasons, why a city is more suitable than other, are given by the usability of UAM for airport shuttle, possible sightseeing use, first aid use case and other. Statistical research of multicopter existing UAM concepts was performed and is summarized in chapter 5.

3 INITIAL CONSTRUCTION AND FLIGHT PERFORMANCE REQUIREMENTS

Conceptual design of any aircraft unfolds from the requirements, which should be defined in the beginning of designing process. VTOL aircraft may be designed several ways, but in this work a purely hovering rotorcraft will be considered to meet the initial idea of a flying motorbike, which will be resembled mainly by the seating position of a pilot. The following table lists the input requirements for the design and flight performance on which the design itself will be based. Three payload variants were taken into account to make the aerial vehicles suitable for the majority of population.

Table 3.1 Initial construction and performance requirements

Number of passengers	1
Payload variant 1	100 kg
Payload variant 2	85 kg
Payload variant 3	60 kg
MTOW (estimated from statistics)	300 kg
Empty weight (estimated from statistics)	150 kg
Maximal speed	30 m/s
Battery endurance	20 min
Maximal ceiling	50 m

3.1 Flight mission

UAM projects are usually designed for the exact flight missions, which can be relatively complex, since the city does not offer enough suitable spaces for safe landing, so it is important not to forget this important factor. UAM project should be designed preferably to shorten the travelling time, which should be significantly lower, than the time spent in the car. Flight mission has to be also deriving the flight range and speeds generated by the conventional public transport.[3]

NASA presented a study, which describes several flight mission models. Differences between them are in the flight range and payload. Aircraft designed in this thesis would fit in the first proposed flight mission type, which is represented as a one passenger commuter with a bag from outskirts of a city to its centre and back. [4]

UAM vehicle designed in this work suits a short mission. Following picture depicts the distance diameters around Brno to represent the flight ranges. Designed eVTOL should not have any problem to operate in the blue circle. On the other hand, green and red circles are covering densely populated areas. Danger of flying over these areas brings several limitation and additional requirements, which are described in the chapter 6.

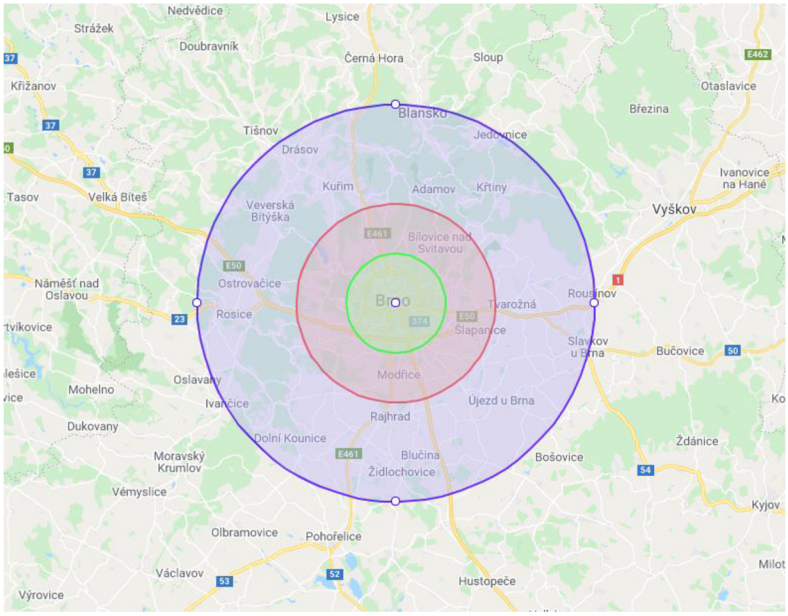

Figure 3.1 Distance diameters around Brno (5 km, 10 km, 20 km)

Altitude of a cruise phase may be different, since it can be expected that aviation authorities will determine safe altitudes for UAM vehicles and in other altitudes the aerial movement will be banned or reserved for other aircrafts. Federal Aviation Administration (FAA) has already proposed the distribution of aerial space and divided it to three altitudes. Beside the general aviation altitude also proposed a special altitude for UAM and Unmanned Aircraft systems (UAS).[3][5]

Following picture depicts the proposed flight mission inspired by [4]. After the vertical take-off to the altitude, which is considered as safe for the flight throughout the city, multicopter moves forward to the target location. Flight mission should also take into account transition phases, but it basically does not apply for multicopters, whose transition is relatively fast. However, the movement in the city may be a dangerous task for a pilot and also for his surroundings, so it is important to count with an obstacle, which should be overcame fast enough to be safely trespassed. Another possible flight mission could into account a low level flight, which would be the most efficient for multicopter. However, this flight mission would have to be performed at safe area.

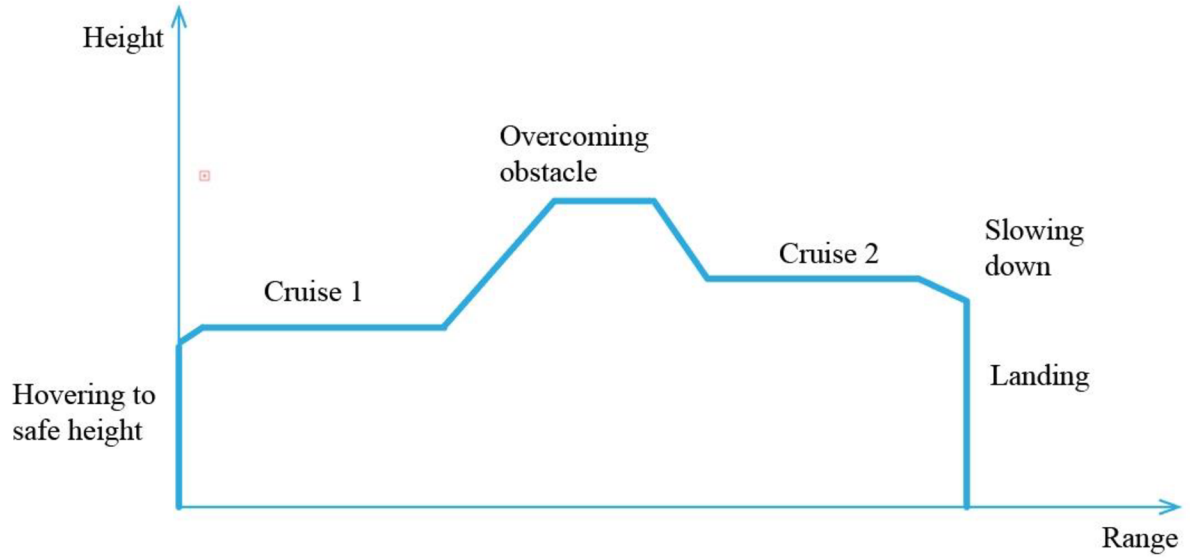

Figure 3.2 Proposed model flight mission

4 INTRODUCTION TO MULTICOPTERS

Multicopter is a rotorcraft, which uses multiple propulsion systems to generate thrust needed to overcome gravity and make complex maneuvers possible. Multicopters doesn not contain any mechanical control mechanism and their air movement depends on the differentiation of propeller speeds. Unlike the conventional helicopters, multicopters do not need a tail rotor, which compensates the torque generated by the main rotor. To eliminate this torque inequality, multiple rotors rotating in different directions are used.[6]

4.1 Basic principle of multicopter movement

Since the multicopters have usually fixed propellers without a possibility of changing the pitch, the only way how a multicopter may maneuver is by changing the motor speeds independently. In order to generate the longitudinal or lateral movements, a multicoter has to tilt first, so the thrust forces act in the desired way. In order to make the multicopter stable, it is needed to differ the senses of rotation, so the torque equilibrium is achieved. Usually said, the rotation on the quadcopter diagonal are in the same sense. For multicopters with other motor configurations which are also listed in this chapter, it is more complicated.[6]

Four different aerial maneuvers may be distinguished. Usually, the multicopter maneuvers in compound movement, which is the combination of these basic motions. The distribution of thrusts and moments torques for generating these various maneveurs of quadcopters is described below. Resultant air movements highly depends on the flight controller, which makes a thrust coupling possible. Pilot's command carries only the value of intensity of maneuvers and pilot does not have to control each motor separately, which would be very difficult, tiring and relatively slow. Flight controllers are discussed deeper in the last chapter of this thesis.

Hovering

Hovering is a movement in vertical axis. Multicopter changes its altitude by simultaneously rising or decreasing motor speed and therefore the propeller thrust increases. Following picture depicts hover flight, where magnitude of rotational frequency is represented by the size of arrows and their colour represents their direction.

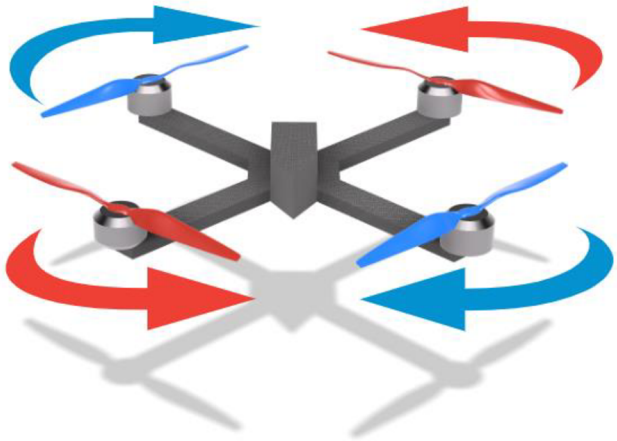

Figure 4.1 Quadcopter at hover

Pitching

Pitching movement makes forward and backward motion possible. It is obtained by different value of rotational speeds of the front pair of propellers and rear pair propellers. As following picture shows, during the forward flight, rear propellers have to generate higher thrust compared to front propellers.

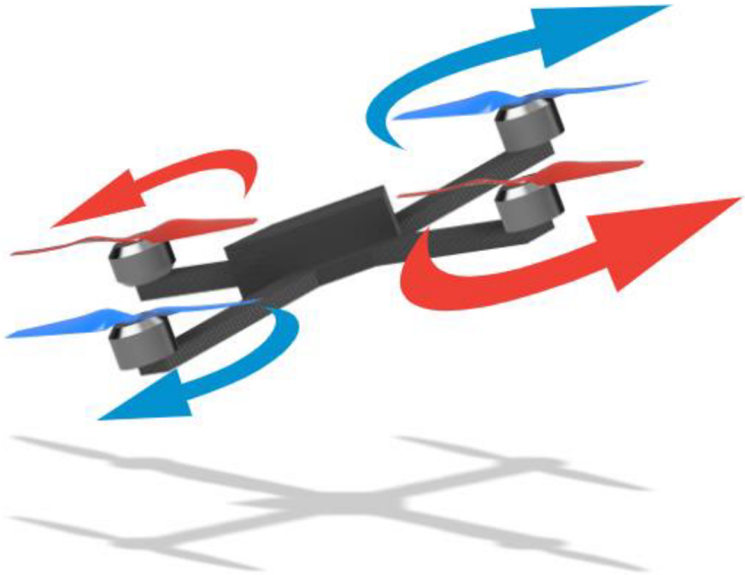

Figure 4.2 Quadcopter at forward flight

Rolling

Rolling motion may be described as a lateral motion of the multicopter, since it helps the multicopter moves left and right. The propellers of the left pair have to rotate at lower speeds than the right pair to tilt and move to the left, which is represented in the following picture.

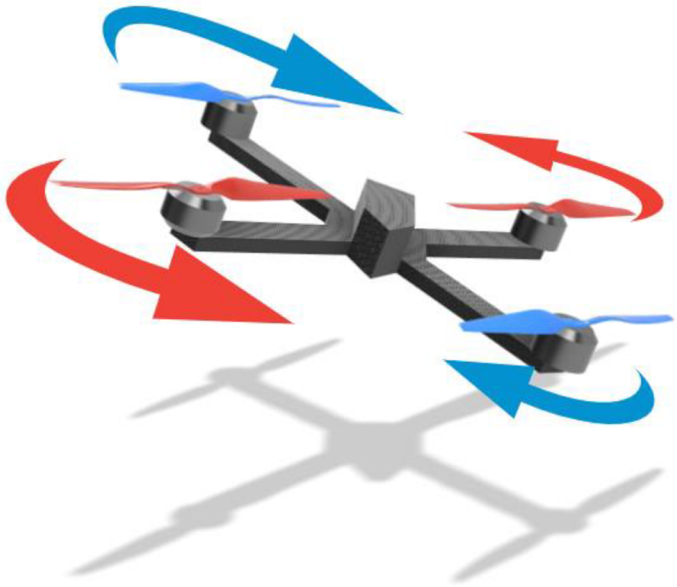

Figure 4.3 Quadcopter at leftward flight

Yawing

Yawing motion is the result of the different propeller torques. The rotor speeds of the same orientation have to differ from the other pair of rotors to create the difference in the resultant torque, which rotate the multicopter without any pitching or rolling as following picture shows.

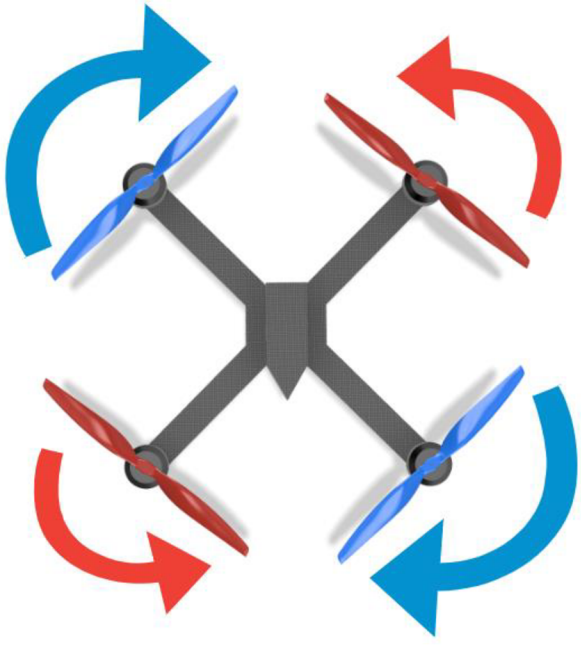

Figure 4.4 Quadcopter at counter-clockwise yaw

4.2 Types of multicopter configurations

Multicopter are designed for specific applications and each configuration has its advantages and disadvantages. Multicopter configurations are divided by the number of motors and its orientation to the multicopter body. Minimal number of rotors required to compensate other propeller torque is two. However, this configuration lacks stability, so this configuration is not the common. Following picture shows various multicopter configurations and also differentiates the rotation directions by different colours of rotors. Most common configuration is a quadcopter at the X configuration, which is means that a multicopter body is not parallel with the rotor diagonal. Tricopter configuration is sometimes chosen by designers, but this configuration has its stability and control disadvantages. Picture also shows more exotic configuration which are hexacopters and octocopters, which are also used in some cases. There is also a possibility of the usage of coaxial motors.[6]

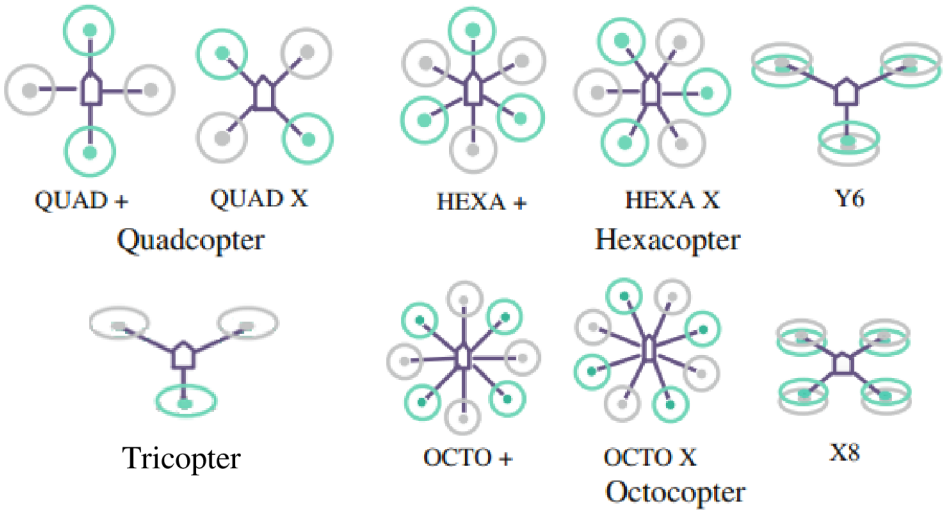

Figure 4.5 Overview of possible multicopter configurations [6]

Some of these configurations such as octocopter or hexacopter do not suit the intended concept, since in these configurations it would be difficult for a pilot to mount the multicopter. The best configurations for the intended purpose is a tricopter or quadcopter in X configuration, because in these configurations it is possible to place a seat better.

5 STATISTICAL EVALUATION OF EXISING CONCEPTS

In recent years, UAM projects for passenger transport have begun to emerge and already there is a large number of them today and they are mostly designed to transport more than one person. Based on existing multicopter projects for passenger transport for one to two people, statistics has been created to estimate some parameters, such as maximum take-off weight (MTOW), maximum power, maximum speed, or battery endurance. Following table clearly shows the characteristics of the individual projects on which the statistical outcomes were based. Unfortunately, some projects do not publish all the necessary data to help refining the statistics. Appended statistics contain acquired data from the end of 2020.

Table 5.1 Overview of statistical research data

Project name	Empty weight [kg]	Payload [kg]	MTOW [kg]	Maximal speed [km/h]	Number of motors [-]	Motor power [kW]	Total power [kW]
Assen A1	68	45	113	80.46	3	19	57
Assen A2 Avenger	114	90	204	101.4	3	19	57
Opener BlackFly	142	113	255	130	8	31.3	250.4
Hoversurf	114	114	228	96	4	33	132
Malloy hoverbike	105	165	270	96	2	40	80
EHANG 184	260	100	360	100	8	19	152
Flike	300	100	400	100	3	-	-
Kitty Hawk Flyer	113	91	204	48	10	-	-
DaVinci ZeroG	90	100	240	70	12	30	-
AirSPeeder MK4	310	90	400	160	4	12.5	100
teTra 3	-	-	-	100	4	-	-
Neva AirQuad	-	100	500	60	20	-	-
Red hummingbird	75	104	238	60	6	-	-
Jindouyun drone	-	-	-	72.4	8	-	-
Aerofex Aero-X	216	140	356	72	2	-	-

The statistical research also includes projects which are in the prototype stage and may therefore skew the results, but due to the small number of real projects in this category, prototypes and conceptual designs have also been included. In the charts are highlighted concepts that are already physically tested and comply with the idea of flying motorcycle. Their dimensions and performance were key pivot points in initial phase of the work. Based on the results of statistical research several UAM vehicle properties were estimated and were used for the initial design

iteration. However, some values have to be taken with reserve, since not all included projects are also in its conceptual phase and some of the values may be skewed.

5.1 Similar concepts

Following pictures show the most similar hovercrafts Assen A2 Avenger and Hovercraft Hoversurf, which are the closest motorbike-like looking concepts. Main differentiating factor of A2 Avenger are three ducted fans, which are aerodynamical beneficial. However, maneuvering and stability of tricopter is considered to be worse compared to quadcopters.

Figure 5.1 Assen A2 Avenger [7]

On the other hand, Hovercraft Hoversurf is a quadcopter with the rotors placed on the bottom of the frame. Several configurations with two and three bladed propellers exist.

Figure 5.2 Hoversurf Hovercraft for Dubai police [8]

5.2 Statistical evaluation

5.2.1 MTOW

From the following chart, the MTOW can be estimated based on the required payload.

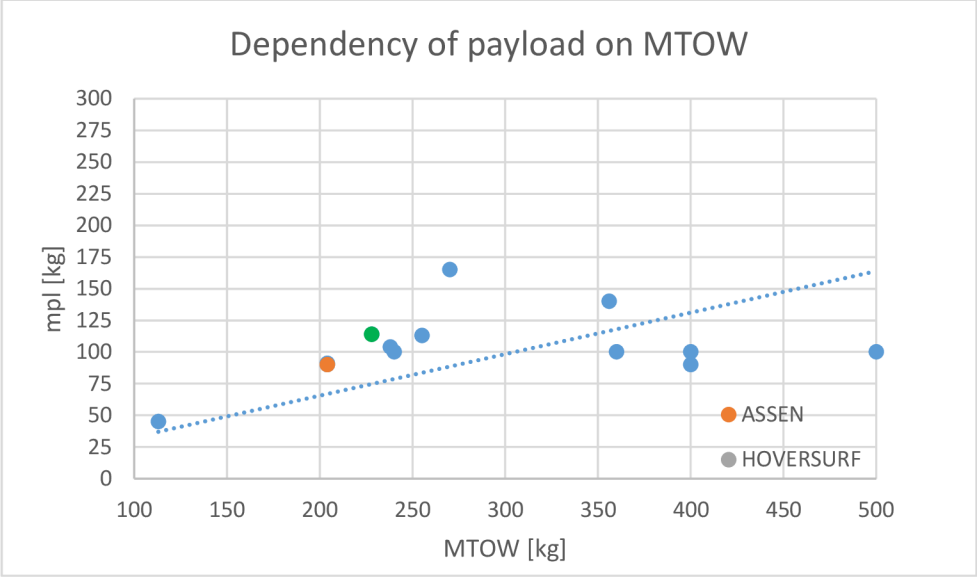

Figure 5.3 Dependency of payload on MTOW

Based on the interpolated curve, MTOW of the multicopter with the payload of 100 kg is expected to be around 300 kg.

5.2.2 Maximal total electric power

Estimated MTOW of the multicopter was used to preliminarily estimate the required maximal motor power.

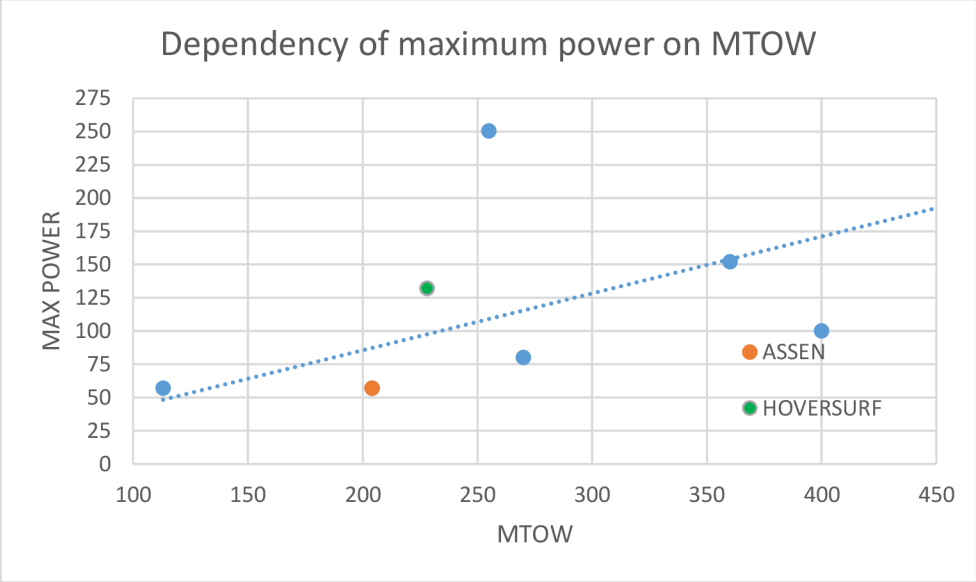

Figure 5.4 Dependency of maximal power on MTOW

It is expected that maximal total electric power to be around 125 kW.

5.2.3 Maximal flight speed

Maximal flight speed of some projects is intentionally limited for safety reasons. Based on the following dependency, maximum speed can be derived based on MTOW.

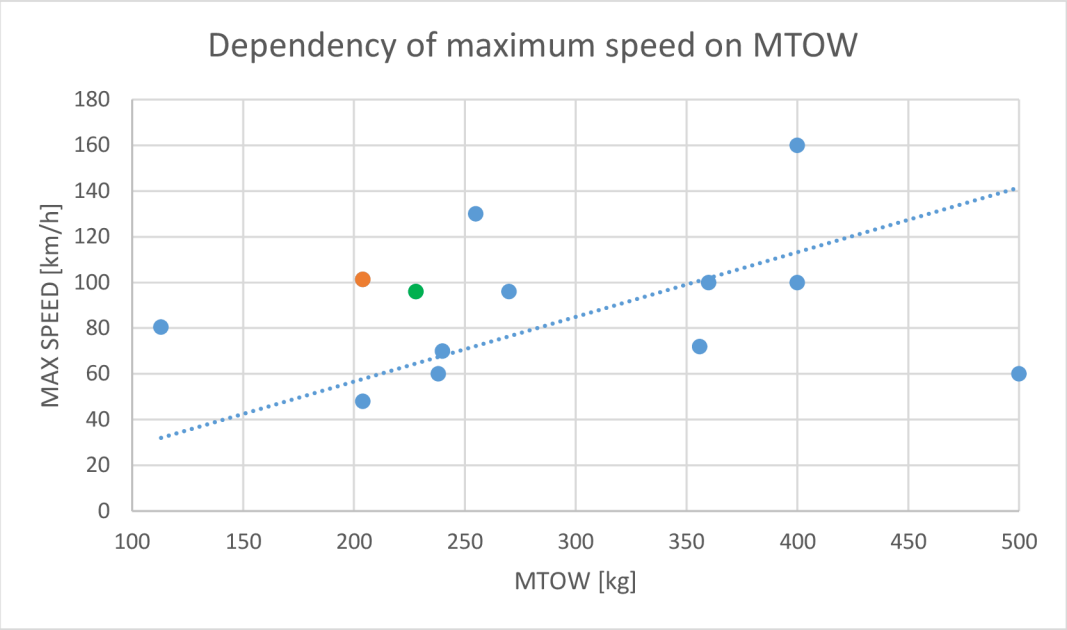

Figure 5.5 Dependency of maximal speed on MTOW

Possible achievable flight speed is expected to be around 85 km/h.

5.2.4 Battery capacity

Statistical research helped to predict the required battery capacity for a demanded endurance. To obtain more accurate estimation, statistics would have to also differentiate type of battery cells.

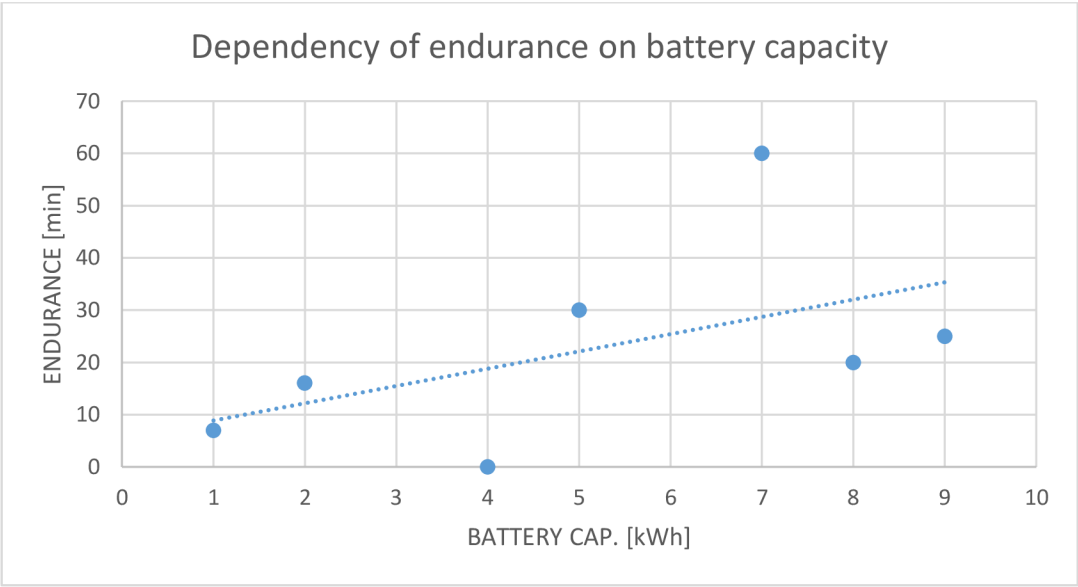

Figure 5.6 Dependency of endurance on battery capacity

For the required endurance of 20 min, battery with capacity of 4.25 kWh should be chosen.

6 AIRWORTHINESS STANDARDS

6.1 EASA Special condition and means of compliance

Since the UAM is a new emerging concept, there are not certification specifications defined yet and they are developed hand in hand with UAM projects, whose number in this rapidly increasing. EASA is creating the new standards partially by the communication with companies, which are developing UAM vehicles. EASA published a document Second Publication of Proposed Means of Compliance [9] with the Special Condition VTOL [10], which partially defines the requirements and recommendations for UAM projects.

Special condition divides VTOL aircrafts to two categories. Enhanced VTOL category aircraft is able to safely continue in flight in case of failure to alternative safe landing spot, so it allowed to fly over congested areas. Basic category aircrafts cannot continue in flight, so they have to immediately perform a safety landing in case of failure. Hence Basic category aircrafts cannot fly over congested areas.[10]

6.1.1 Structural design envelope

Every aircraft should have established design speeds. As [9] states, several design airspeeds should be taken into consideration. Maximum level flight speed at maximum continuous power. Never-exceed speed should not be greater than 0.9 times maximum design speed. Velocity of normal operation is the maximum structural cruising speed and should be less or equal to maximal level flight speed and never-exceed speed. Maximum design rearward and sideward speed differs these design speeds from conventional aircraft design speeds. This speed should be defined during the design. Positive and negative maneuvering load factors should be higher than 2 and lower than 0.5.[9]

6.1.2 Flight Load Conditions

VTOL aircraft should be able to withstand several situations and maneuvers, which are difficult to predict in the conceptual phase of the design. These flight loads cover unsymmetrical loadings due to thrust unit failure or take-off from sloped plane. Load factor introducing loads, like recoveries from maneuvers, which orientation depends on the maneuver type. Due to the complexity of simulation of multicopter flight, structural analysis in this work considered hover and artificial implementation of gyroscopic moment.[9]

6.1.3 Take-off performance

VTOL aircraft may use various take-off paths. Proper choice of the take-off pat his dependent on the pilot skills and also the surroundings and possible obstacles. First possible take-off path is Conventional Take-Off (ConvTO) and Elevated Conventional Take-Off (EConvTO), which differs from ConvTO only by the initial elevation to safer altitude. These two take-off paths are used by helicopters. After a performed maneuver, take-off safety speed V_{TOSS} is reached. At given altitudes of flight envelope, V_{TOSS} should be calculated for all weight configurations and critical centre of gravity positions. Another possible take-off path is Vertical Take-Off (VTO), at which the aircraft vertically takes-off to the safe altitude, from which can continue in forward flight. Schematic trajectories of take-off paths are displayed in the following picture.[9]

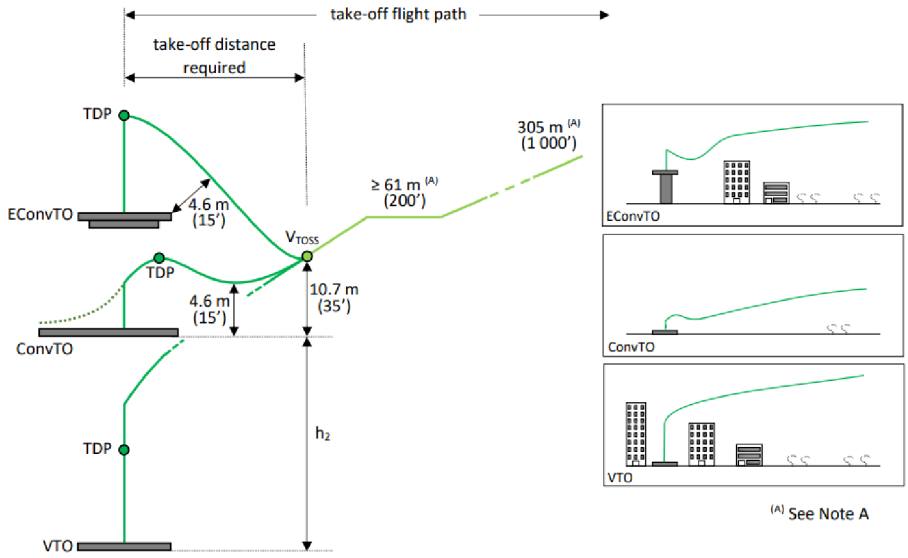

Figure 6.1 Different possible take-off trajectories [9]

6.1.4 Landing [9]

VTOL aircrafts may use also a conventional landing which differ from vertical landing by trajectory, which is not vertical since the aircrafts still keeps the forward speed. Vertical landing is beneficial at situations, when the pilot has to pass the obstacles. It could be considered as a safer option since the pilot may stabilize the aircraft in the higher altitude and then descent.

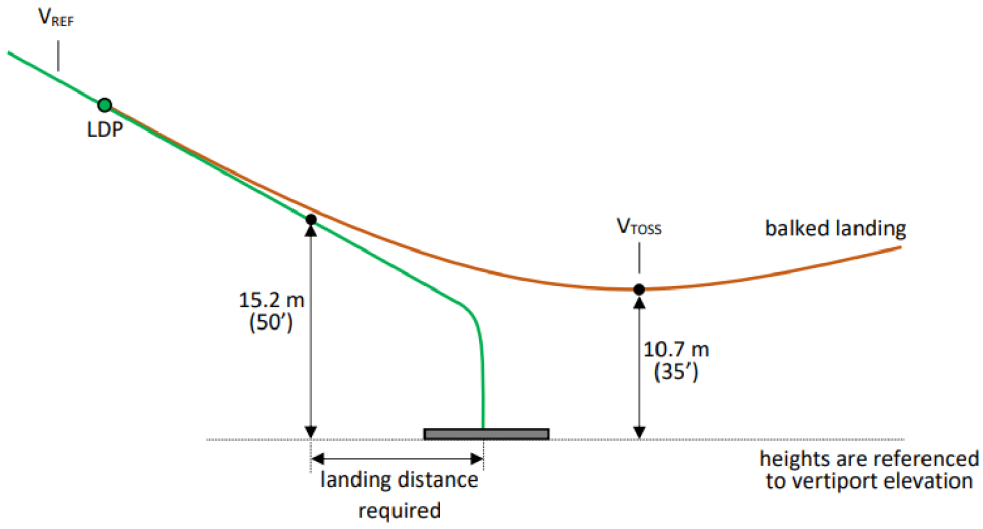

Figure 6.2 Various landing approaches of VTOL aircrafts [9]

VTOL aircraft should be also able to perform balked landing, which should be decided at the latest in the landing deciding point (LDP). At the defined altitude it should gain take-off safety speed and begin to climb at the certain climb gradient.

6.2 Certification Specifications for Small Rotorcraft – CS 27

Some chapters of the MOC-2 SC-VTOL link the CS-27 as a reference for several conditions, especially the structural strength and reliability section. Designed rotorcraft will follow some parts even though the maximal certified take-off weight of small rotorcraft may be up to 3175 kg and expected MTOW of designed rotorcraft is 320 kg.[11]

6.2.1 Flight loads

Certification Specifications distinguish between limit loads, which occur at the service and ultimate loads, which are limit loads multiplied by a factor of safety, which should be at least 1.5. Structure have to be able to withstand ultimate load for 3 seconds at static conditions without any failure. Defines the range of load factors between 3.5 to –1. Construction of the rotorcrafts should be able to sustain the loads for all weight configurations in this range of load factors.[11]

7 PRELIMINARY DESIGN OF THE PROPULSION SYSTEM

Propulsion system is a crucial part of any aircraft, as it takes care of creating the necessary thrust. Most concepts benefit from the apparent simplicity of the electric drive, which was also chosen for the design in this work. There are also projects with internal combustion or even jet engines, but they also have disadvantages. The electric drive consists of several components, which will be summarized in this chapter. Large number of these components is available on the market, so an filtering program has been created, which was mainly based on the references [6],[12]. With its help, the ideal propeller, engine, electronic speed controller (ESC) and batteries can be effectively selected based on comparison criteria from the created databases of suitable components.

7.1 Selection of propellers

Propellers make the flight of the UAM vehicle possible since they generate needed thrust. Hovering aircrafts are highly dependent on the propeller performance because there is not a possibility of gliding, which fixed-wing aircrafts rely on.[1]

7.1.1 Propeller diameter

Since the propellers of can be simplified by using momentum theory to ideal actuator disk, which is defined only by its diameter, it is possible to evaluate appropriate propeller diameter without defined propeller geometry. In the conceptual design phase, it can help designers to quickly valorise the size of rotors.[1]

Required thrust at the hover mode, which is equally divided to all of the propellers, as can be seen in the following equation [6].

$$T_{\min} = \frac{MTOW}{n_r} = \frac{250}{8} = 31.25\,kgf \tag{7.1}$$

Disk loading of the proposed configuration is calculated directly as division of required thrust T_{min} by disk area A.[1]

$$DL = \frac{T_{\min}}{A} = \frac{T_{\min}}{\pi \frac{D_p^{\,2}}{4}} \tag{7.2}$$

Hovering aircrafts should have the disk loading the lowest as possible to increase the propeller efficiency, because propellers with lower disk loading require lower power to generate the required thrust. In some cases, the disk loading may be bigger even for hovering aircraft. However, the power consumption rises and then hand in hand flight endurance lowers. Recommended disk loading for multicopter is in the range of 24÷48, so the chosen propeller diameter should be able to generate enough thrust efficiently from this point of view.[1]

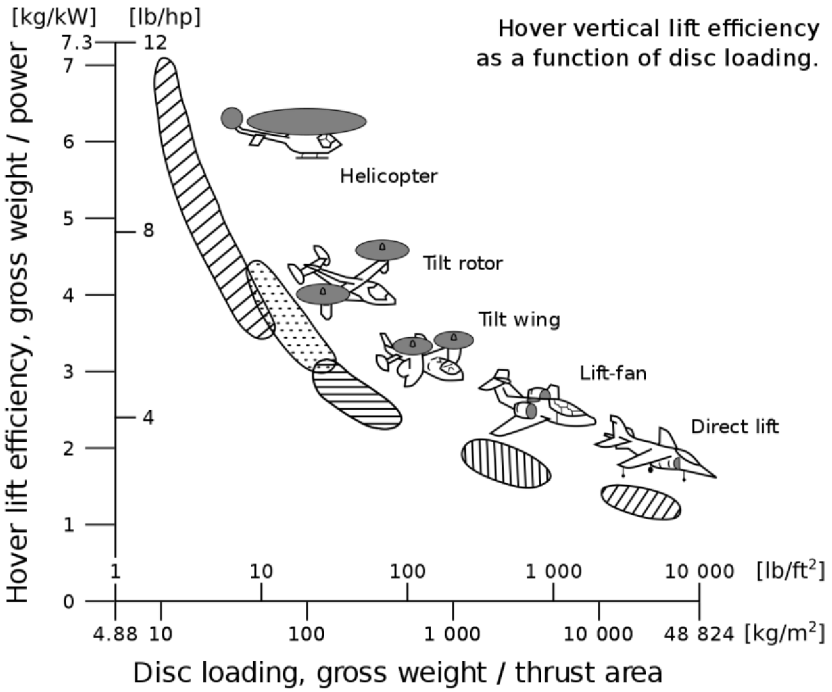

Figure 7.1 Disk loading of various aircraft configurations [13]

By combining previous two equations, a following formula for the calculation of ideal disk can be derived.

$$D_p = \sqrt{\frac{4 \cdot MTOW}{\pi \cdot DL}} \tag{7.3}$$

$$D_p = \sqrt{\frac{4 \cdot 31.25}{\pi \cdot 30}} = 1.15\,m \tag{7.4}$$

From the point of view of overall size of the aircraft, smaller diameter should be always better, because it is lighter and more compact, but on the other hand, it is not as efficient as a larger diameter propeller, because it generates lower induced velocities and induced power requirements. Trade-off between the geometric, weight and propeller power had to be made.[1]

As any aircraft, multicopters should have a power reserve, which is used for maneuvering. Since the only the thrust of the propellers makes the aerial movement possible, a power reserve is represented by thrust to weight ratio, which differ for different types of multicopters. Recommended minimal thrust to weight ratio for multicopters is 2 and for payload transport is recommended 3. These values are difficult to maintain in bigger scale concepts, which require also require improved structural strength and durability. Chosen thrust to weight for the initial dimensioning of propulsion system was 1.5. Disk loading in the maximum throttle will also be 1.5 bigger, but it is expected that flight phases with maximal thrust cover minor occurrence at flight envelope.[1][12]

7.1.2 Propeller tip speed

Larger diameter increases the tip speed, which has mostly a negative effect on the propeller performance. At higher propeller speeds unwanted because of compressibility effects occur and generate additional drag, which may compensate the benefits of stored rotational kinetic energy. However, higher tip speeds also result in bigger noise, which is undesirable for UAM, since the noise of the aircraft should be low as possible. Compressibility effects may be partially supressed by thinning the airfoil or tuning the tip shape, if we want to use larger propeller diameter.[1]

7.1.3 Number of propeller blades

In the cases when the two bladed propeller is not capable of generating required thrust thus increase the solidity ratio, which describes how much big area the propeller blades cover from the ideal actuator disk, number of blades may be increase the solidity ratio to be able to generate more thrust. Efficiency of the three bladed propeller is lower compared to two bladed propellers. However, increased number of propeller blade has beneficial effect on propeller noise, which is lowered because tip vortices are weakened.[1][14]

7.1.4 Estimation of propeller thrust and torque

Even the propeller diameter was chosen at the previous subchapter, the propeller geometry differs, and it is difficult to calculate them, since the geometry is mostly known only by the manufacturer.

In order to choose the most suitable propeller it would be necessary to have the data from static and dynamic test of the propeller. Unfortunately, this data cannot be obtained for all propellers. In the filtering program, the propellers were filtered based on analytical calculations of propeller characteristics, for the calculation of which the relations from [6] were used.

$$T = c_T \rho \left(\frac{N}{60} \right)^2 D_p{}^4 \tag{7.5}$$

$$M = c_M \rho \left(\frac{N}{60} \right)^2 D_p{}^5 \tag{7.6}$$

Thrust coefficients c_T and torque coefficients c_M are determined with difficulty. However, there are the empirical equations for their calculation. These equations are valid for smaller quadcopters, but if the coefficients are chosen appropriately, the calculated thrust and power characteristics correspond to the characteristics of the propellers of the corresponding dimensions obtained from the static tests.[6]

$$C_T \doteq 0,25\pi^3 \lambda \xi^2 B_p K_0 \frac{\varepsilon \arctan\left(\frac{H_p}{\pi D_p} - \alpha_0 \right)}{\pi A + K_0} \tag{7.7}$$

$$C_M \doteq \frac{1}{8A} \pi^2 C_d \xi^2 \lambda B_p^2 \tag{7.8}$$

$$C_d = C_{fd} + \frac{\pi A K_0^2}{e} \frac{\left(\varepsilon \arctan\left(\frac{H_p}{\pi D_p} \right) - \alpha_0 \right)^2}{\left(\pi A + K_0 \right)^2} \tag{7.9}$$

Coefficients A, ε, λ, ζ, e, C_{fd}, α_0, are dependent on the propeller geometry, so it is difficult to determine, so they were estimated and adjusted to correspond as closely as possible to the values from the static test data. In the following picture, static performance of the propeller Mejzlik 48x16.4“, from the Czech manufacturer is compared in this way. The average deviation is 7.6 %. It is important to mention that the propeller coefficients are different for each propeller and in the comparison program they were not alternating. Therefore, the propeller characteristics of some propellers may differ from the static test data. These deviations do not affect the comparison process. For the further calculations of flight performance, measurement data were used.

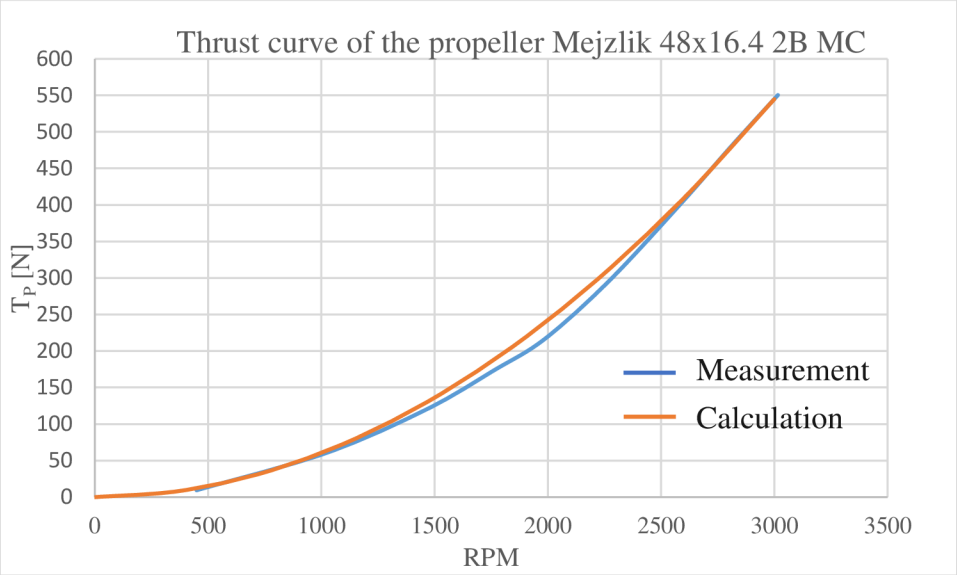

Figure 7.2 Comparison of analytically calculated thrust curve with measured static values

The most suitable propeller was selected based on the lowest power required to create the minimal thrust required. The minimum required thrust is plotted in thrust curves, from which the speed corresponding to this power is determined for each propeller. The propeller power can then be determined from these speeds.

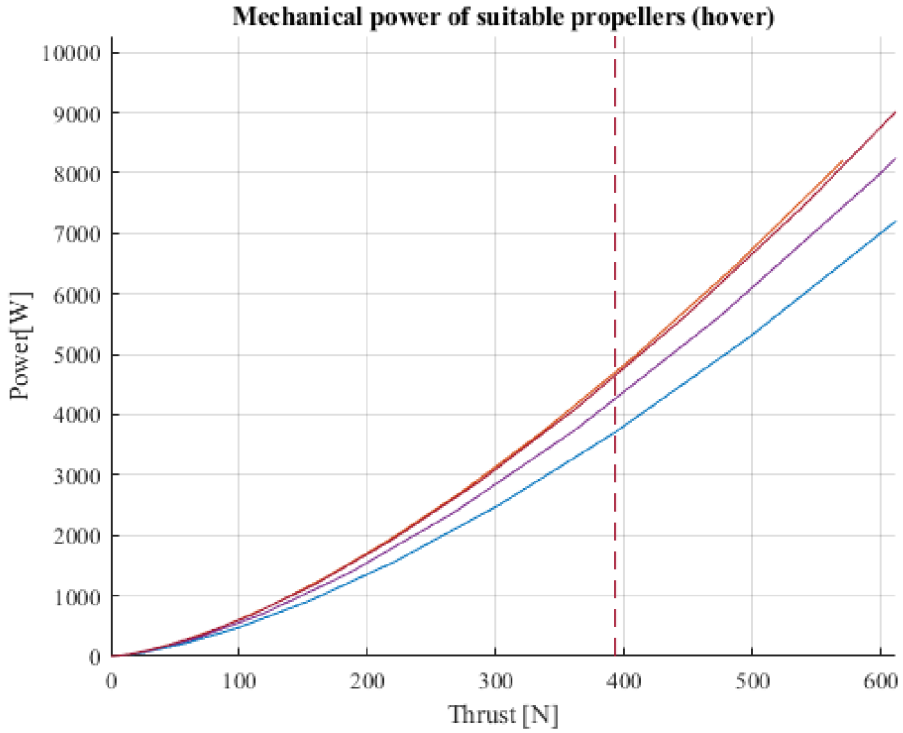

Figure 7.3 Mechanical power of suitable propellers

Out of the database of propellers, Mejzlik 48x16.4 2B MC was chosen as the most suitable propeller.

7.2 Selection of motors

In order to generate the required rotational speed and torque to run the propeller, the right motor has to be chosen. The most commonly used motors for multicopters today are the brushless direct current (BLDC) motors, because of their higher effectivity and higher reachable speeds. Since the brushless motor lacks the brushes, which may wear-off, they their lifetime is much longer in comparison to the brushed DC motors. Today, there are already motors of this type that can develop relatively large power values, reaching up to 200 kW.[15][16]

BLDC motors consist of permanent magnets placed on the rotor and the coils are usually winded up in the iron core of the stator. Based on the rotor construction, motors can be divided to inrunners and outrunners. Following picture shows inrunner configuration, so the rotor with permanent magnets are placed on the inside and usually only the outer motor shaft rotates. Outrunners have permanent magnets on the rotor rotating around inner stator. Rotation of the motor is covered by generating the rotating magnetic field, which is achieved by electronic commutation with electronic speed controllers (ESC). ESC activates motor phases by driving current into windings, which generate magnetic field interferencing with permanent magnet. After this rotation step, controller has to know the position of the rotor, which is secured by hall sensors, which gives a signal to activate following motor phase. [15][16]

A database of motors was created, for which it was necessary to know their electrical properties such as optimal motor voltage U_M, maximal motor voltage U_{Mmax}, maximal peak current I_{Mmax}, and K_{v0} value, which describes how much rotational speed can a motor rotates at the given

voltage. Another important characteristic describing the BLDC motor is internal electrical resistance R_m, which is difficult to estimate.[15]

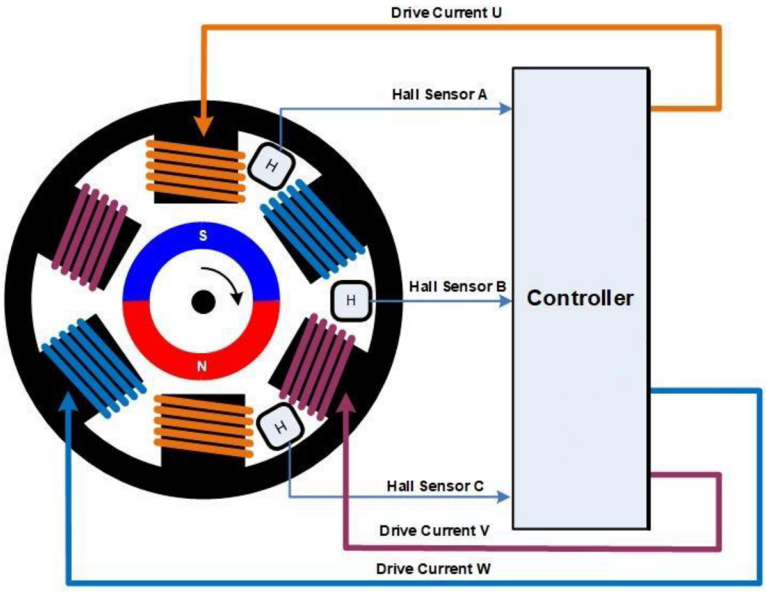

Figure 7.4 Scheme of BLDC motor [16]

In order to compare the motors, the simplified motor model is taken into account. Motor may operate at different voltages, but it is wise to use the values given by the manufacturer. For the chosen motor, the ideal motor voltage U_m=*100 V* and motor current I_m can be determined using the following equations stated in [6].

From the created database of suitable motors, BLDC motor T-MOTOR U15L KV43 for UAM applications was chosen. Motor characteristics stated by the manufacturer are attached in the appendix.

To be able to calculate motor performance, a simplified model of a motor based on [12] was used. Motor characteristic was calculated using following group of equations.

$$P_{iron} = U_m I_0 \tag{7.10}$$

$$I_m = \frac{U_m - \sqrt{U_m{}^2 - 4R_m\left(P_{iron} + P_{prop}\right)}}{2R_m} \tag{7.11}$$

$$P_e = U_m \cdot I_{\mathrm{m}} \tag{7.12}$$

$$\eta_m = \frac{P_m}{P_e} \cdot 100 \tag{7.13}$$

Calculated motor characteristic was then compared with the manufacturer's measured data of the same motor. For more precise validation of the model, thrust and torque of the propeller

T-Motor 47x18, which was used by the manufacturer for the measurements, was calculated based on the process described in the previous subchapter.

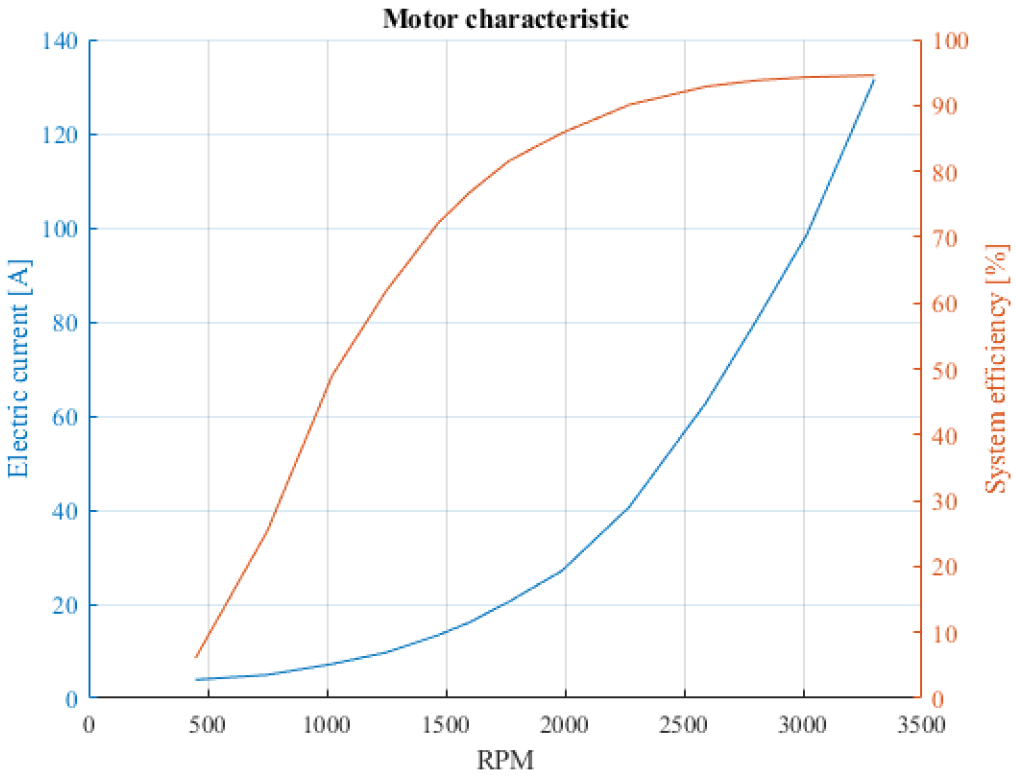

Figure 7.5 Calculated motor characteristic of T-motor U15L 43KV with the propeller Mejzlik 48x16.4

Following charts depicts comparison between the results obtained using motor model and manufacturer's data. In the comparison, proposed propeller model was used to simulate performance of T-Motor 47x18.

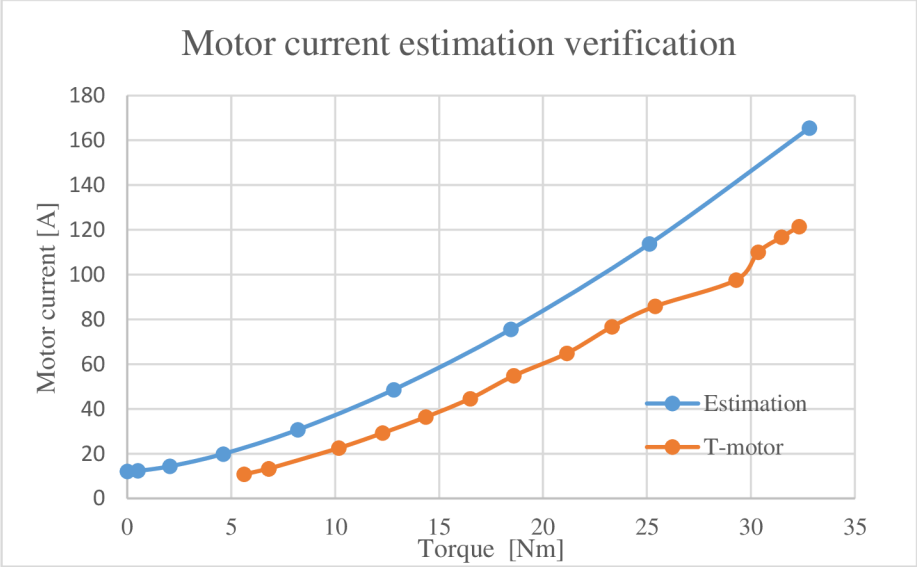

Figure 7.6 Electrical current computed via motor model compared with measurement

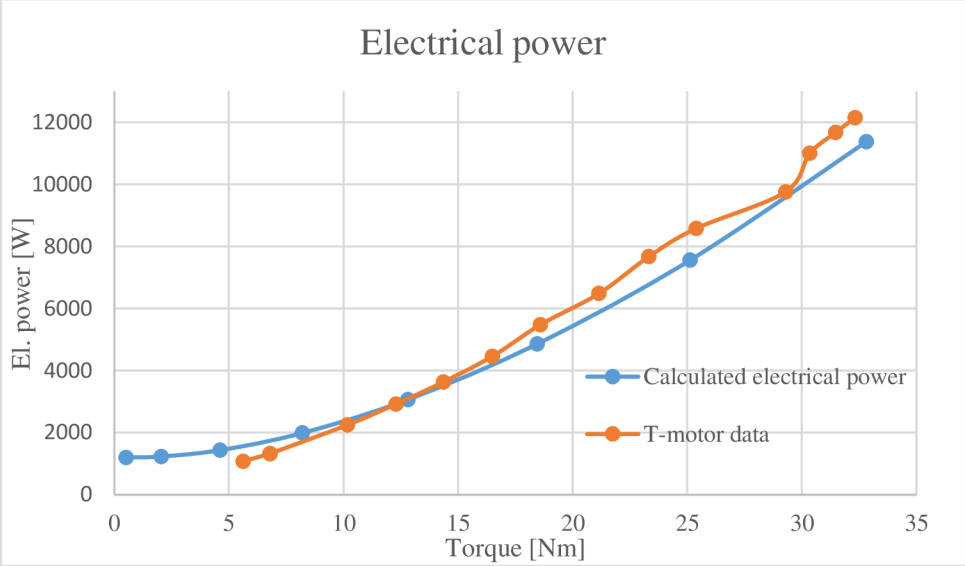

Figure 7.7 Electrical power computed via motor model compared with measurement

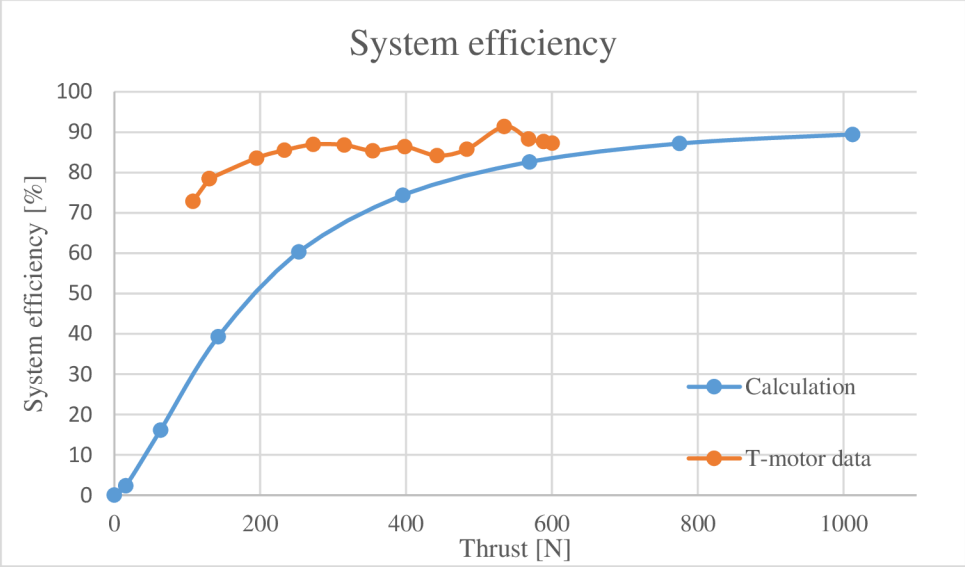

Figure 7.8 System efficiency computed via motor model compared with measurement

Results of the simplified model do not correspond unequivocally with the measurements, which could be also affected by the simplified propeller model, which neglects several propeller effects and do not respect the precise geometry of the given propeller. Another possible factor, which could affect the results was the neglecting of the losses in ESC and wirings. Additionally used values of motor resistance and no-load current may be misrepresented. However, the results are quite promising for the conceptual phase of the design, because they describe motor characteristic trends. This motor model will be used for the calculation of flight performance.

7.3 Selection of electronic speed controllers

In the case of brushless DC motors, mechanical gears are usually not used to control the speed, but so-called electronic speed controllers (ESC), which electronically commutate the speed of the electric motor. Each motor is usually connected to its own ESC, or all motors are connected to one central ESC. ESC consists of two circuits, one of which is connected to the battery by two wires and to the motor by three. In addition, the controller must be equipped with a low-current circuit which is used to process the control signal of the propulsion system. The input capacitors suppress high frequency noise that could affect the return electromotive voltage measurement. On the other hand, they cause delays that degrade the quality of control. Some controllers also include temperature sensors. In order to precisely control the rotation, hall sensors can be embedded in the stator of a motor, but more often measuring of back electromotive force is used for its simple principal, which is based on measuring voltage drops at non-active coils. Signals controlling the motor use pulse width modulation (PWM), which effectively divides the voltage signal into segments, which are determined by its amplitude and duration of the pulse. Again, it was necessary to create a database of controllers, which were determined by their electrical properties, mainly maximal voltage, current and weight.[17][18]

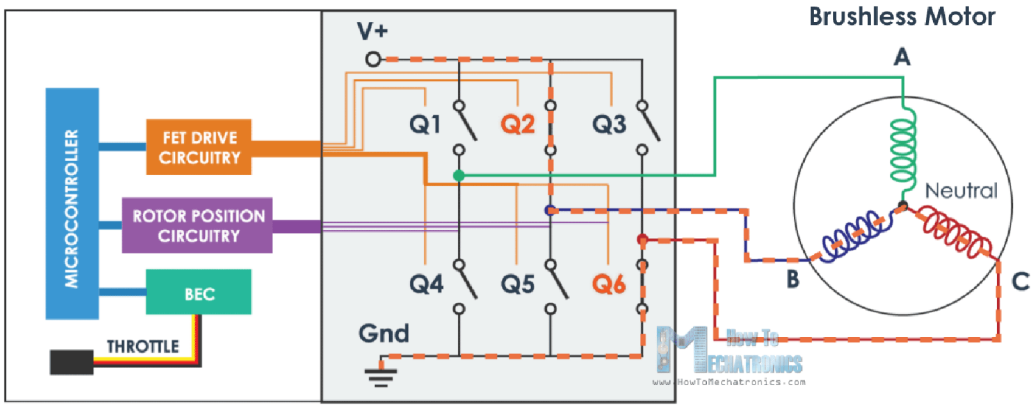

Figure 7.9 Simplified scheme of ESC circuit [18]

An ideal ESC is one that can commute a sufficient range of electric currents, so ESCs have been filtered based on the maximum electric current I_{eMAX} and its weight. As a most suitable ESC was chosen MAD AMPX 200A (12S-24S).

7.4 Selection of battery

Battery is a source of electric energy, which runs the propulsion system and also control subsystems. Beside the important role of a battery, its downside is in its weight, makes a battery one of the heaviest components of the whole aircraft, so it should be low as possible. Key parameter of the batteries, which evaluates the weight of a battery, is the specific power, which represents the power of the battery which can deliver from one kilogram of the battery weight. There are many types of batteries, but the most effective one for UAM applications are Li-ion batteries, since theirs specific power and energy density is the highest of commonly available batteries on the market. Li-ion batteries also have the best efficiency out of the list. The only main downside of this type of batteries is its high price.[15]

The most important characteristic of the battery is clearly its electrical capacity C_b, which is still evaluated based on the battery discharge. The battery cannot discharge below the minimum value of C_{min}, which expresses the safety minimum and is in the range of 15% ÷ 20% of the C_b value. A battery is composed of multiple cells. Important factor of a battery cell is the voltage, which battery cell can supply. The overall voltage of a battery is a result of a summation of the battery cells voltage.[6]

Batteries for electric aircraft propulsions systems are usually formed by creating as custom battery pack from battery cells. Resultant battery pack voltage and capacity unfold from the number of cells and also the arrangements. Cells connected in series increase the voltage and on the other hand cells connected in parallel increase battery capacity. Real number of the battery cells can be determined by multiplying number of battery cells in series and in parallel. Sadly, with the increasing number of cells battery pack weight increases exponentially, which has major influence on flight endurance.[19]

Battery endurance can be calculated by following simplified formula:

$$t_b = \frac{C_b}{I_b} \tag{7.14}$$

Since the current flowing from the battery into propulsion system increases with the aircraft weight, because required minimal thrust for hover rises simultaneously, finding the ideal battery capacity is a complex task, which needs optimization tools. Iterative calculation was performed to find the ideal battery capacity. Goal of the optimization was to define the minimal battery capacity to secure the desired flight endurance in hover with the maximal payload. At each battery configuration the battery current had to be calculated using motor model stated previously in this chapter. Nominal battery voltage was set to be 88.8 V, which equals to 24S. Peak voltage can be 100 V.

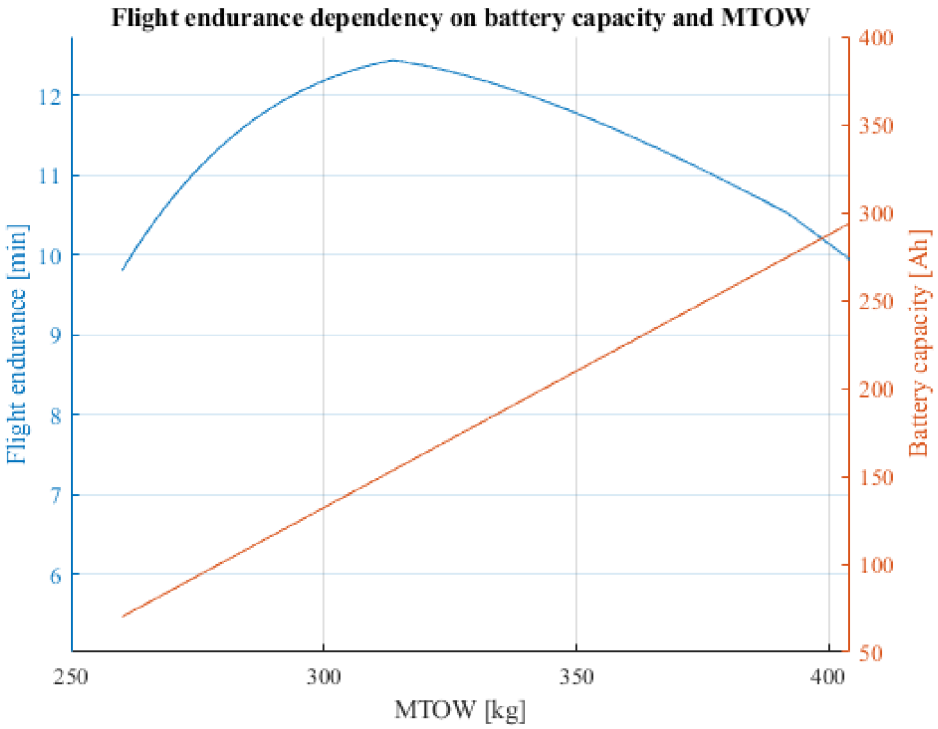

Figure 7.10 Dependency of flight endurance on MTOW and battery capacity

In the chart above it is possible to observe the dependency of flight endurance on battery capacity. Flight endurance rises with the battery capacity to the certain point but afterwards increasing capacity does not increase flight endurance, since the battery is too heavy, and the propulsion system is not able to produce enough thrust to carry such heavy battery.

Ideal battery pack for the application should contain 168 battery cells arranged in 24 series lines and 7 parallel lines, which could provide 182 Ah battery capacity. Expected weight of such battery pack could be 105 kg based on the known battery cells weight and estimated weight of the casing and wirings.

7.5 Possible ways of propeller performance improvement

7.5.1 Contra-rotating propellers configuration effect

From the results of preliminary design of a propulsion system it is obvious that for generating enough thrust it would be necessary to use propellers with the big diameters. Such big propellers are space consuming and also need bigger frame, which would make a multicopter even heavier. Because of that, coaxial configuration of motors was taken into account.

At this rotor configuration, propellers rotate contradictory, so the upper propeller generates thrust by pulling the air down and lower propeller is affected by the energy of the flow and creates smaller thrust, because the flow is affected by the upper propeller downwash. This phenomenon is displayed in the following picture. Coaxial configuration has a positive impact on power consumption for generating given thrust, which is lower in comparison to single rotating propeller rotating at higher rotational speed. However, most effective configuration for generating same thrust are two single rotating propellers. Acoustic profile of contra-rotating propellers is also perceptible, which is comparable to two single rotating propellers. [20][21]

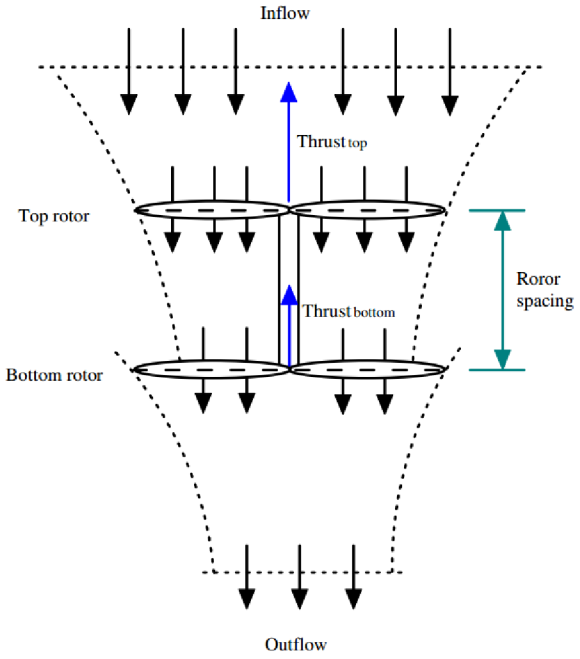

Figure 7.11 An experimental investigation on aerodynamic performance of a coaxial rotor [22]

Since the lower propeller is lightened by the upper propeller, lower propeller is allowed to rotate at higher rotational speeds, which is usually beneficial for motor efficiency, which increases with rotational speeds. On the other hand, lower propeller has problems with generating same thrust as the upper propeller. Finding the optimal settings requires testing, which observes overall power consumption with respect to different rotational speeds of upper and lower propellers and also tuning the distance between propellers, which is also dependent on the construction of multicopter.

7.5.2 Ducted fan effect

The losses due to the interference of the flow in coaxial configuration and the choice of smaller propeller diameters it was needed to implement the duct fan into the construction. Propellers placed in a duct produce higher thrust, in a publication [23] authors state that this thrust increase due to duct may reach 25÷30 %. The following figure schematically shows the effect of the duct.

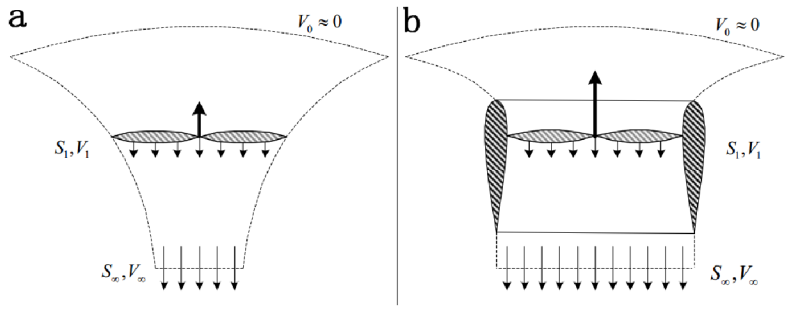

Figure 7.12 Illustration of ducted fan effect [23]

However, the geometry of the duct is crucial. The most influencing is the duct height and the cone angle of the duct. From the results of aerodynamic analysis in the work it is possible to derive the ducted fan influence on the lift and drag. At a vertical flight, the increase of vertical velocity means the rising of the thrust, but at some point, the thrust is decreasing with the additional vertical velocity. Considerable difference is in the forward flight, when the duct has similar behaviour as an airfoil, so the thrust depends not only on the duct geometry, but also the forward velocity and a certain angle of attack the lift and drag decrease. Choice of the duct airfoil is crucial. Since the chosen concept of load bearing ducts was chosen, an airfoil with bigger thickness was chosen. Influence of the ducted fan was evaluated together with the ground effect analysis performed in chapter 11.[23]

Propellers used in the ducts are usually adjusted to perform more efficiently. Blade tips are usually cutted and the clearance between the propeller tip and duct surface has an impact on the overall performance. Tip clearance should be the smallest in order to increase the efficiency. Chosen propellers would have to be customized and optimized in order to reach highest efficiency.[24]

Ducted fan has also other advantages, which improve the construction. Since it covers the rotating propellers, it also increases security of the pilot and surrounding environment. Inclusion of the duct to the construction also makes easier mounting of the motor and the propeller. It can also be a load bearing element.

8 CONCEPTUAL DESIGN OF MULTICOPTER FRAME

8.1 Initial design of the multicopter

Design of any new aircraft is a complex task and during the designing process several complications arise. Main concern of the conceptual design was to design light weight structure, which could carry a pilot and a battery with high capacity. Several iterations were created in order to optimize the construction to the feasible shape. Statistical research helped to set first boundaries, but during the process, several properties had to be changed in order to create the best multicopter.

Construction design counted with eight contra-rotating ducted propellers, which was based on statistical research and definition of propulsion system. Rotors were placed to the middle vertical position, approximately around the pilot's seat. This concept has several benefits, which are mainly based on a trade-off between usable ground effect and improved stability due to the lower CoG position. In comparison to the concept with rotors placed in the bottom, selected configuration allows easier landing on skis while preventing a damage of propulsion system. On the other hand, multicopters with the rotors placed above the pilot are much safer and its stability is also improved, but it deviates from the initial idea of a flying motorcycle. These concepts were not further developed for the reasons described above.

The following picture shows the final sketch of the designed eVTOL UAM vehicle.

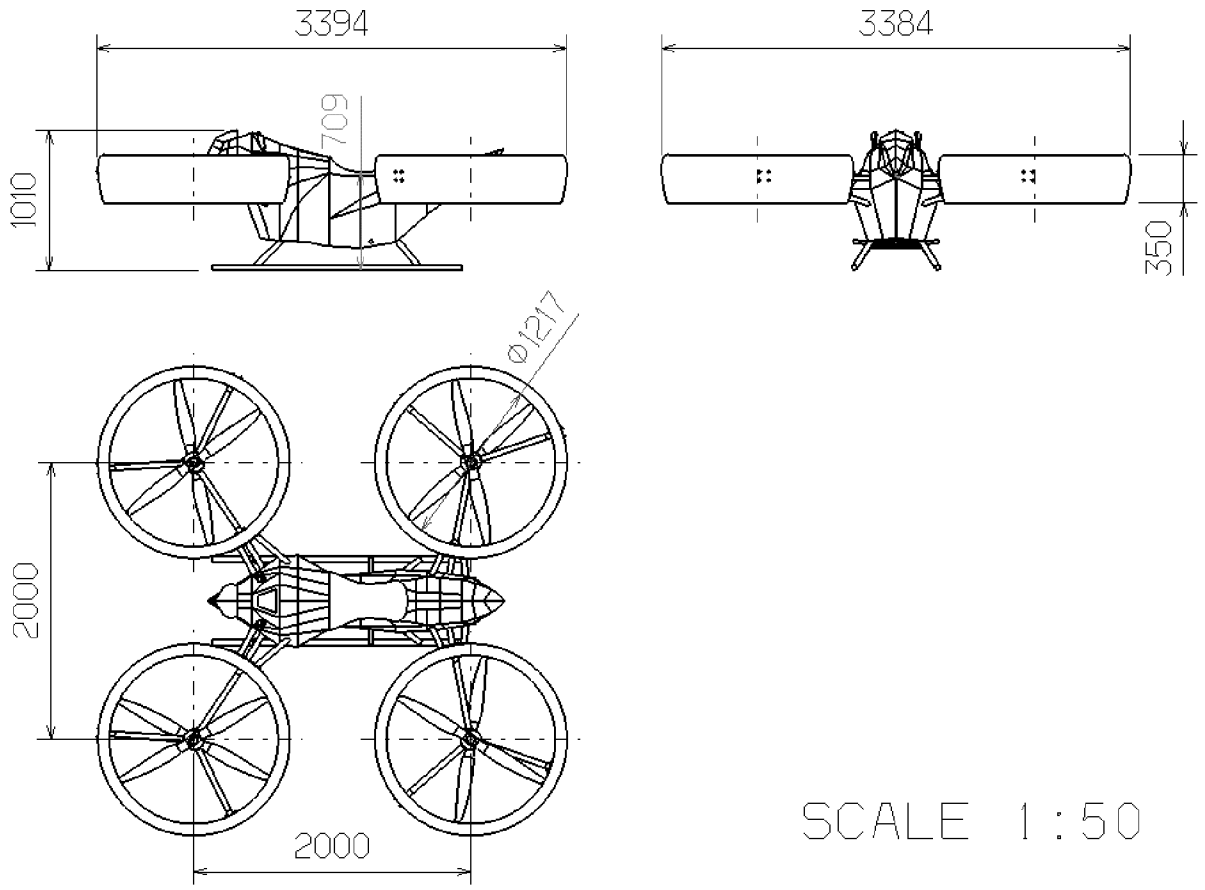

Figure 8.1 Drawing of final design

8.2 Ergonomics of the multicopter

Initial idea of a flying motorcycle had a great influence on the design, which should be ergonomic enough to make the flight for pilot as much comfortable as possible. Finding the most suitable seating position was also a crucial aspect of the design, so various sizes of mannequins had to be taken into account. Mannequin model available CATIA V5 Human Builder were used and placed into CAD model to find the ideal size of multicopter, so it would fit the majority of population. Pilots of the height 160, 185 and 200 cm were taken into account.

Figure 8.2 Ergonomics of the multicopter with the pilot 185 cm tall

X configuration of the multicopter makes the seat approaching easier since there was a space between propellers kept. Personal aerial vehicle (PAV) should not be too tall, otherwise the pilot had to climb into the seat with difficulties. Small vehicle would not be comfortable, since the pilot would have to crouch. Pilot can also rest hands on the covering and feet on the footrest.

8.3 Description of the multicopter design

During the designing, CAD software CATIA V5 was used due to its advanced possibilities of surface creation. Following picture shows the isometric view on the designed rotorcraft. Frame of the multicopter was tuned in order to find the optimal ergonomic seating position of the pilot. Construction can be divided into the central aluminium frame, which is covered by CFRP covering and the propeller ducts.

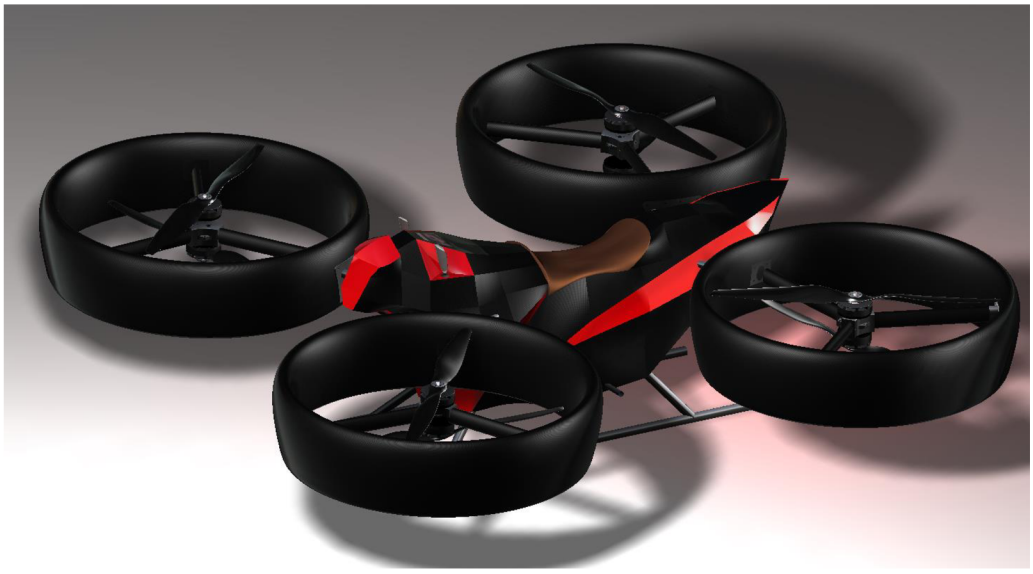

Figure 8.3 Isometric view on the designed multicopter

Figure 8.4 Front view on the designed multicopter

From the picture is evident the mounting design of the motors, which are placed on the connecting parts, which are connected to the ducts by 3 traverse beams.

Figure 8.5 Top view on the designed multicopter

Covering of the central space frame covers the battery, flight computed and wirings. ESCs are considered to be also placed inside the covering.

8.4 Multicopter central frame

Backbone of the designed rotorcraft is a welded rod frame consisting of 7039 aluminium tubular profiles. Using FEM analysis described in the chapter 10, the shape of the space frame was optimized in order to safely withstand applied load. Final shape of the frame is displayed in the following picture.

Figure 8.6 Multicopter space frame with duct connecting plates

8.5 Propeller ducts

Propeller ducts are the key elements of the designed multicopter since they form a bearing element for the propulsion system. Due to the chosen concept of flying motorcycle and the chosen composition of rotors and a pilot's seat, the ducts had to be designed as load bearing elements and not only aerodynamic and safety features. Relatively complex shape of the duct and lower specific weight were the main reasons for choosing composite material, to be more specific carbon fibre reinforced polymer (CFRP).

Beneficial aerodynamic effect of the duct is hart to estimate without an experiment or complex CFD analysis so the determining factor for choosing the airfoil was a construction thickness, which would enable inner reinforcing of the duct. Symmetrical airfoil NACA 0024 was chosen. Airfoil shape could be optimized in the future work in order to increase the aerodynamic benefit of ducted propellers.

Propeller ducts can be also considered as a safety feature since they cover the propellers, which would be exposed to the environment otherwise. A proposed safety feature which would prevent a pilot to come into a contact with rotating propellers is a spherical netting in the nearest quarters of the propeller ducts. However, structural strength of the netting and aerodynamic blockage effect would have to be checked.

8.5.1 Detailed description of duct construction

Propeller duct is connected to the central frame via a 7039 aluminium connecting plate with the thickness of 5 mm, which is welded to tubular profiles of the central frame. Connecting plate is bolted through the duct and some of the bolts connect also one of the traverse beams, which hold the central mounting flange of the motors and propellers. Traverse beams are composite elliptical beams glued by its ends to the inner connecting plate and central mounting flange. In order to prevent galvanic corrosion, an insulator or separation layer should be implemented between steel bolts and aluminium parts.

Figure 8.7 Detail of the propeller duct

Motor cables are considered to be routed through the beams, which are connecting duct to the central frame and then through the duct itself and traverse beam. In the motor mounting part are holes leading directly to motor. Unfortunately, these holes are stress concentrators and its leading path harms the structural integrity of the construction. On the other hand, routing cables directly on the outer surface would be less aesthetic and could increase drag and cause vibrations.

8.5.2 Composite lay up of duct and inner reinforcement

Due to the used mechanical joints it was important to focus on the reinforcement of duct shell surface since the mechanical joints disrupt the fibres and often can lead to failures such as bearing of shear-out. Lay-up of orthotropic composite should be in these cases chosen in the way to form a quasi-isotropic pattern. Plies of principal material directions should be chosen in a certain recommended ratio, which is displayed in the following chart. All used bolted composite parts fall to the recommended area.[25]

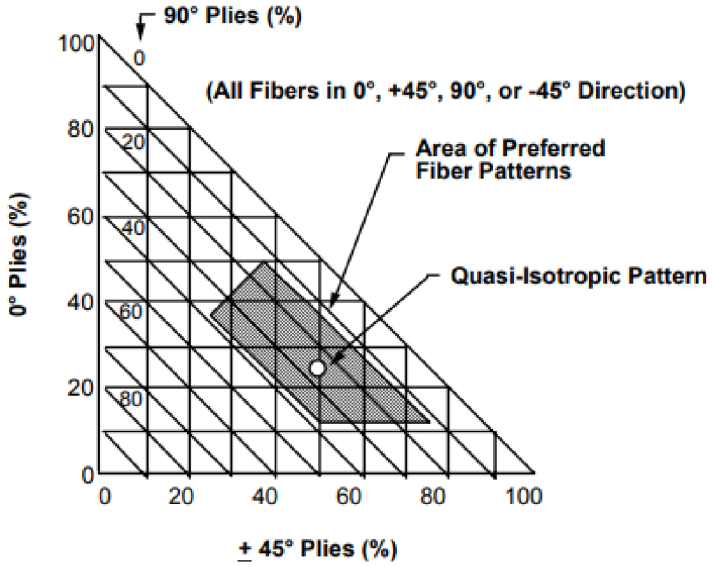

Figure 8.8 Recommended ratio of composite plies [25]

Following picture depicts a cross section of the duct and shows used lay-up of the composite structure. Reinforcement is structured to the omega profiles, which are glued together. Inside omega profile, Herex foam is placed to support the flanges of the beams and its main duty is to prevent a buckling of thin walled walls. Herex foam could be placed also to other parts of the shell in order to improve stability. Following picture depicts the final inner structure, which was tuned during the structural analysis. Lay-ups of other parts of the composite duct and other components can be found in the appendix.

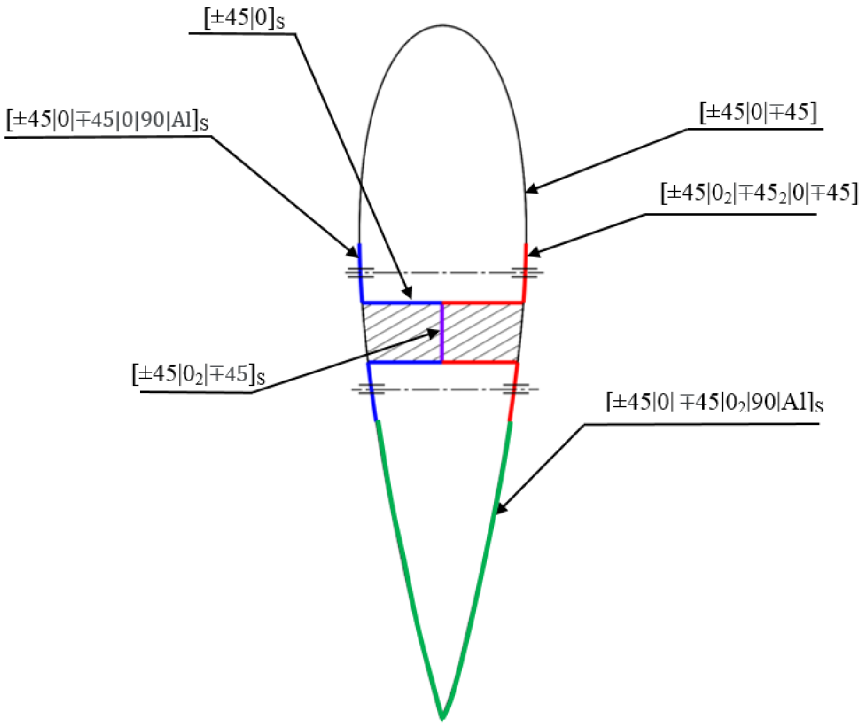

Figure 8.9 Lay-up of composite duct

8.5.3 Techniques of strengthening mechanical joints of composite materials

Mechanical joints are significant stress concentrators of CFRP parts, which is a big problem due to the low bearing strength of CFRP. Luckily, several improvements may be added into the structure in order to increase strength of the composite. Drilled holes also damage surrounding fibres and this degree of damage depends on the technology of drilling. Results of research show that the main focus should be on the quality of drill. Weared drill may tear out fibres instead of carving.[26]

8.5.3.1 Metal inserts

Metal inserts are often used parts, which help to increase strength of mechanical joints. Steel inserts were considered mainly around the connections to the central frame. This holes are the most critical part of the construction, as the results in the chapter 10 showed. Inserts may decrease bearing, tensile and shear stresses up to 75 %. Shape of the mechanical insert may be topologically optimized in regard to the stress distribution in order to reduce stress even more.[26]

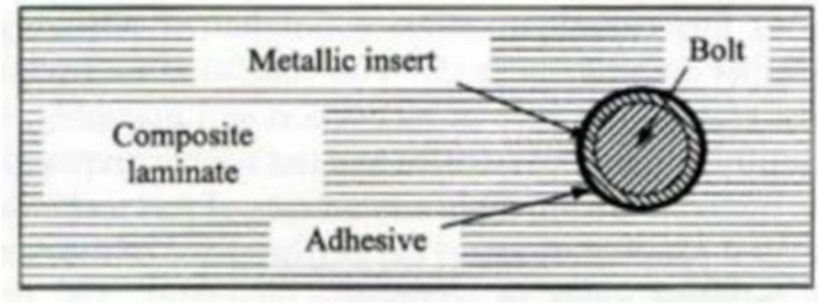

Figure 8.10 Scheme of the metallic insert in composite laminate [27]

8.5.3.2 Titanium foils

Creating a hybrid titanium-CFRP laminates may exhibit significant improvement of bearing strength of the composite. Research showed high-percentage up to 158 % at some cases. In order to design a safe construction, this feature was included despite the potential difficulties of manufacturing, which is done by gluing with strong glues. This glued contact may also suffer delamination, which is a main disadvantage.[28]

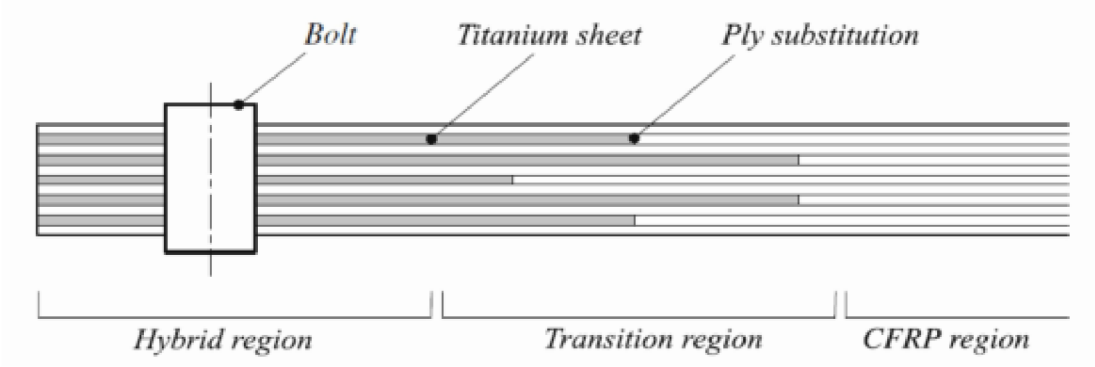

Figure 8.11 Illustration of hybrid composite suitable for mechanical joints [28]

Titanium foils are an expensive solution, which can suit heavy duty structures. However, for this application it would be redundant since the critical places of the duct are mainly around the connection to space frame. Nevertheless, main idea of gluing a metal plate was kept. Plate of aluminium 7075 with 3 mm thickness was taken into account as an interlaminar reinforcement. This plate was added to the laminate properties of duct's elements. It is important to mention that the strength and manufacturing errors were neglected.

9 CENTER OF GRAVITY OF MULTICOPTER AND STABILITY

9.1 Mass estimation

Hand in hand with the sizing of the propulsion system and multicopter frame, it is important to bear in mind the overall mass of the rotorcraft. Based on the statistical research, the mass of the rotorcraft was estimated for the initial estimations and calculations. However, the real weight of the rotorcraft is probably going to be different compared to the initial guess. Even though the rotorcraft is not designed to details yet, mass estimation is an important step for the conceptual design verification.

Since the design considers composite construction, a mass estimation is difficult to perform. However, the mass of the aluminium frame and composite duct was computed using prepared FEM model in MSC Patran.

Appended table summarizes the mass estimations of the multicopter construction parts and known weight of propulsion system components together with individual CoGs of these parts.

9.2 Centre of gravity calculation

Finding the centre of gravity of the multicopter is an important task, since its position derives the stability of the multicopter and also influences its maneuverability. In order to find the position of CoG, it is important to know all major heavy components and their positions. Since the multicopter is symmetrical along one axis, only the X and Z coordinates are needed. Following picture depicts the overall CoG and also centres of gravity of particular components.

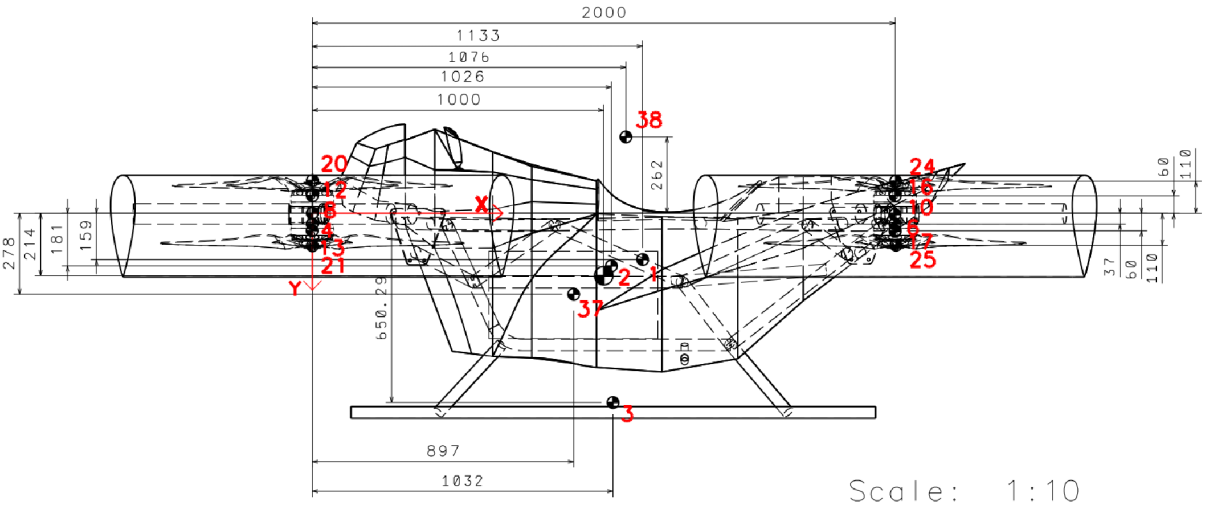

Figure 9.1 Centre of gravity of the designed rotorcraft

Ideal position of CoG along the horizontal axis is exactly in the middle between front and rear rotors. Otherwise, some rotors would have to rotate with different rotational speed in order to keep rotorcraft stable during hovering. Following table represents positions of CoG at different payload configurations.

Table 9.1 Total weight and center of gravity position for different payload configurations

Payload configuration	Total weight [kg]	CoG x [mm]	CoG y [mm]
Pilot 100 kg	320	1001	203
Pilot 85 kg	296	1027	206
Pilot 60 kg	280	991	194

CoG position at x axis should be exactly 1000 mm, since the distance between rotors is 2000 mm. Computed positions of CoG are very close to this ideal position. Its values is mainly influenced by the pilot and his seating position. Table with calculated all estimated weights and centres of gravity individual components is placed in the appendix of this work.

9.3 Stability of the multicopter

Vertical position of CoG determines multicopter stability during forward flight or wind interference. During the forward flight, not only the parasitic drag of the frame is generated, but also the propellers generate induced drag. When the CoG is lower than propellers and the aerodynamic centre, a stabilizing moment is generated. On the other hand, when the CoG lies above the propellers and the aerodynamic centre, a destabilizing moment occurs. Same principle applies during wind interference. Designed multicopter has the CoG located below the propellers and aerodynamic centre, so it can be said that the multicopter should be stable.[6]

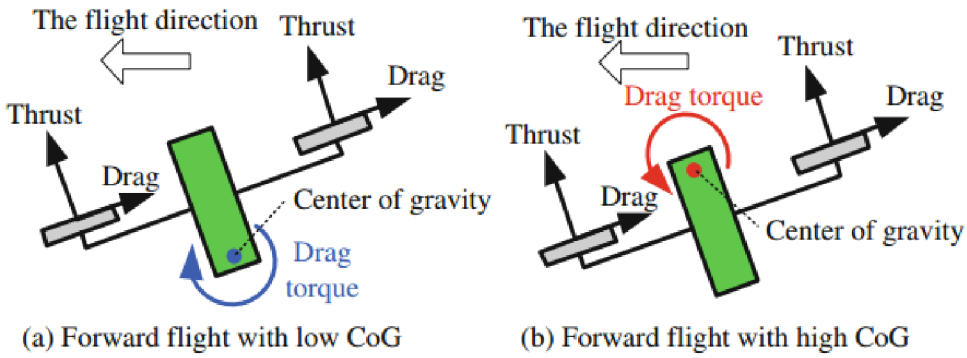

Figure 9.2 Impact on stability of vertical position of CoG [6]

Stability analysis of the multicopter is a complex parametric case, which requires a dynamic simulation. It is also highly dependent on the flight controller, which may can perform stabilization. However, based on the calculation of CoG it is possible to consider multicopter as stable, since its CoG is below bottom propellers. It is expected that drag generates stabilizing drag torque.

10 STRUCTURAL ANALYSIS OF THE MULTICOPTER FRAME

Designed frame is the crucial part of the rotorcraft construction, because it secures overall structural integrity. In this case, the frame is a hybrid construction combining aluminium beams, which work like a main load bearing element, and propeller ducts, manufactured from carbon fibre reinforced polymer, which transmit the loads to the aluminium rod frame. Geometrical complexity of designed frame lead to the use of finite element method (FEM). MSC Patran was used for FEM model and mesh preparation and the structural analysis was performed via MSC Nastran.

Structural analysis was divided to two main parts. The first solves the structural strength of central space frame with isolated composite ducts. The second part deals with composite duct strength, which was solved with isolated space frame. This approach was chosen in order to help easier optimization of separate parts and simplify a model for better computation performance.

Structural analysis was performed for static conditions, which occur practically only in stable hover. Otherwise, dynamic behaviour of the construction would have to be taken into account, which is difficult to estimate in the initial phases of conceptual design.

10.1 Loading case under static conditions

Main load acting on the multicopter during hovering is gravity of the pilot, the battery, propulsion system and weight of the frame itself. Thrust generated by the propellers acts against this overall gravity force and creates force equilibrium. Hover was chosen as a reference flight phase for the initial analysis. Another not negligible load is propeller torque. Following picture schematically shows the loads acting on the multicopter during hover.

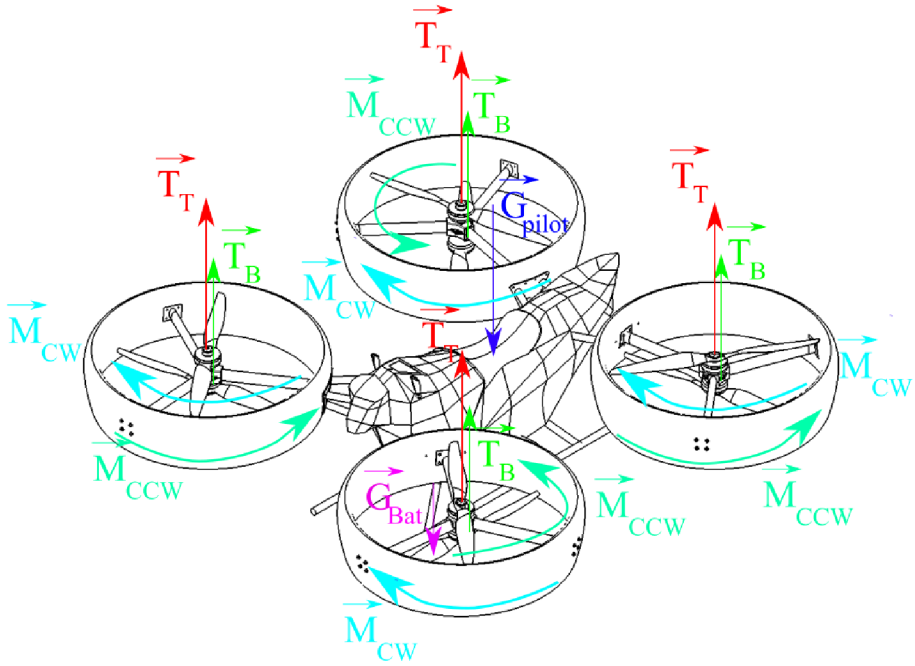

Figure 10.1 Static loads acting on the multicopter during hover

10.2 Structural analysis of space frame at hover n=3.5

Main goal of this part of structural analysis was to evaluate the structural integrity of the designed frame and determine suitable cross section of tubular profiles. Fairing of the central multicopter part was neglected since its main function is the covering and aesthetic appearance. Light components such as ESCs, were also neglected.

10.2.1 Finite element mesh

Welded frames do not only carry tensile and compressive axial loads but also bending, so BAR2 elements were chosen for the mesh of the beams. Rotor connecting plates are also involved in the model and to their holes MPC RBE2 elements are connected. Nodes of the circumferences of the holes are dependent and the node in the rotor centre is independent. RBE2 elements are rigid, which makes the model fully constrained. Since the frame is connected to the hypothetical centres of rotors, the rigidity of the duct is neglected. This simplified approach was used in the initial phase of the design and for to define the cross section of aluminium profiles. 3D shape of the beams and circles representing rotors are used only for illustration in the following picture.[29]

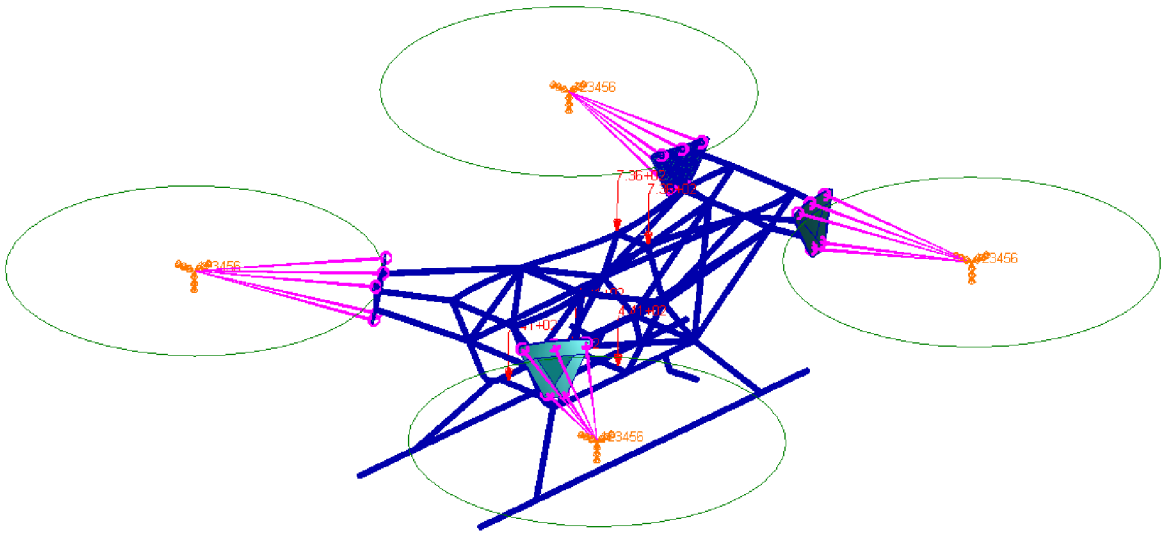

Figure 10.2 FEM model of the multicopter frame

Figure 10.3 Detail on finite element mesh used for duct connecting plateshows a detail of the mesh. For the duct connecting plates, triangular shell elements (TRI3) were used. Beams are connected to the plate at multiple nodes, which are shared also for the bar elements (BAR2).

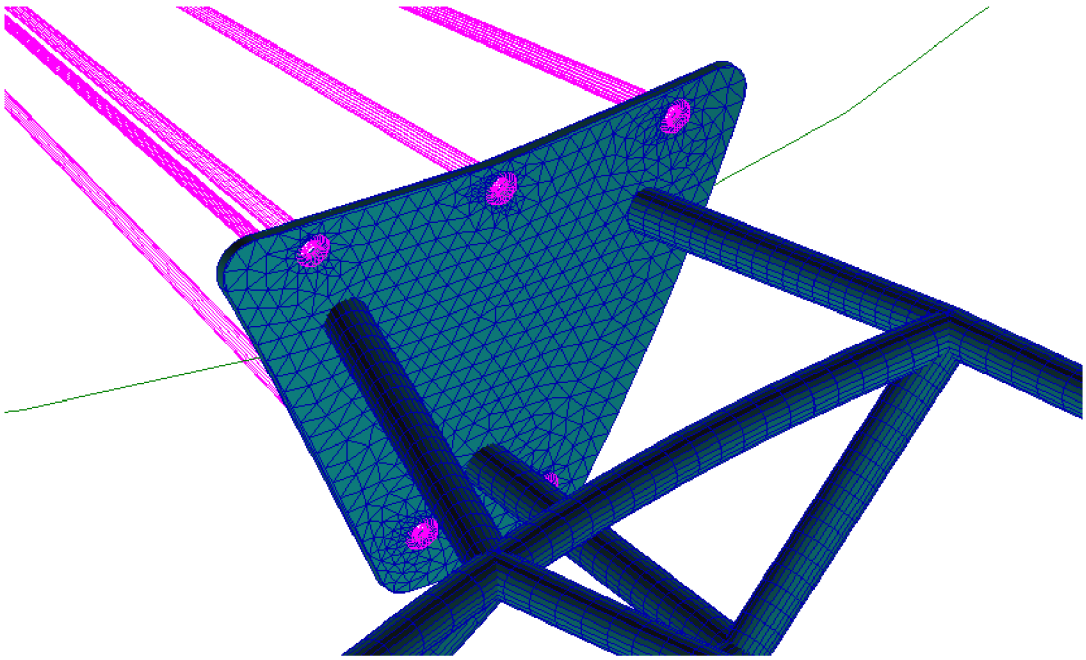

Figure 10.3 Detail on finite element mesh used for duct connecting plate

Table 10.1 Elements used for a mesh of multicopter frame

Component	Element type	Number of elements
Welded beams	BAR2	1574
Duct connecting plates	TRI3	6072

10.2.2 Boundary conditions and loads

For this part of the analysis, frame is constrained in the centres of rotors, where the zero displacement is set. Gravity of the pilot is represented by two forces acting directly at beams at the position of the seat. In reality, pilot's weight would be distributed with respect to his seating position. Battery load is divided to 4 contact points. Ultimate load was calculated for positive load factor 3.5 and with the factor of safety 1.5. Following table summarizes used boundary conditions and loads.

Table 10.2 Overview of used boundary conditions and loads

Displacement x,y,z	$<0\ 0\ 0>$
Gravity of the pilot (100 kg)	5150.25 N
Gravity of the battery (105 kg)	5407.76 N

10.2.3 Material characteristics

Chosen aluminium alloy is was chosen mainly for its weldability. Its material characteristics used for computation can be found in the following table.

Table 10.3 Mechanical properties of aluminium alloy 7039 - T64 [30]

Property	Aluminium 7039 – T64
E [GPa]	69.6
G [GPa]	26
μ [-]	0.33
σ_t $[MPa]$	450
σ_y $[MPa]$	380
τ [MPa]	260

10.2.4 FEM analysis results

Analysis was solved as linear static, since the hover phase can be considered as a static problem, where the resultant forces acting on the multicopter are in equilibrium.

10.2.4.1 Results of the FEM analysis of space frame structure

Welded space frames are loaded by combined loads. It is important to extinguish between the resultant stresses and evaluate multiple possible failures. Following picture shows the stress distribution of combined stress on the deformed body. Maximum stress combines bending and axial stresses. Deformation scale ratio is 1:1.

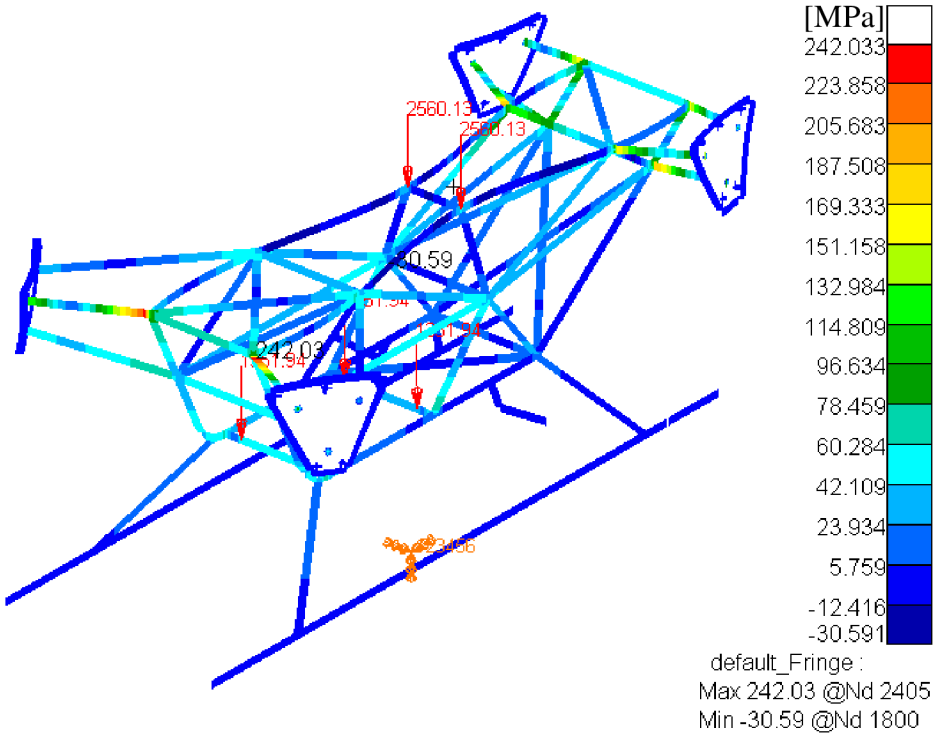

Figure 10.4 Maximum combined stress of the multicopter frame

Critical part of the space frame are the beams connecting the ducts to the frame. Main reason for this is that beams at this parts do not directly support each other and are relatively long. Frontal duct-connecting beams are loaded more compared to the rear beams.

Table 10.4 Resultant combined stress of the central frame

Maximal combined stress [MPa]	242
Minimal combined stress[MPa]	-237.5

$$RF = \frac{R_m}{\sigma_v} = \frac{450}{242} \geq 1 \tag{10.1}$$

$$RF = 1.86 \tag{10.2}$$

Results show that the designed space frame is safe enough to withstand ultimate load with the reserve factor 1.86, which can be considered as very safe structure and a reserve for the applied simplifications.

Maximal deformation at applied ultimate load is 10.2 mm, which occur at the ends of the beams connecting front rotors.

10.3 Structural analysis of composite propeller duct *n*=3.5

Beside the beneficial aerodynamic influence, propeller ducts have also a load-bearing function since the propulsion system generating thrust is placed in the middle of the duct. In order to design a light-weight structure, as a main material CFRP was chosen.

Structural analysis of orthotropic materials is more complex in comparison to isotropic materials used in the previous chapter because such materials have different strength in different directions. For orthotropic materials does not apply a rule of the coincidence between strain and stress principal axis.[30]

Structural analysis of such construction usually requires advanced FEM software, which allows analysis of composite orthotropic material, so MSC Nastran was used. It also provides a Laminate Modeller module for more efficient designing of composite lay-up and also evaluate the results using failure criterions.

10.3.1 Geometry preparation

Preparation of the meshes for composite structures slightly differs from the analysis of isotropic materials since the composite structures are consisted of different lay ups and materials. Surfaces of the 3D model of such component has to be divided into independent surfaces according to the changing ply lay-up. Different colours used for surfaces in the following picture represent partition of 3D model.

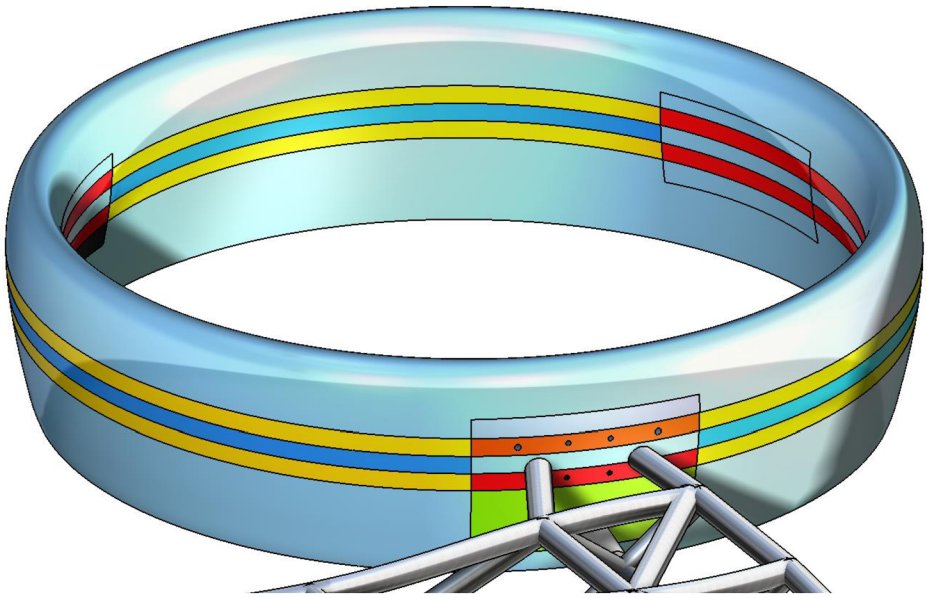

Figure 10.5 Geometry preparation of composite duct

10.3.2 Finite element mesh

Mesh of this composite part consists of various elements. CFRP duct surfaces were meshed with quadratic shell elements (QUAD4) with the size of 10 mm. Traverse beams connecting the propulsion system to the duct surface were also meshed with quadratic elements but the glued part was meshed with TRIA3 shell elements to fit the hexahedral mesh of the motor mount for which TET3 elements were used. Inner reinforcement was also meshed with these elements. Connecting plates were meshed with shell triangular elements (TRIA3). Bolt connections were presented as the beam elements connected to the MPC RBE2 elements.

Table 10.5 Element types used for a mesh of propeller duct

Component	Element type	Number of elements
Duct surfaces	QUAD4	41405
Inner connecting plates	QUAD4	1014
Main connecting plate	TRIA3	1638
Connecting beams	QUAD4/TRIA3	1360/1335
Motor mount	TET4	46794
Bolts	BAR2	36
Central frame beams	BAR2	300
Total number of elements		95520

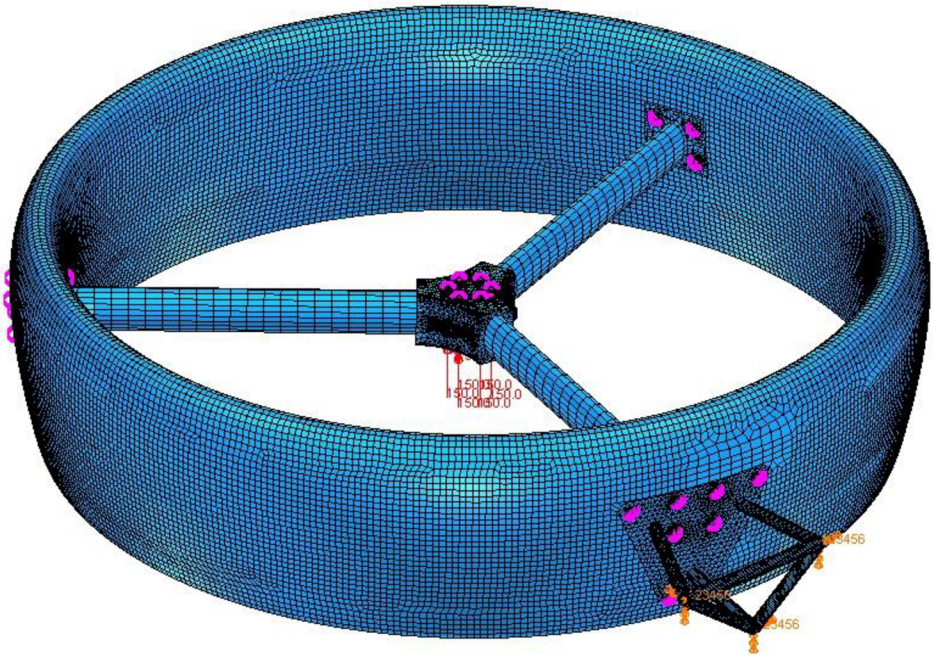

Figure 10.6 Mesh of the propeller duct

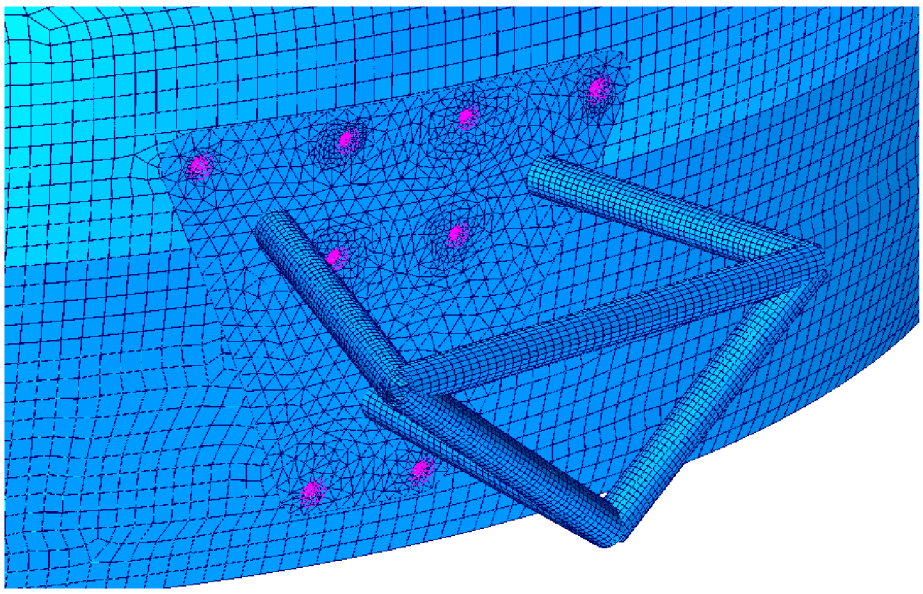

Figure 10.7 Detail of mesh of duct connecting plate and part of the frame

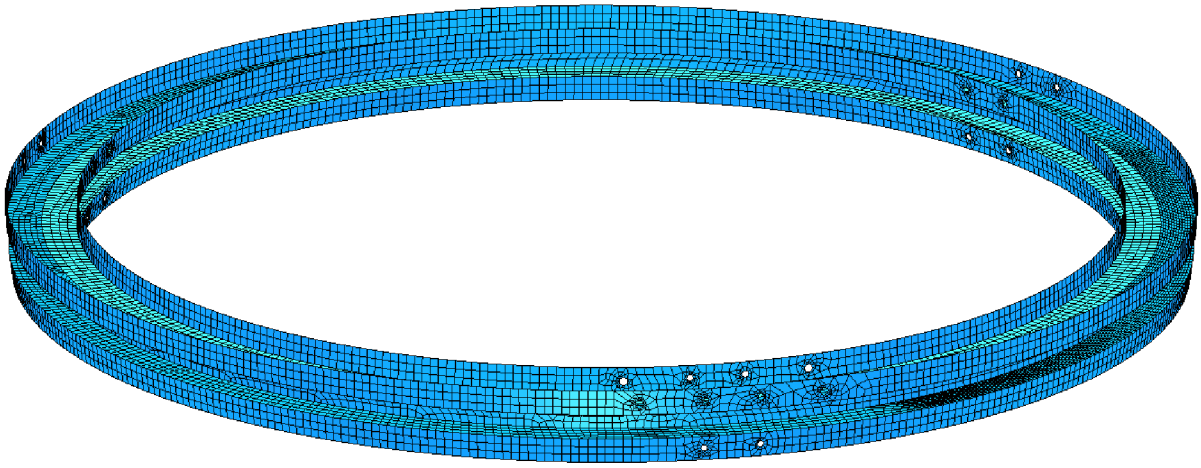

Figure 10.8 Finite element mesh of the inner reinforcements

10.3.3 Material characteristics

CFRP composites are materials manufactured from carbon fibres and are cured usually with epoxy resin matrix. Carbon fibres are very strong materials by itself mainly in its axial direction. This makes the CFRP composites orthotropic materials, which means that their mechanical characteristics depend on the loading direction. Following picture shows the material coordinate system of a laminate.[30]

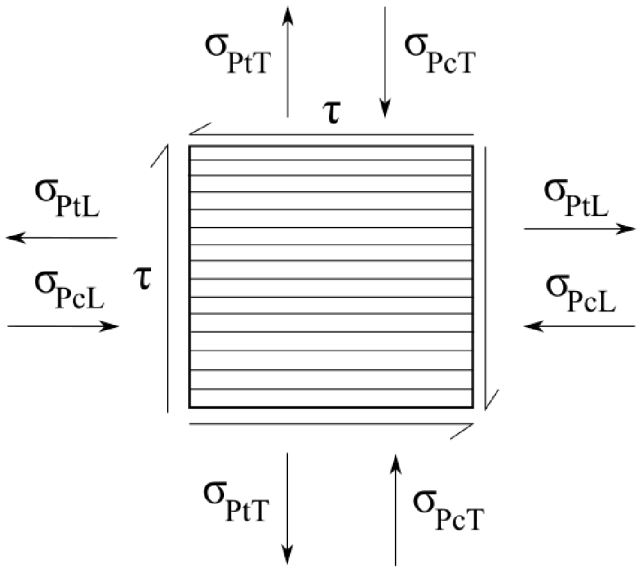

Figure 10.9 Principal and shear stress of unidirectional laminate

Resultant material properties of the composite material are determined besides the carbon fibre and epoxy strength also by the composite lay-up. Laying layers in different directions makes the composite able to withstand more complex loads. Number of layers usually increases overall strength of the composite but on the other hand also increases the weight of the part. Hence, ideal lay-up structure has to be found by optimization of the lay-up.[32]

In order to obtain accurate mechanical properties of the used material, a specimen of the designed structure would have to be manufactured and tested. If the specimen was manufactured in the same way as a resultant construction, it would also include the impact of manufacturing technology.[30]

Since the design is in the conceptual phase, there was not a need for manufacturing specimens and testing them. Chosen mechanical properties summarized in the following table correspond with the experience and common values of CFRP specimens tested in the testing lab of Institute of Aerospace engineering of Brno University of Technology.

Table 10.6 CFRP mechanical properties

Mechanical property	CFRP
E_1 $[MPa]$	77000
E_2 $[MPa]$	3400
μ_{12} [-]	0.28
G_{12} $[MPa]$	2581
σ_{PtL} $[MPa]$	848
σ_{PcL} $[MPa]$	546
σ_{PtT} $[MPa]$	100
σ_{PcT} $[MPa]$	100
τ [MPa]	50

Table 10.7 Mechanical properties of aluminium 7075-T6 [30]

Property	Aluminium 7075-T6
E [GPa]	71.7
G [GPa]	26.9
μ [-]	0.33
R_m $[MPa]$	572
R_e $[MPa]$	503
τ [MPa]	331

10.3.4 Boundary conditions and loads

Loads acting on the duct could be isolated from the central multicopter frame in order to make a simpler FEM model. Besides the gravity, another significant load acting on the duct is propeller thrust and reaction torque generated by the propellers. Loads were applied to the two nodes and transmitted to the nodes of the mounting pattern holes using MPC RBE2. Aerodynamic drag of the ducts during forward flight was neglected. Trust per propeller was calculated directly as a fraction of maximal thrust computed in chapter 10 and number of propellers and multiplied by safety factor and load factor, which is represented in the following calculation. Safety factor used to determine the ultimate load was chosen as 2.25 in order to cover material behaviour change due to increased temperature or humidity and manufacturing errors.

$$T_U = \frac{T_{MAX}}{8} \cdot SF \cdot n = \frac{3624.88}{8} \cdot 2.25 \cdot 3.5 \tag{10.3}$$

$$T_U = 3568.2\,N \tag{10.4}$$

Torque was applied at the same point as a reaction to the propeller torque and interpolated for the given thrust based on the measurements of the propeller manufacturer.

$$M_U = M \cdot SF \cdot n \tag{10.5}$$

$$M_U = 24.4 \cdot 2.25 \cdot 3.5 \tag{10.6}$$

$$M_U = 192.15\,Nm \tag{10.7}$$

Part of the central multicopter frame was included in the FEM model. Beams connecting duct to the central frame were constrained at theirs connecting nodes to have a zero displacement.

10.3.4.1 Gyroscopic moment estimation

Rotating propellers generate gyroscopic moments during maneuvering since the multicopter also tilts during pitching or rolling. Most significant magnitudes of gyroscopic moment should appear during pitching to forward flight because the tilt angles will be bigger in comparison to rolling. On the other hand, contra-rotating propellers generate gyroscopic moments of opposite orientation, but since they act on different part of construction, both gyroscopic moments had to be taken into account. Propeller moment of inertia along its rotation axis was provided by the manufacturer. Following picture describes the directions of gyroscopic moments generated during pitching.

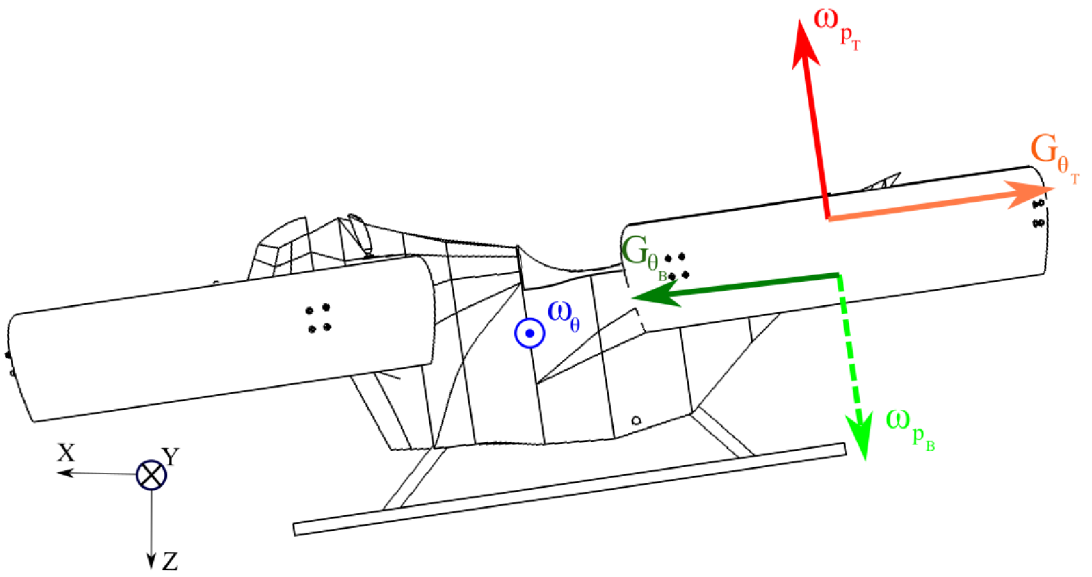

Figure 10.10 Rotational speeds and gyroscopic moments of rear right rotor

In order to accurately obtain angular precession rate, dynamic simulation would have to be performed. However, rough estimation was performed using following formula. Maximal pitch angle was taken as 30° from hover position and duration of maneuver as 0.5 s.

$$\omega_\theta = \frac{\theta}{t} = \frac{\frac{\pi}{6}}{0.5} \tag{10.8}$$

$$\omega_\theta = 1.05\, rad \cdot s^{-1} \tag{10.9}$$

Exact value of required thrust, hence rotational speed of top and bottom propeller could also be obtained from dynamic analysis for given maneuver. For a purpose of structural analysis, these values were guessed based on the maximum power of motors. As a reference propeller rotational speed was taken as 284.4 rad/s (2716 RPM), which is a considered maximum.

Gyroscopic moment can be then calculated using following equation.

$$\vec{G}_{\theta_t} = J_p \vec{\omega}_p \vec{\omega}_\theta \tag{10.10}$$

$$\vec{G}_{\theta_t} = 0.02337 \cdot 284.4 \cdot 1.05 \tag{10.11}$$

$$\vec{G}_{\theta_t} = 6.98\, Nm \tag{10.12}$$

$$\vec{G}_{\theta_{Ut}} = \vec{G}_{\theta_t} \cdot n \cdot SF \tag{10.13}$$

$$\vec{G}_{\theta_{Ut}} = 6.98 \cdot 3.5 \cdot 2.25 \tag{10.14}$$

$$\vec{G}_{\theta_{Ut}} = 54.95\,Nm \tag{10.15}$$

Considered bottom propeller rotational speed is 314.15 (3000 RPM). Bottom gyroscopic moment is then:

$$\vec{G}_{\theta_b} = 0.02337 \cdot 314.15 \cdot 1.05 \tag{10.16}$$

$$\vec{G}_{\theta_b} = 7.71\,Nm \tag{10.17}$$

$$G_{\theta_{Ub}} = G_{\theta_b} \cdot n \cdot SF \tag{10.18}$$

$$G_{\theta_{Ub}} = 7.71 \cdot 3.5 \cdot 2.25 \tag{10.19}$$

$$G_{\theta_{Ub}} = 60.72\,Nm \tag{10.20}$$

From the results it can be said that the resultant gyroscopic moment can be neglected, but it was included in the FEM analysis.

10.3.5 Results of FEM analysis of composite duct

Structural analysis of composite material is difficult task since the prediction of failure depends on many factors such as used materials, sequence of plies and environment. However, majority of failures initiate in the individual ply. Because of that, it is important to evaluate stress distribution in every ply and find the critical ones.[32]

Several types of failure may occur at composite structures [32]:

a) matrix cracking
b) first ply failure
c) ultimate failure when the laminate fails
d) traverse failure or delamination
e) fibre buckling
f) bearing failure or shear–out

Main focus will be on first ply failure, even though its appearance does not directly lead to the fatal failure of the composite structure, because rest of the undamaged layers may be able to withstand the load.[32]

10.3.5.1 Deformations

Deformations at the ultimate load reach maximum at the furthest point from the connecting beams, as can be seen in the following picture. Red wireframe represent the deformed state. Maximal deformation reaches 106.7 mm, which does not endanger structural strength of the duct, but it could affect the multicopter stability, by the impact of this fact is difficult to predict. Following picture shows a distribution of deformations of composite duct.

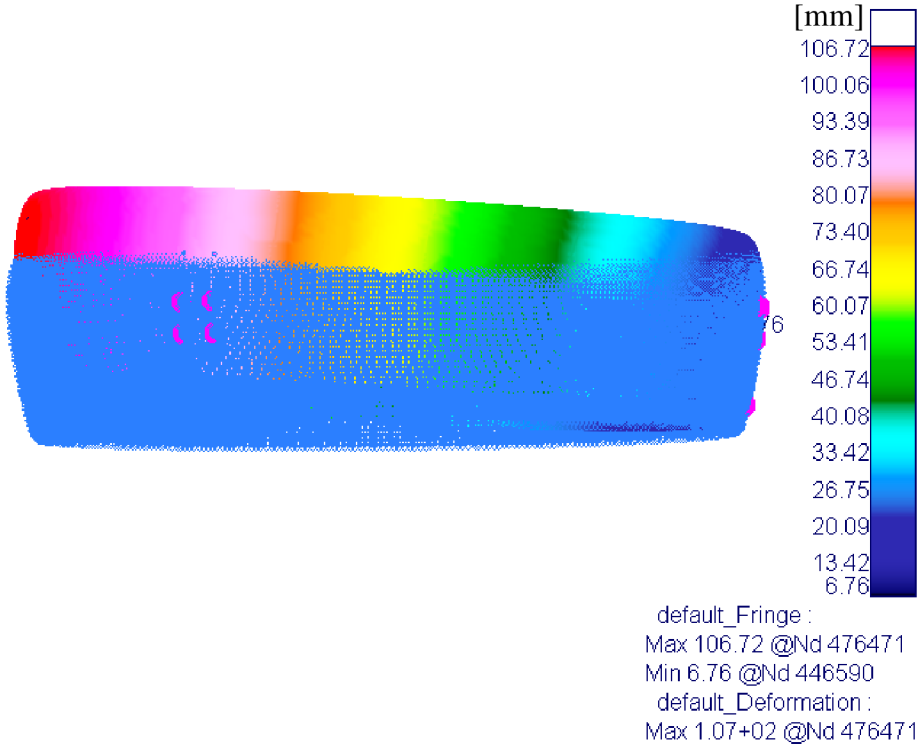

Figure 10.11 Deformations of the construction at ultimate load (true scale)

10.3.5.2 Stress distribution

Following pictures shows stress distribution of all layers of the composite duct. Major weak points of the constructions are around holes, where bolts connect the duct to central frame and create stress concentrations. Following pictures show stress distribution of the composite duct.

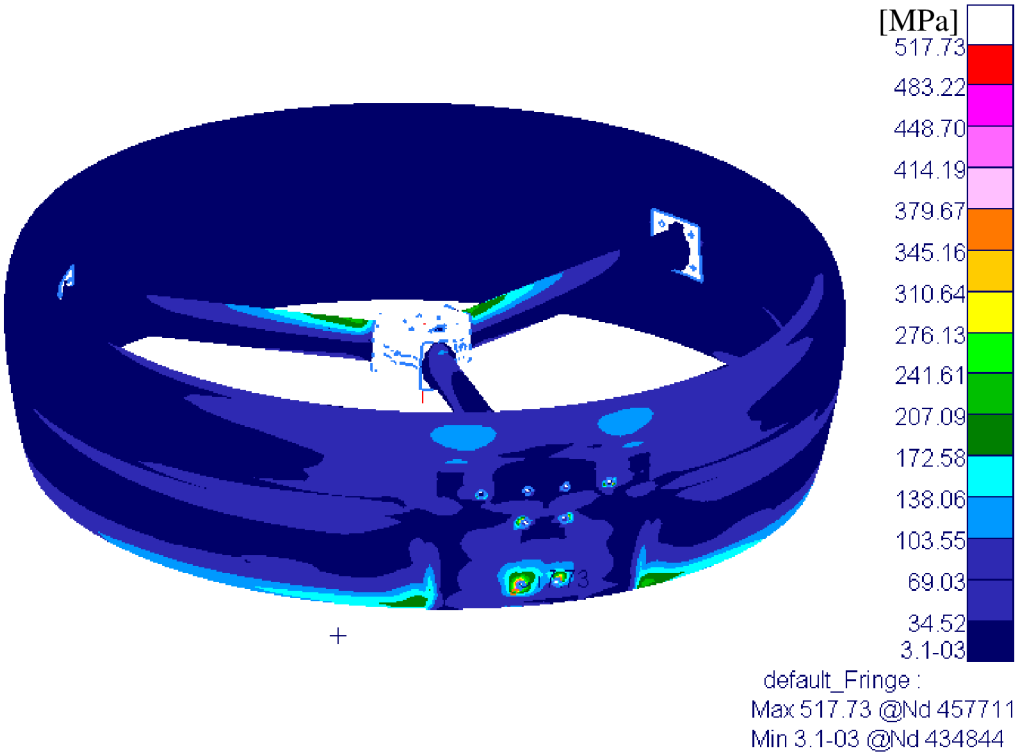

Figure 10.12 Tensile stress distribution on composite parts

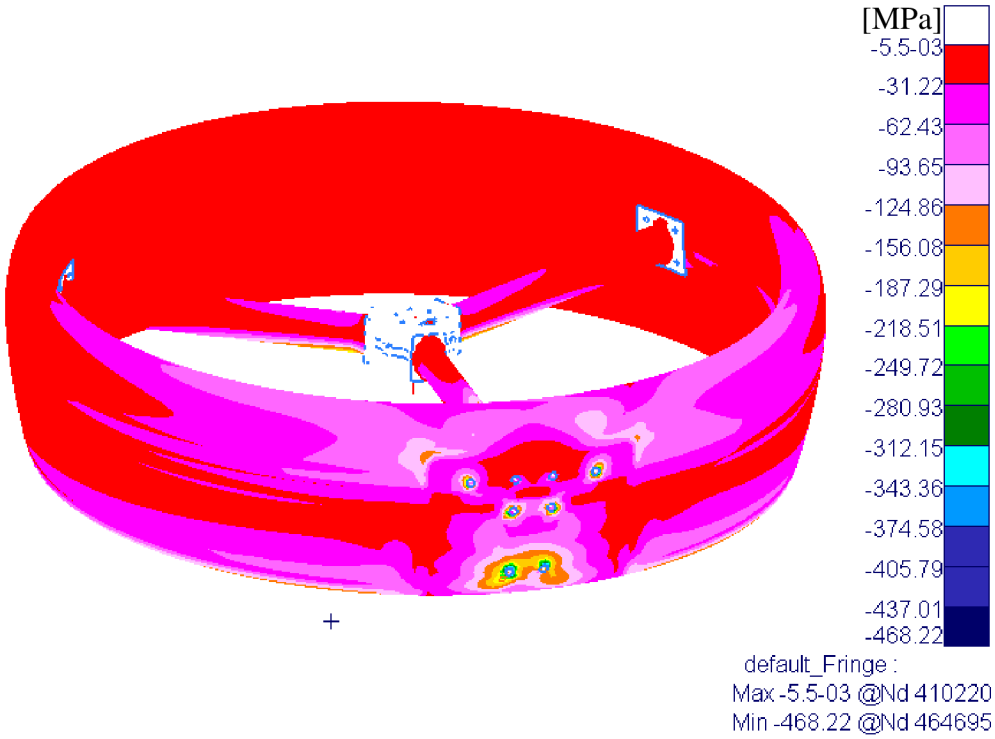

Figure 10.13 Compression stress distribution on composite parts

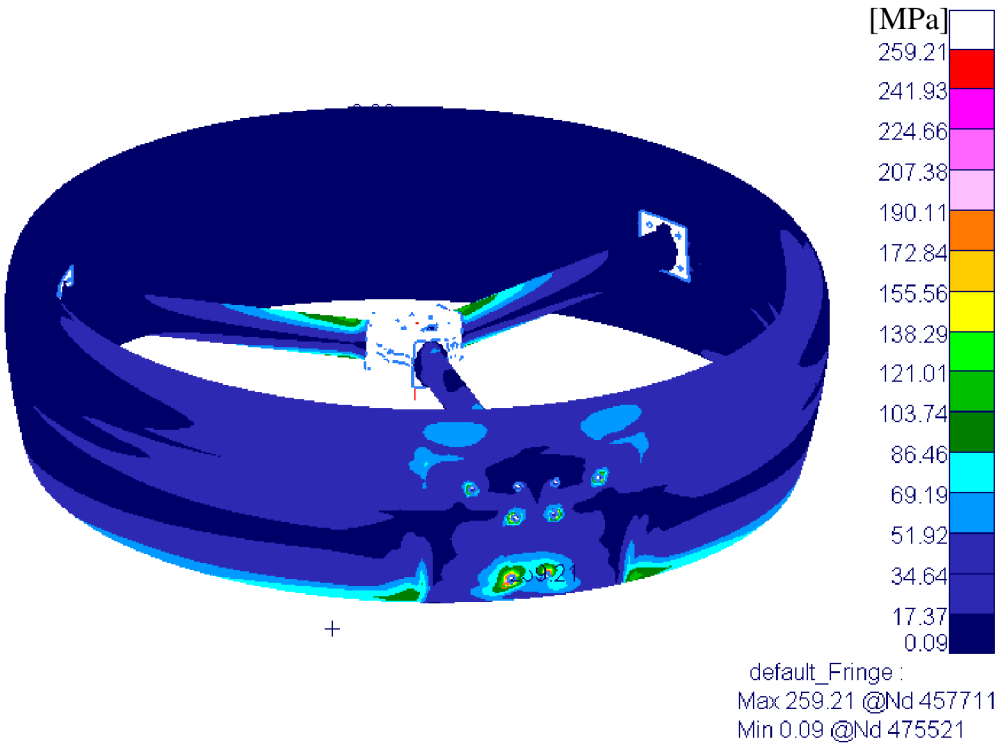

Figure 10.14 Shear stress distribution on composite parts

Another loaded parts are traverse beams connecting motor mount to the duct and the holes connecting this beams to the duct. However, these stresses are significantly lower in comparison to the main connecting holes. Stress concentration at the trailing edge of duct near the connecting plate occur mainly due to the stiffness change. Both places are not considered as dangerous for the overall structural integrity.

Main scope was focused on the hole in the inner side of the duct near to the frame, where the stress magnitudes reach highest values. Following picture shows the maximal tensile stress distribution of selected critical elements. For the most critical element, tabular overview of principal and shear stresses across the lay-up is appended in the table below.

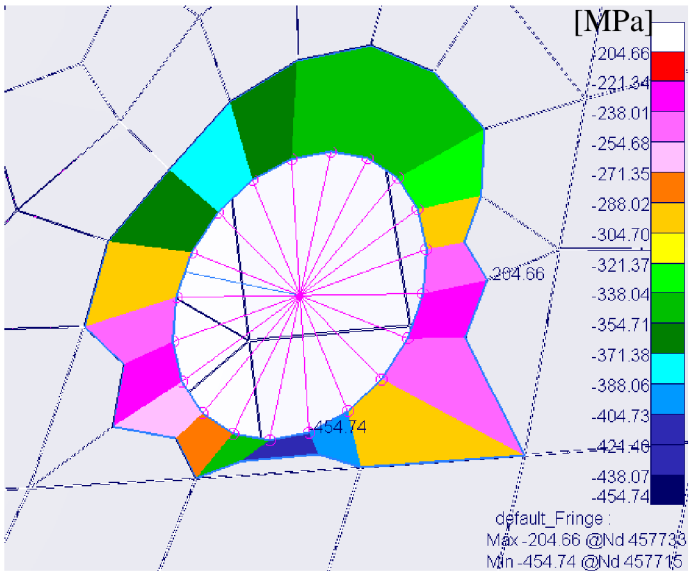

Figure 10.15 Detail on the most critical part of the composite duct (compressive stress)

Table 10.8 Stress distribution across layers of critical element of left bottom hole

Ply number	Material	Thickness [mm]	Orientation [°]	Max principal stress [MPa]	Min principal stress [MPa]	Max shear stress [MPa]
1	CFRP	0.32	+45	505.15	-0.29	252.72
2	CFRP	0.32	-45	328.97	-1.57	165.27
3	CFRP	0.32	0	442.82	-2.41	222.62
4	CFRP	0.32	-45	261.35	-5.52	133.43
5	CFRP	0.32	+45	380.91	-5.88	193.39
6	CFRP	0.32	-45	194.65	-10.72	102.68
7	CFRP	0.32	0	459.93	-11.66	235.79
8	CFRP	0.32	0	399.41	-13.57	206.49
9	CFRP	0.32	90	53.56	-40.23	46.90
10	Aluminium 7075	4.00	-	74.28	-85.08	79.68
11	CFRP	0.32	90	37.38	-55.01	46.20
12	CFRP	0.32	0	11.25	-382.12	196.69
13	CFRP	0.32	0	9.85	-442.88	226.36
14	CFRP	0.32	-45	8.17	-371.29	189.73
15	CFRP	0.32	+45	3.97	-199.35	101.66
16	CFRP	0.32	-45	3.64	-439.03	221.34
17	CFRP	0.32	0	1.05	-260.63	130.84
18	CFRP	0.32	-45	0.47	-507.18	253.82
19	CFRP	0.32	+45	0.00	-322.96	161.48

From the stress distribution it is obvious that major stress acting in the critical elements is compressive in the outer side of the composite duct.

10.3.5.3 First ply failure evaluation

Max stress criterion

This criterion is a stress-based criterion, which compares the maximal applied principal stresses at the material with its strength. It is important to check the stresses at every material direction. First failure then occurs, when the maximal stress ratio described by the following equation is overcomes 1.[32]

$$\max\left(\frac{\sigma_{1t}}{\sigma_{PtL}},\frac{\sigma_{1d}}{\sigma_{PcL}},\frac{\sigma_{2t}}{\sigma_{PtT}},\frac{\sigma_{2d}}{\sigma_{PcT}},\frac{\tau_{12}}{\tau_{PLT}}\right)<1 \tag{10.21}$$

Tsai-Wu criterion

Tsai-Wu criterion is a quadratic stress failure theory, which covers also an effect of multiaxial loads. It can be considered as more general criterion also for its possibility of distinguishing difference between tensile and compressive strength. Failure index can be calculated using following set of equations.[32]

$$FI = F_1\sigma_1 + F_2\sigma_2 + F_{11}\sigma_1^2 + F_{22}\sigma_2^2 + F_{66}\tau_{12}^2 + 2F_{12}\sigma_1\sigma_2 < 1 \tag{10.22}$$

$$F_1 = \frac{1}{\sigma_{PtL}} - \frac{1}{|\sigma_{PdL}|} \tag{10.23}$$

$$F_2 = \frac{1}{\sigma_{PtT}} - \frac{1}{|\sigma_{PdT}|} \tag{10.24}$$

$$F_{11} = \frac{1}{\sigma_{PtL}|\sigma_{PdL}|} \tag{10.25}$$

$$F_{22} = \frac{1}{\sigma_{PtT}|\sigma_{PdT}|} \tag{10.26}$$

$$F_{66} = \frac{1}{\tau_{PLT}^2} \tag{10.27}$$

$$F_{12} = \frac{-1}{2\sqrt{\sigma_{PtL}\cdot|\sigma_{PdL}|\cdot\sigma_{PtT}\cdot|\sigma_{PdT}|}} \tag{10.28}$$

Discussed stress-based criterions can be displayed in the stress space, which is defined by the boundaries of maximum stresses at two principal stresses axis. Stress states placed inside the closed curves, which is for maximum stress criterion a rectangle and for Tsai-Wu an elliptical curve, are in the safe range. Stress states outside of these shapes cause first ply failures.[32]

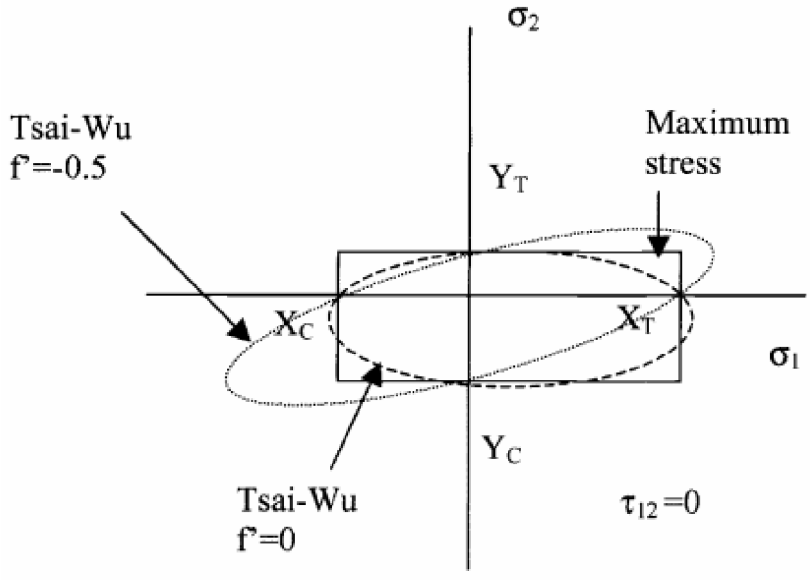

Figure 10.16 Comparison of failure envelopes of failure criterions [32]

With the usage of Laminate modeller module of Patran, it was possible to directly calculate failure index calculated by Tsai-Wu criterion. Following picture shows a distribution of the failure index, which should be lower than 1 in all layers.

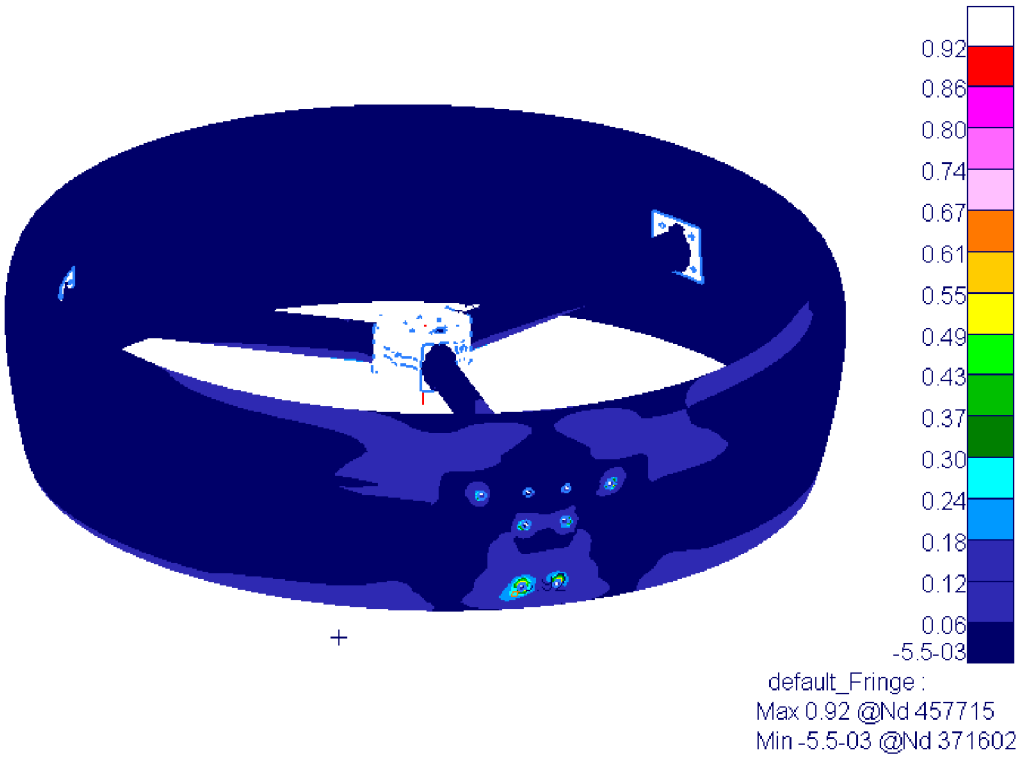

Figure 10.17 Average failure index of all composite layers

From the results it is evident that the failure index is lower than 1 even at the most critical parts around the holes connecting duct to the central frame. Other parts of the construction can be considered as very safe and could be even lightened by reducing number of plies.

Failure indexes of each layer were calculated only for the chosen critical element, due to its stress magnitude. Table 10.9 Failure indexes across the layers of critical element of composite duct shellshows failure indexes calculated by Tsai-Wu criterion for this element.

Table 10.9 Failure indexes across the layers of critical element of composite duct shell

Ply number	Material	Thickness [mm]	Orientation [°]	TsaiWu FI [-]
1	CFRP	0.32	+45	0.43
2	CFRP	0.32	-45	0.23
3	CFRP	0.32	0	0.28
4	CFRP	0.32	-45	0.13
5	CFRP	0.32	+45	0.16
6	CFRP	0.32	-45	0.06
7	CFRP	0.32	0	0.1
8	CFRP	0.32	0	0.05
9	CFRP	0.32	90	0.02
10	Aluminium 7075	4.00	-	0.01
11	CFRP	0.32	90	0.05
12	CFRP	0.32	0	0.48
13	CFRP	0.32	0	0.6
14	CFRP	0.32	-45	0.52
15	CFRP	0.32	+45	0.34
16	CFRP	0.32	-45	0.71
17	CFRP	0.32	0	0.51
18	CFRP	0.32	-45	0.92
19	CFRP	0.32	+45	0.69

Maximal failure index appears at 18th layer, which is on the outer side of the duct shell, and reaches 0.92, so any ply failure should not appear at this critical ply.

10.3.5.4 Check of inner connecting plates structural strength

Traverse beams transmit the load to the duct via connecting plates, which are bolted to the duct. Even though the parts are designed from relatively thin aluminium plates. These connecting plates have also a sleeve to which the composite traverse beams are glued, but this part of the connecting plate was included to the composite layup of the traverse beams as a 3mm thick layer of aluminium. Stresses distribution of the most critical plate is displayed in the following picture. This plate had to be strengthened by increasing its thickness to 8 mm.

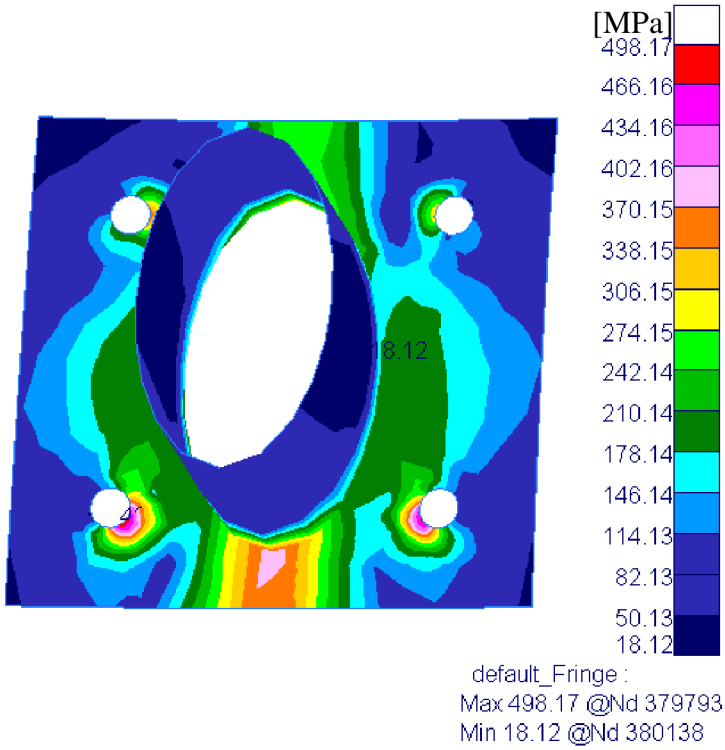

Figure 10.18 Von Mises stress distribution of inner connecting plate

$$RF = \frac{R_m}{\sigma_v} = \frac{450}{498.17} \tag{10.29}$$

$$RF = 0.90 > 1 \tag{10.30}$$

Calculation of reserve factor showed that this part should be reinforced since its value is below 1 which is mainly due to the applied safety factor for composite structures. However, when the safety factor of 1.5 is considered, resultant reserve factor reaches 1.35, which can be considered as safe enough to withstand given load. Increasing thickness of this part should improve its strength.

10.3.6 Evaluation of duct connecting plates structural strength

Strength of the plates connecting ducts to the space frame was also checked since they are also a critical part. Based on the stress distribution displayed in the following picture, main focus should be put on connecting beams, because the stress concentrates around these connections. Another weak spot are the holes connecting plate to composite duct.

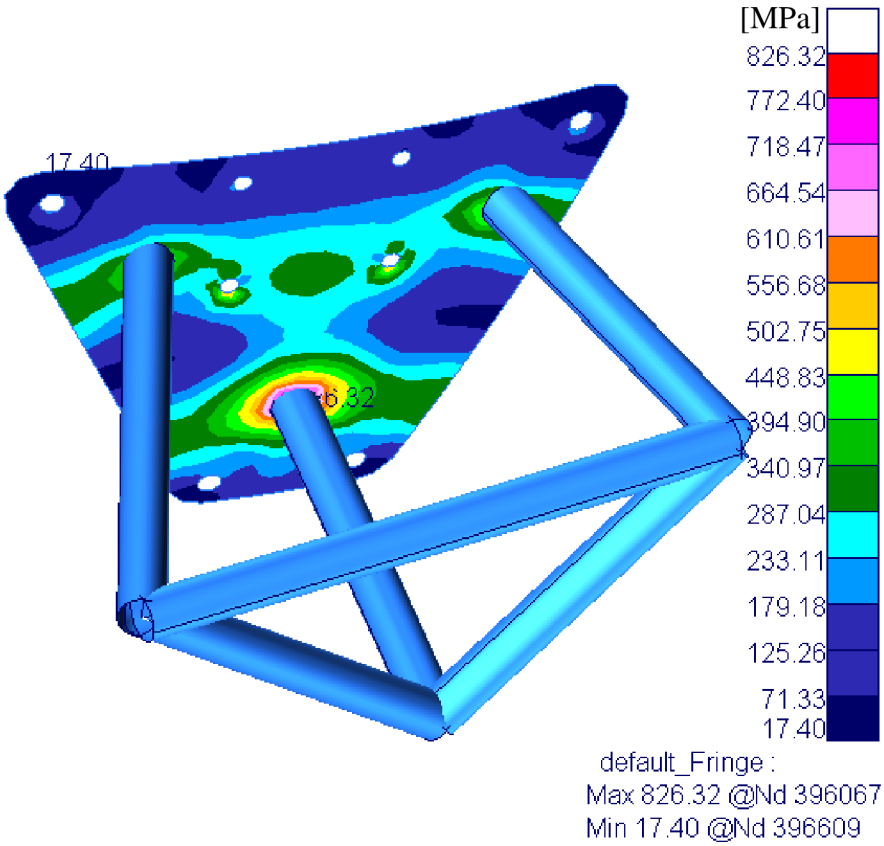

Figure 10.19 Front left duct connecting plate von Mises stress distribution

Stresses reach very high values, which are caused mainly by applying safety factor 2.25, which is used for composite structures. Since the connecting plate is considered to be manufactured from aluminium alloy, applied safety factor should be 1.5 since there is no expectation of non-linear material behaviour. Another reason, why the stress around connections reaches such high values could occur due to the connection of bar element at single node of the shell mesh. This could create a singularity.

For the determination of reserve factors, maximal stress occurring at the diameter corresponding with the beam is taken. In the distance of 20 mm from the centre of beam, which is also a connecting node, maximal stress reaches 681.02 MPa.

$$RF = \frac{R_m}{\sigma_v} = \frac{450}{718.56} \leq 1 \tag{10.31}$$

$$RF = 0.63 \tag{10.32}$$

Reserve factor is below 1, but with the application of isotropic material corresponding safety factor, reserve factor reaches 1.015. However, resultant strength of this part would be highly dependent on welds, which were not covered in this preliminary strength analysis. Reinforcement of the bottom beam should be considered in order to increase connection area. Increased thickness of the plate could also improve its strength.

10.3.6.1 Bearing and shear out

Designers of composite structures try to avoid mechanical joints as much as possible, because its including in the construction creates stress concentrations. However, mechanical joints of composite structures have many benefits. Primarily it simplifies the assembly and manufacturing, since the moulds of the composite parts do not have to be so complex. On the other hand, adhesive connections are more dependent on external influences, such as increased temperature or humidity and the assemblies are not dismantable. Holes drilled into the composite are the critical parts of the construction and may cause many different failures based on a type of loading. Following picture shows several types of failures of composites. [33]

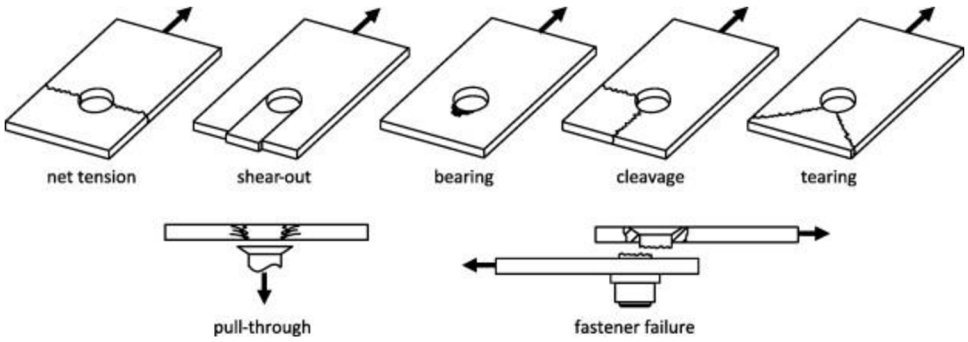

Figure 10.20 Overview of possible failures of composite mechanical joints [34]

Bearing failures

Bearing failure is a local compressive failure in material immediately beneath the loaded bolt. During this failure, bolt is pressed into the composite and corrupts the initial circular shape of the hole. Even though this failure is not critical, it can affect the construction and cause further damage.[33]

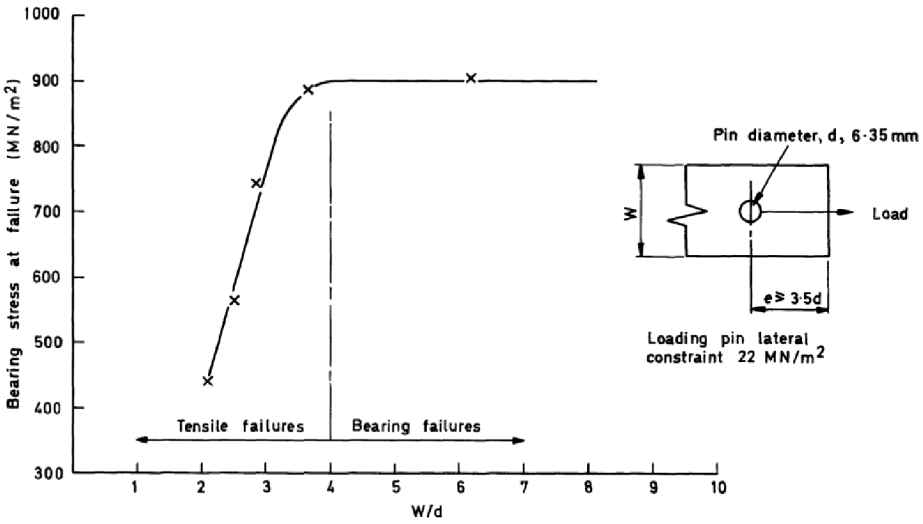

Figure 10.21 Bearing stress at failure with W/d ratio [33]

10.4 Summary

Structural analysis showed weak spots of the construction and helped to optimize it. Total mass of the space frame was reduced and with further optimization could be reduced slightly more. Space frame is structurally safe and composite ducts should be also safe with the proposed inner structure and features. However, for more accurate analysis of structural strength of composite duct, accurate corresponding material characteristics would have to be obtained. Bolted joints should be also evaluated more since the bearing and shear-out failures require testing for more accurate evaluation of their strength.

Further work could focus on overall FEM model, which would reduce the impact of isolating outer construction. Loading of the space frame would be more accurate in this case. Flight testing or detailed simulation could provide more accurate values of thrust at given maneuver and gyroscopic moments. Another loading case which was not solved during this conceptual design is landing, respectively a drop test, which is a part of certification specification requirements. In order to fulfil the requirements, landing gear with shock absorbers or leaf spring would have to be designed and integrated to the construction. However, if the advanced control system with altitude sensors is applied, landing may be performed automatically and smoothly without any significant dynamic impact, which would damage the frame.

11 CFD aerodynamic analysis of the multicopter

Computational Fluid Dynamics (CFD) is a useful tool in the conceptual phase of a design, since it allows designers evaluate aerodynamic shape of the aircraft in the very beginning of the designing process and hence find improvements quickly without needing of making prototype models for wind tunnel testing. On the other hand, results from CFD analysis should be taken with reserve since the most conservative approach is still experimental wind tunnel testing, which reflects the reality most accurately. Another big advantage of CFD analysis is its possible connection with geometrical shape optimization, which can be performed for further improvements.[35]

CFD analysis of this part of the thesis was performed using ANSYS Fluent.

11.1 Geometrical model

11.1.1 Description of geometrical model

Designed multicopter with a pilot had to be edited before the mesh generation, because there was a possibility of applying geometrical simplifications, which can be considered conservative. Main simplification was neglecting the propellers, motors and inner traverse beams of the ducts, since for the drag analysis, all these parts can be assumed as an actuator disk. Geometry of the pilot was also simplified, mainly his hands were covered in order to prevent flow between fingers. Geometry preparation and meshing was performed using ANSA, which is suitable for meshing complex 3D geometries. Following picture shows a prepared 3D model for CFD analysis.

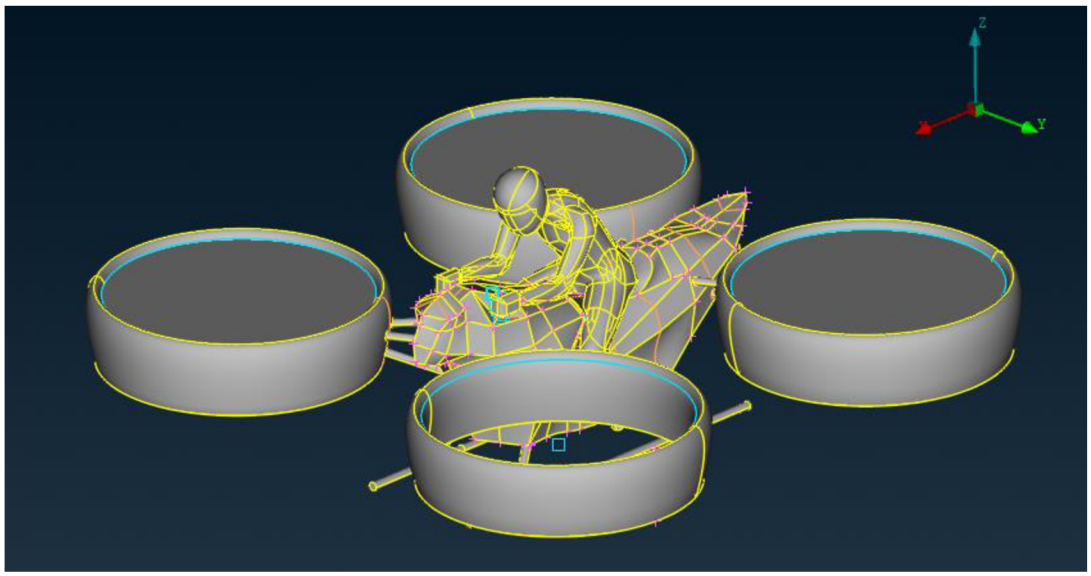

Figure 11.1 Simplified geometry for CFD analysis

Crucial part of geometry preparation is computational domain, which is a 3D space usually of cubic or spherical shape made for creating a section for computations. Its size should be adapted to the size and shape of the analysed object, Reynolds and Mach number. Considered domain of the shape is prismatic. Two sizes of domains had to be created, the first one for the ground effect analysis and the second one forward flight analysis. Cleaned and simplified model was then used for generation of surface mesh and then volume mesh [35].

11.2 CFD analysis of ground effect at hover

Rotorcrafts and even airplanes can benefit from the ground effect, which is an aerodynamic phenomenon appearing at low level flight. Rotorcraft hovering above ground can gain additional due to the ground effect. Since the streamlines of the slipstream has to copy the ground, it makes a rapid expansion of slipstream, which changes the induced velocity in the plane of the rotor. Due to the ground effect, propellers generate bigger thrust at the same power consumption. Another beneficial aspect of ground effect is landing, when the slipstream acts as an air cushion.[1]

Degree of ground effect influence depends mainly on the distance between the rotor and ground. Following picture shows the measurements of ground effect influence with respect to different distances. Propeller geometry and blade loading also affects the resultant slipstream and hence the ground effect. From the following chart it is obvious that the ground effect influence decreases exponentially with the increasing distance.[1]

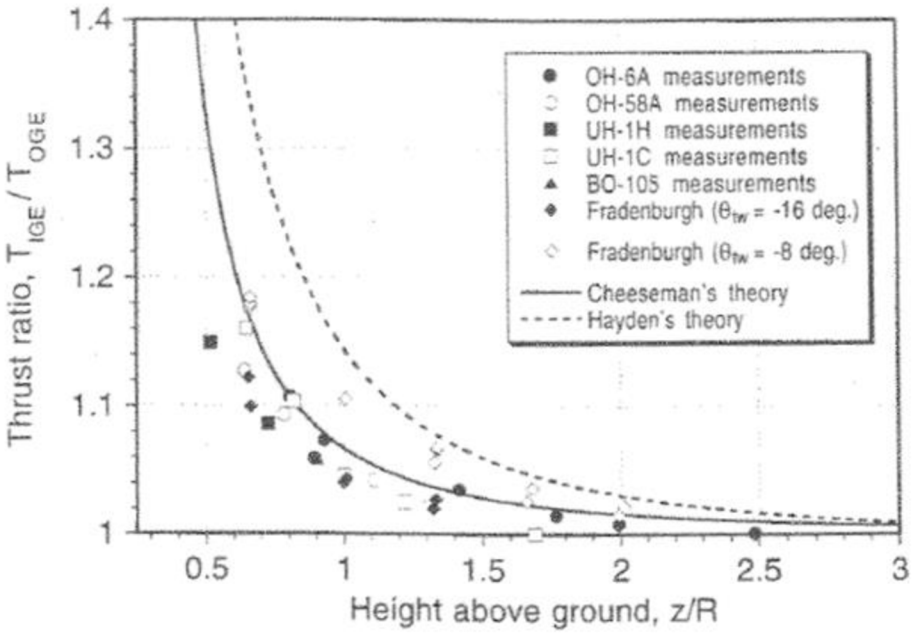

Figure 11.2 Ground effect dependency with respect to the rotor distance from the ground [1]

In order to estimate the influence of distance between the rotor and ground, three distance between the landing skis and the ground were analysed: 0 mm, 500 mm and 1000 mm. Distance between landing gear and the considered actuator disk position is 800 mm.

11.2.1 CFD mesh

Creating a mesh from the computational domain is a crucial part of CFD pre-processing, because flow properties such as velocity, pressure, temperature are computed in every element, so its refinement and distribution affect directly analysis results. From the point of view of mesh entropy, every mesh may be divided into structured or unstructured mesh. Creating a structured mesh is more time consuming and for some applications impossible to use, because of geometric complexity. For these applications, unstructured mesh is a possible way. Nevertheless, unstructured mesh is usually combined with structured mesh, which is used at more influential places of domain, e.g. near boundary layer.[35]

Domain of this case had dimension of 23383x23383x12152 mm. Mesh was created using ANSA, which is a commercial pre-processing tool suitable for meshing complex 3D geometries. Meshing procedure begins with the preparation of surface mesh of the model using triangular shell elements and then generating volume mesh using the tetrahedral elements.

Following picture shows the detail of the domain section.

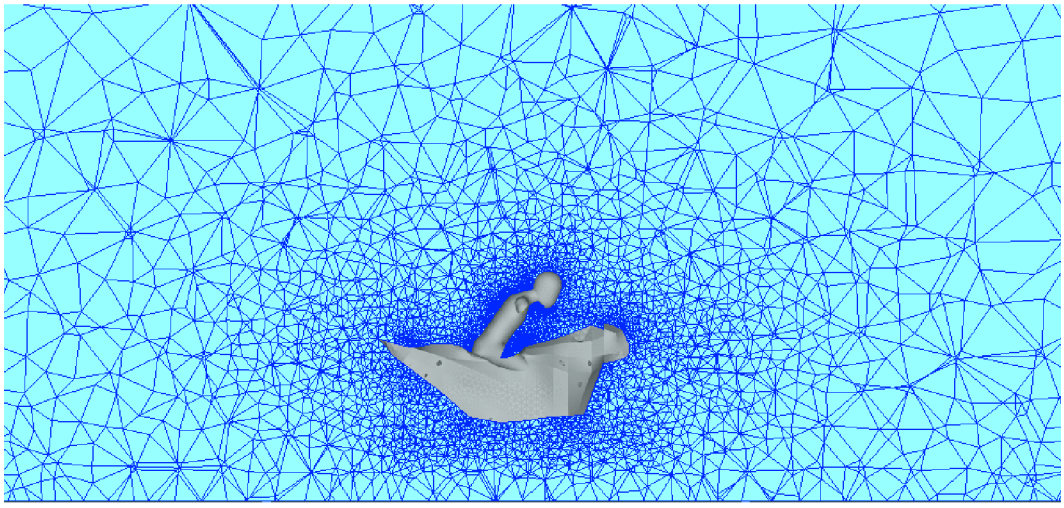

Figure 11.3 Mesh of the case for ground effect observation at 0.5 m above the ground

Main focus of mesh quality was on the ducts, which are the most influential parts of the model due to the expected highest velocity gradient. Therefore, prismatic layers were generated around ducts in order to reach y^+ value to 5.

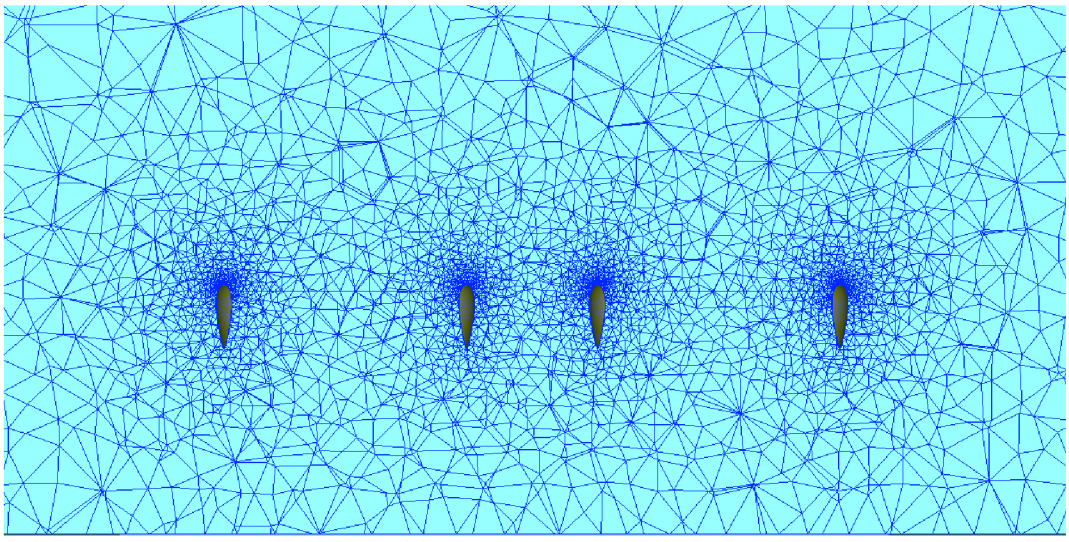

Figure 11.4 Detail on mesh refinement of ducts

Table 11.1 Number of elements of analysed cases

	Number of elements		
Case	Tetrahedrals	Pentahedrals	Total
0 m	5590363	2063355	7653718
0.5 m	6037704	2063355	8101059
1 m	6079841	2063355	8143196

11.2.2 CFD settings and turbulence model

Analysis was performed as steady state case with the usage of Spalart-Allmaras turbulence model, which is a one equation model often used in aerodynamic analysis. Pressure-velocity coupling was set to simple. Momentum and modified turbulent viscosity was set to first order upwind. Relaxation factors were set to default. Following table represents used atmospheric conditions at 0 m ISA and used gravitational acceleration.

Table 11.2 Atmospheric conditions

Air density [kg.m^{-3}]	1.225
Kinematic viscosity [m^{2}.s^{-1}]	1.46E-05
Gravitational acceleration [m.s^{-2}]	9.81

11.2.3 Boundary conditions

Ground effect analysis is a specific CFD case, where the conventional approach of inlet and outlet cannot be used. Outer walls of prismatic domain were set to pressure outlet, since the flow is generated by actuator disks. Bottom wall underneath the multicopter was set to wall. Actuator disks were simulated using fan boundary condition as described in the previous subchapter. All parts of the multicopter model and pilot were set to no-slip walls.

11.2.3.1 Actuator disk

Propellers were modelled as actuator disks, which means that the overall pressure jump is taken into account and the model is then much simpler, since there is no need to consider a dynamic rotating mesh or similar approaches. ANSYS Fluent fan boundary condition was used to model actuator disk. Since the scope of this analysis was the ground effect impact and drag analysis, this method can be taken as sufficient. Resultant thrust of contra-rotating propellers was used, so there was only one actuator disk was taken into account. Swirl of the stream, which can be set by this boundary condition was also neglected, since it is difficult to estimate.

Pressure jump can be calculated using actuator disk momentum theory of ideal propulsor. It neglects the friction and also the shape of the rotor. It is mainly based on Bernoulli equation described in section of the propulsor and also before and after it. Following picture shows the pressure distribution of the actuator disk and also considered sections.[36]

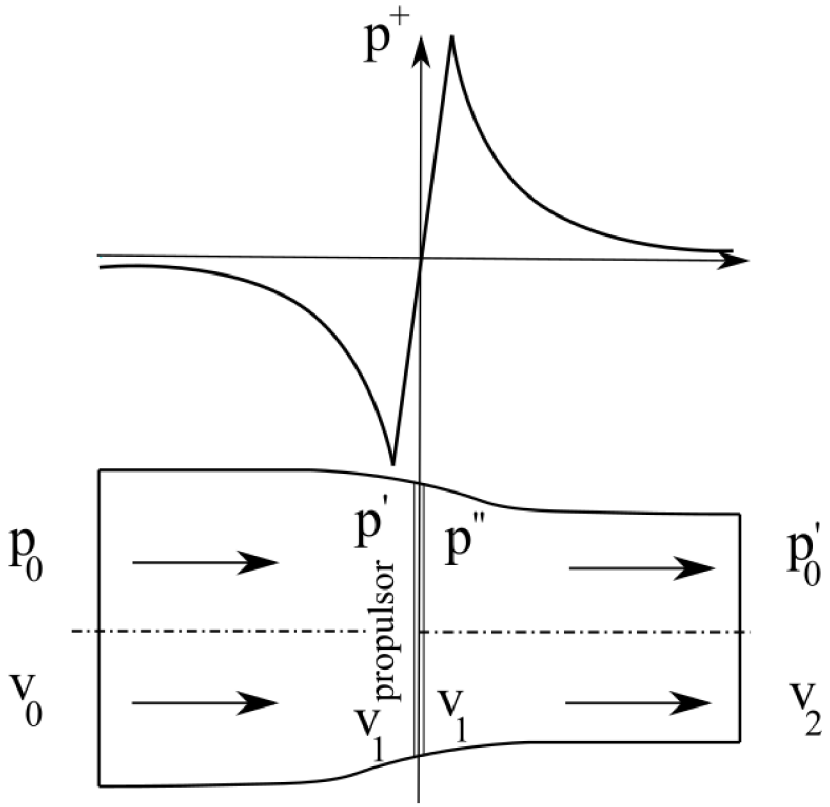

Figure 11.5 Pressure distribution of actuator disk [36]

Following equations represent Bernoulli equations applied at different sections:

$$p_0 + \rho\frac{v_0^2}{2} = p' + \rho\frac{v_1^2}{2} \tag{10.33}$$

$$p'' + \rho\frac{v_1^2}{2} = p_0 + \rho\frac{v_2^2}{2} \tag{10.34}$$

Resultant pressure difference is then equal to the difference of pressure of inlet *p'* and outlet *p''* of actuator disk.

$$\Delta p = p'' - p' = \frac{\rho}{2}\left(v_2^2 - v_0^2\right) \tag{10.35}$$

Thrust of the propeller is the equal to the multiplication of pressure difference and disk area.

$$T = \Delta pA \tag{10.36}$$

Resultant pressure jump used for fan boundary condition for one propulsor is the equal to:

$$\Delta p = \frac{T}{A} = \frac{784.8}{1.167} = 672.5\,Pa \tag{10.37}$$

11.2.4 Evaluation of results

As mentioned above, ground effect is going to be evaluated for these particular distances: 0 mm, 500mm and 1000 mm above ground.

11.2.4.1 Ground effect impact at z=0 mm

Considered actuator disks, placed to the position of top propellers, are in the distance of 800 mm from the bottom part of landing ski, therefore the ground effect should have marginal effect during take-off. Following pictures depict velocity magnitude and static pressure of front rotors.

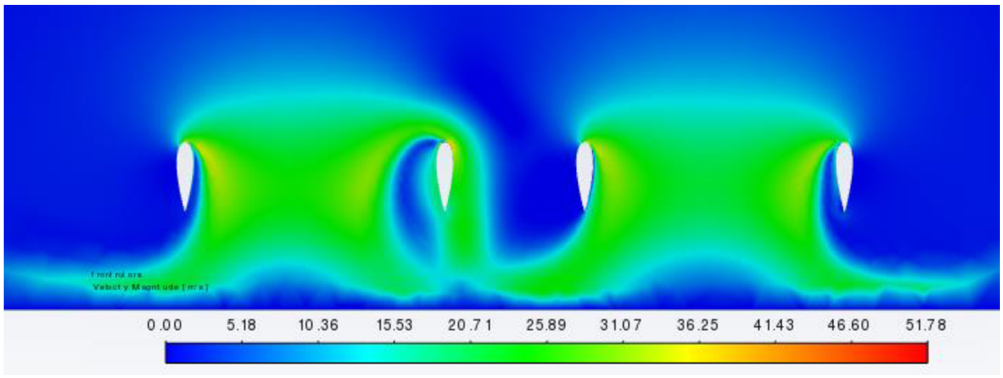

Figure 11.6 Velocity distribution [m/s] around front rotors at 0 m above ground

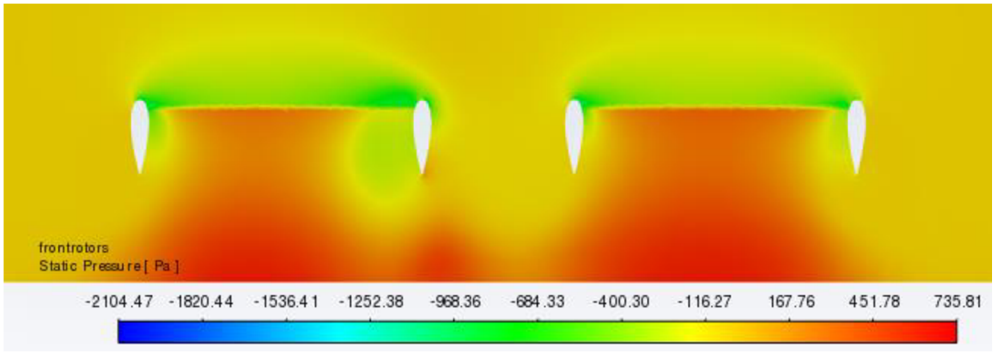

Figure 11.7 Static pressure [Pa] of front rotors at 0 m above ground

Around adjoining part of the duct, the flow is highly impacted by adjacent rotor and on the inner side there is a sign of separation of the flow, which is probably created by the interference of contradictory flows. Static pressure reaches highest values out of all analysed cases, which is redeemed by lower velocity magnitude. Next set of pictures present velocity and static pressure distribution around rear rotors.

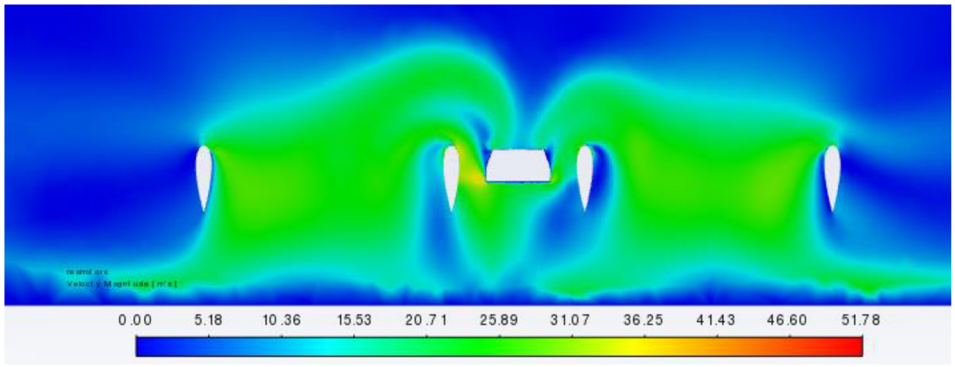

Figure 11.8 Velocity distribution [m/s] around rear rotors at 0 m above ground

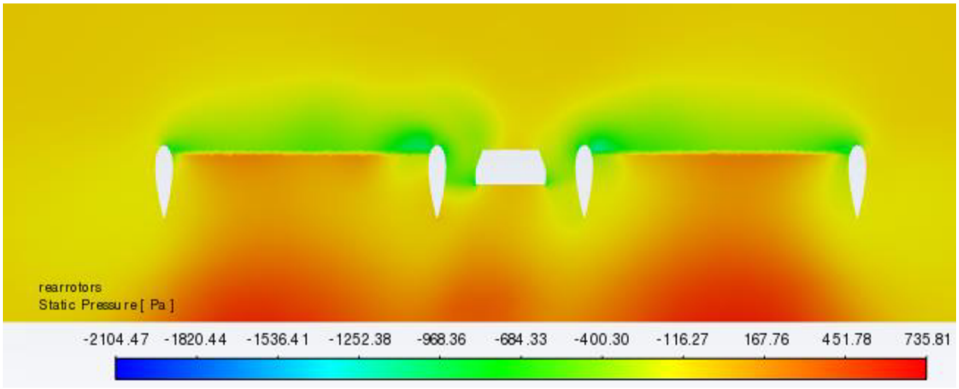

Figure 11.9 Static pressure [Pa] of rear rotors at 0 m above ground

Flow around the multicopter can be considered as very turbulent and the interference between rotors is the strongest of all three analysed cases. In order to verify the results and confirm the strength of interference between the rotors, transient analysis would have to be performed. However, in the conceptual phase obtained results are sufficient for initial estimation.

Overall additional force in vertical direction due to ground effect is 858.57 N.

11.2.4.2 Ground effect impact at z=500 mm

Increasing distance affects the impact of ground effect. Second distance equal to 500 mm above ground, when the actuator disks are 1300 mm above ground, already show the reduced additional thrust. Following pictures show the velocity magnitude and static pressure distribution of front rotors.

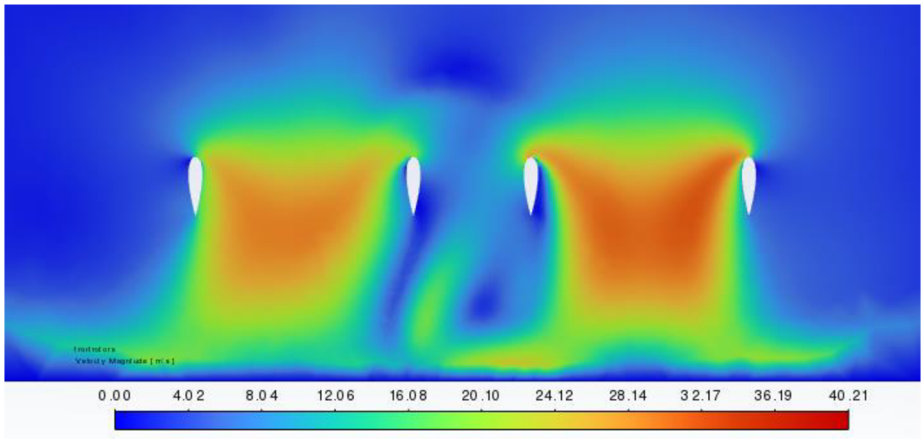

Figure 11.10 Velocity distribution [m/s] around front rotors at 0.5 m above ground

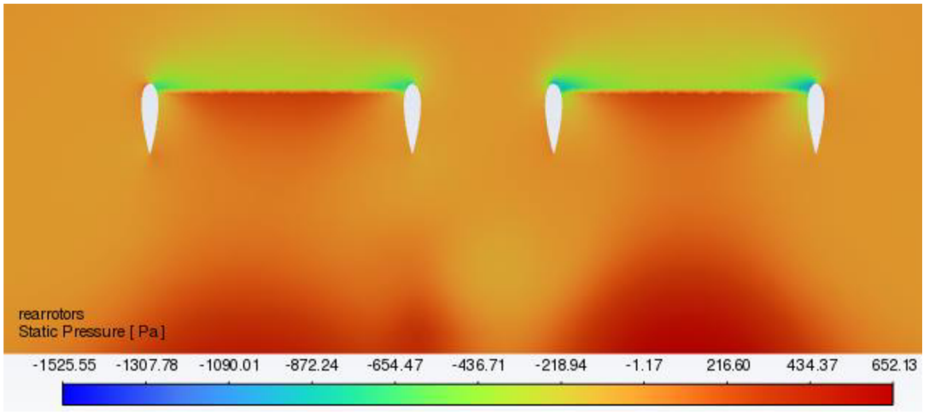

Figure 11.11 Static pressure [Pa] of front rotors at 0.5 m above ground

Following picture representing velocity field and static pressure of rear rotors show that the flow exhibits nearly symmetrical behaviour.

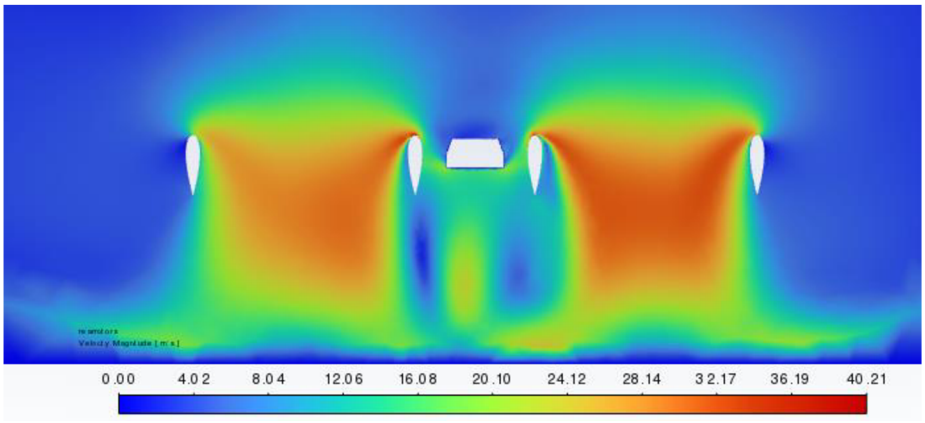

Figure 11.12 Velocity distribution [m/s] around rear rotors at 0.5 m above ground

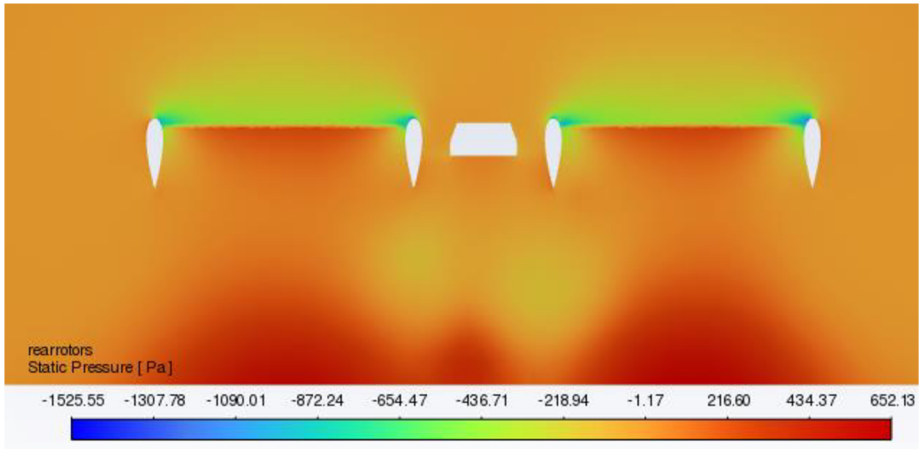

Figure 11.13 Static pressure [Pa] of rear rotors at 0.5 m above ground

Flow at this distance seem to be less turbulent and the interference between adjacent rotors seem to be weakened. Following picture shows the streamlines leaving propeller ducts and its colour represents velocity magnitude.

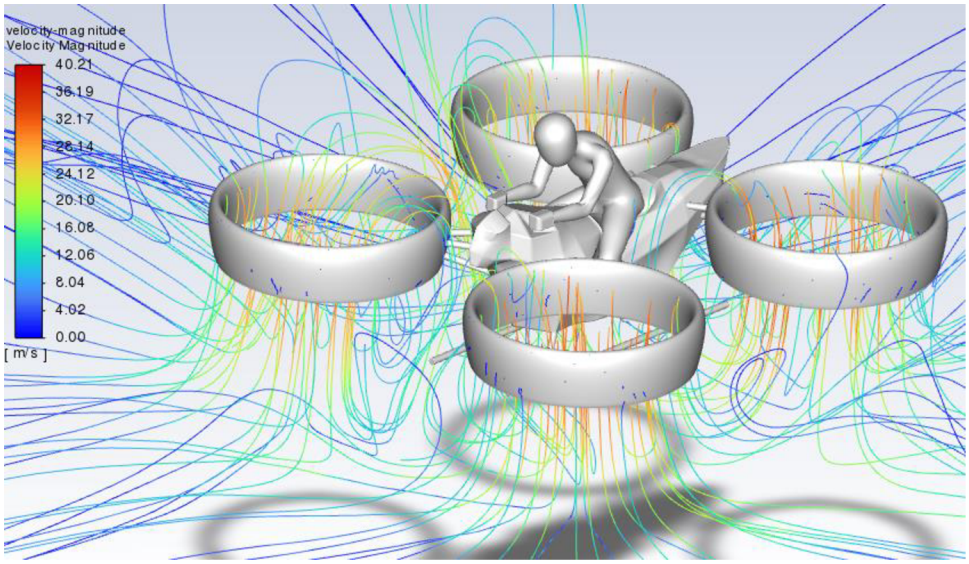

Figure 11.14 Velocity magnitude [m/s] displayed on streamlines around rotors at 0.5 m above ground

Overall additional force in vertical direction due to ground effect is 763.8 N, which can be considered as a high value with respect to the distance.

11.2.4.3 Ground effect impact at z=1000 mm

Last analysed distance above ground was 1000 mm. At this distance, actuators discs are in the distance of 1800 mm. Following pictures show velocity field and static pressure of front rotors.

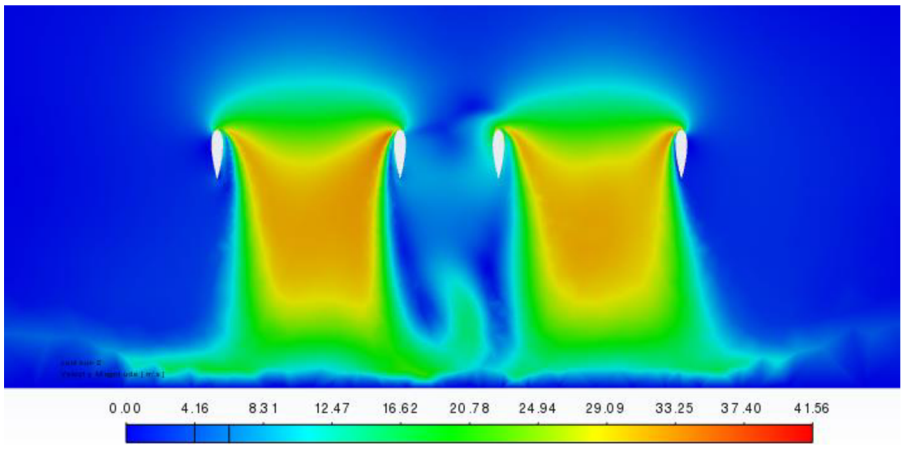

Figure 11.15 Velocity distribution [m/s] around front rotors at 1 m above ground

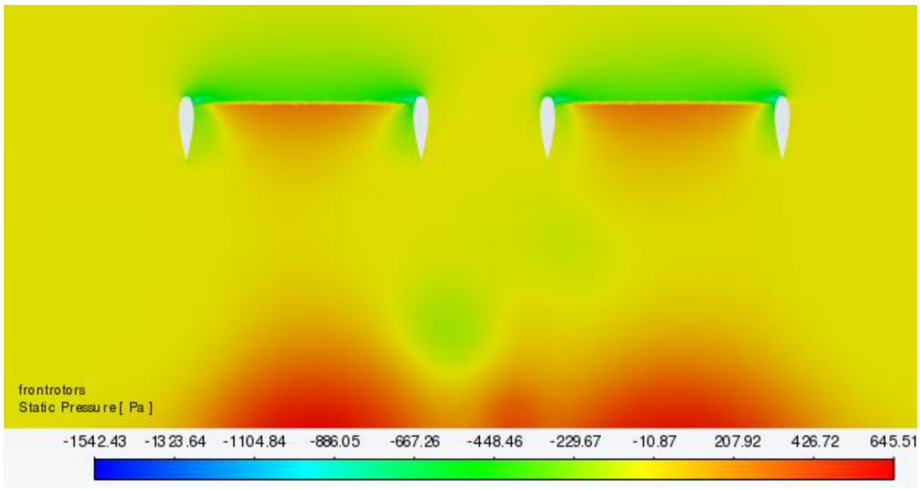

Figure 11.16 Static pressure [Pa] of front rotors at 1 m above ground

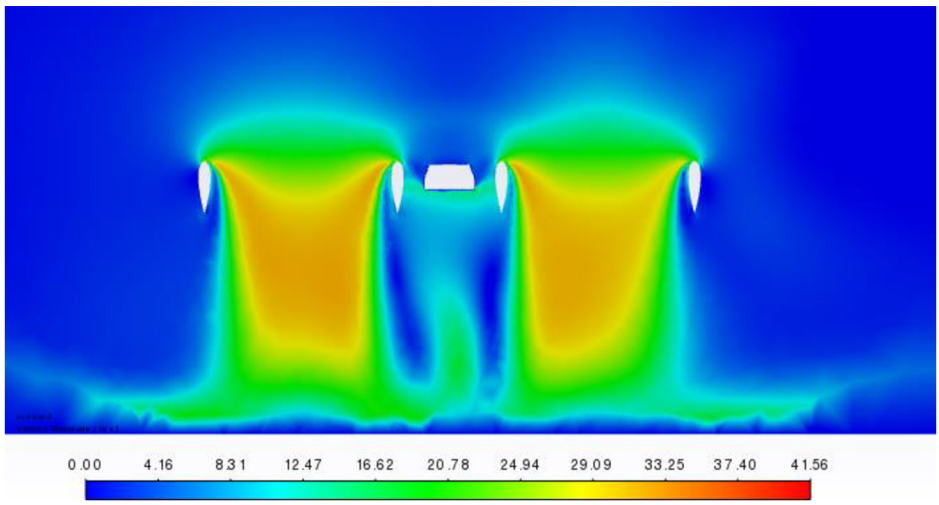

Figure 11.17 Velocity distribution [m/s] around rear rotors at 1 m above ground

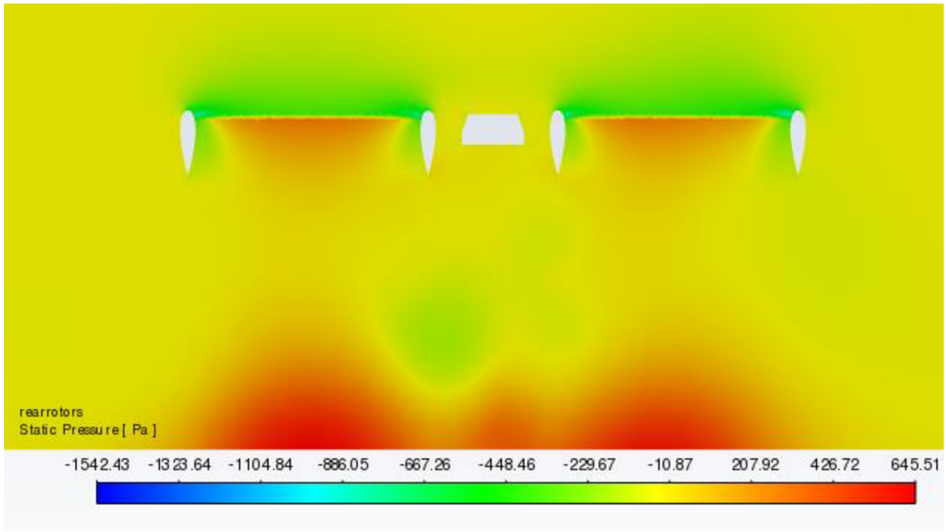

Figure 11.18 Static pressure [Pa] of rear rotors at 1 m above ground

Even in this distance flow below rotors is still relatively directed by ducts and does not begin to spread out before reaching the ground, which is beneficial from ground effect point of view. From the picture of static pressure, it is evident that hypothetical air cushion bellow the multicopter is weaker compared to closed distances. Nevertheless, overall additional force in vertical direction due to ground effect reaches 625.7 N.

11.2.5 Summary

CFD analysis corresponded with the expected trend, which is based on the decreasing thrust with increasing distance as shown at figure 11.5. However, nominally the results reach higher values of thrust ratios, which may arise from the usage of ducts, which direct the flow and standalone generate additional thrust.

Simplification of contra-rotating configuration could also affect the results. Swirl, generated by propellers is partially eliminated by the propellers themselves as they are contra-rotating, but a residual flow swirl persists and may affect the flow around the ducts and the whole multicopter.

Following chart depicts the resultant dependency of thrust ratio between thrust in ground effect and thrust out of ground effect on proportional distance from the ground. Reference thrust out of ground effect T_{OGE} was taken as the required hover thrust used for the calculation of pressure jump. Impact of the ducts was not quantified and its influence is covered in the results of in-ground-effect values of thrust.

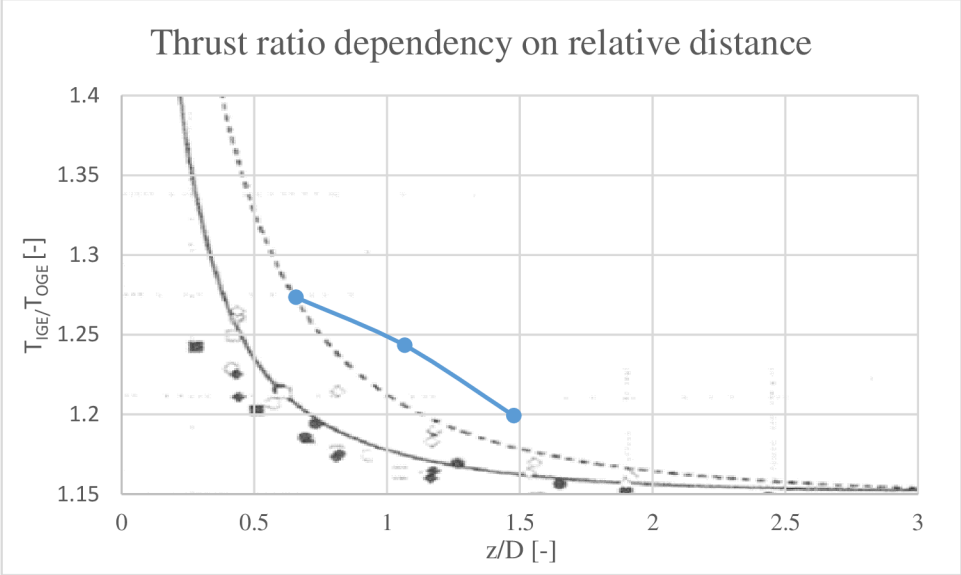

Figure 11.19 Results of thrust ratio dependency on relative distance from the ground compared with results from [1]

In order to evaluate ground effect influence on battery endurance, calculation procedure described in chapter 7 and 12 was used. Ground effect influence was estimated by reducing required hover thrust by a thrust addition due to ground effect.

Flow interference between ducts showed that the rotors may significantly influence each other. This interference may have a negative impact on the stability. In order to verify the results, cases with finer meshes could be created. Accuracy of the results was also highly dependent on the usage of fan boundary condition, where a flow swirl and an impact of contra-rotating propellers was neglected. However, this phenomenon would have to be confirmed with transient CFD analysis. In the appendix, static pressure distribution at the multicopter symmetry plane can be observed.

11.3 ESTIMATION OF AERODYNAMIC DRAG DURING FORWARD FLIGHT

Estimation of aerodynamic drag is crucial for the performance calculations of any aircraft. For conventional airplanes, some assumptions and estimations can be used in order to calculate parasitic drag. However, for unconventional aircrafts such as multicopters do not exist any empirical model of drag estimation yet. Unfortunately, these models also neglect some factors, such as induced drag. In order to obtain values of drag coefficients for different pitch angles. These data could be further used for forward flight performance calculations. Multicopter drag was observed without an impact of ground effect. Multicopter drag was observed without an impact of ground effect.

11.3.1 Domain and mesh

In case of forward flight drag estimation, a domain with different dimensions was used. Compared to ground effect analysis, domain has to offer enough space behind observed geometry. Multicopter body in the middle vertical position of the domain in order to isolate impact of ground effect.

Following picture shows the prepared domain for the analysis of forward flight. Dimensions of the domain were 40000x23383x21158 mm. Multicopter was rotated by various angles, therefore results for different pitch angles could be obtained. A new mesh was generated for each of the configurations, so the inlet velocity was still parallel to the domain longitudinal edges of the domain.

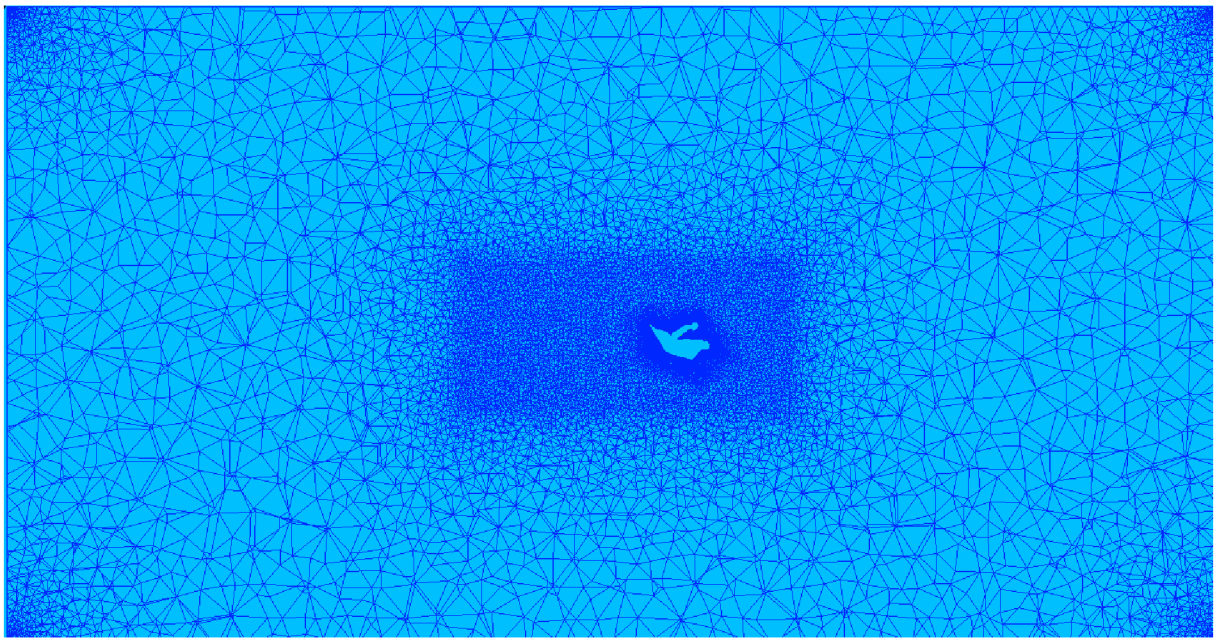

Figure 11.20 Mesh for 20° pitch case

Mesh in this analysis was finer compared to previous CFD analysis. Prismatic layers were generated in order to catch influence of boundary layer.

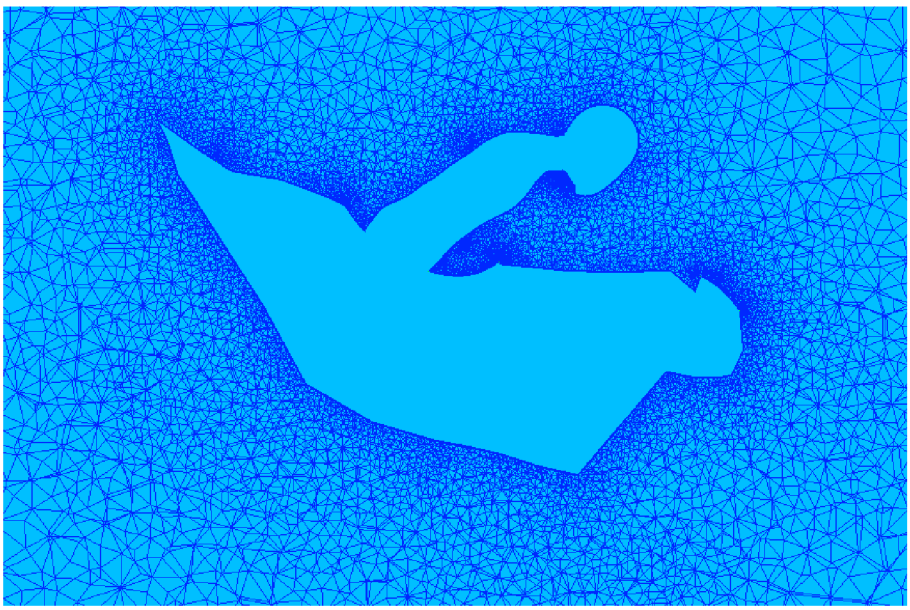

Figure 11.21 Mesh refinement around model body

Table 11.3 Number of elements of analysed cases

	Number of elements		
Case	Tetrahedrals	Pentahedrals	Total
10°	10 872 066	3 950 135	14 822 201
20°	10 865 024	3 950 135	14 815 159
30°	10 868 682	3 950 135	14 818 817

11.3.2 CFD settings and boundary conditions

Considering the CFD settings, the turbulent model Spalart-Allmaras was used as in previous ground effect analysis. Pressure-velocity coupling was set to simple, momentum and modified turbulent viscosity were set to first order upwind. Relaxation factors were set to default. Atmospheric conditions were taken as mentioned in table 11.2.

Front face of the domain was set to velocity inlet. Side faces of the domain were considered as no-slip walls and rear face was set to pressure outlet.

Since multicopter forward flight speed depends both on the pitch angle and thrust distribution between front and rear rotors, this case can be considered as a complex parametric case. In order to precisely estimate drag for each observed pitch angle, dynamic simulation would be needed, so the speed estimation and forces could be calculated more accurately. Due to the conceptual character of this work, constant thrust for all rotors was taken into account.

Forward flight velocity at the given pitch angle had to be estimated based on the force equilibrium. Therefore, two iterations of CFD analysis had to be performed. In the first iteration, which helped to estimate drag coefficient, constant speed and thrust of actuator disks was considered for all pitch angles. Force equilibrium represented by following picture was used for the calculation of thrust and drag. Generated thrust has to balance drag and gravity of the multicopter, as following picture shows.

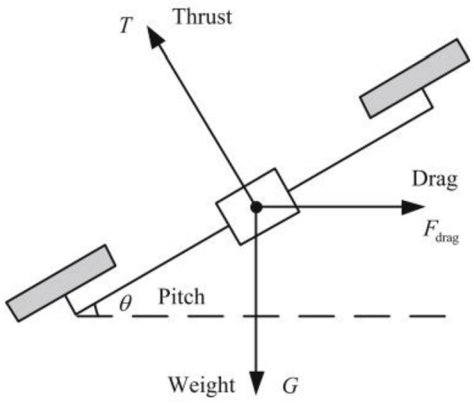

Figure 11.22 Forces on a multicopter in forward flight [6]

From the picture it is possible to derive following equations of force equilibrium.

$$F_{drag} = G \tan\theta \tag{11.1}$$

$$T = \frac{G}{n_r \cos\theta} \tag{11.2}$$

Force equilibrium was computed with considered MTOW 320 kg and results of first iteration of CFD analysis performed at constant speed 22 m/s are shown in the following table. Maximal propeller thrust was considered as 400 kgf, which equals to 840.3 Pa of pressure jump per actuator disk using equation 11.5.

Table 11.4 Results of force equilibrium and inlet velocity based on drag coefficient estimate

Case	Thrust [N]	Drag [N]	Drag coefficient estimate [-]	Inlet velocity [m/s]
10°	3187.64	553.62	0.3086	12.69
20°	3340.70	1142.67	0.2795	19.15
30°	3624.88	1812.51	0.2443	25.80

11.3.3 Evaluation of the results

Following picture shows velocity field around the multicopter. Flow acceleration due to the pressure jump of actuator disk can be observed. Picture combines streamlines flowing at symmetry plane and the plane intersecting ducts centres.

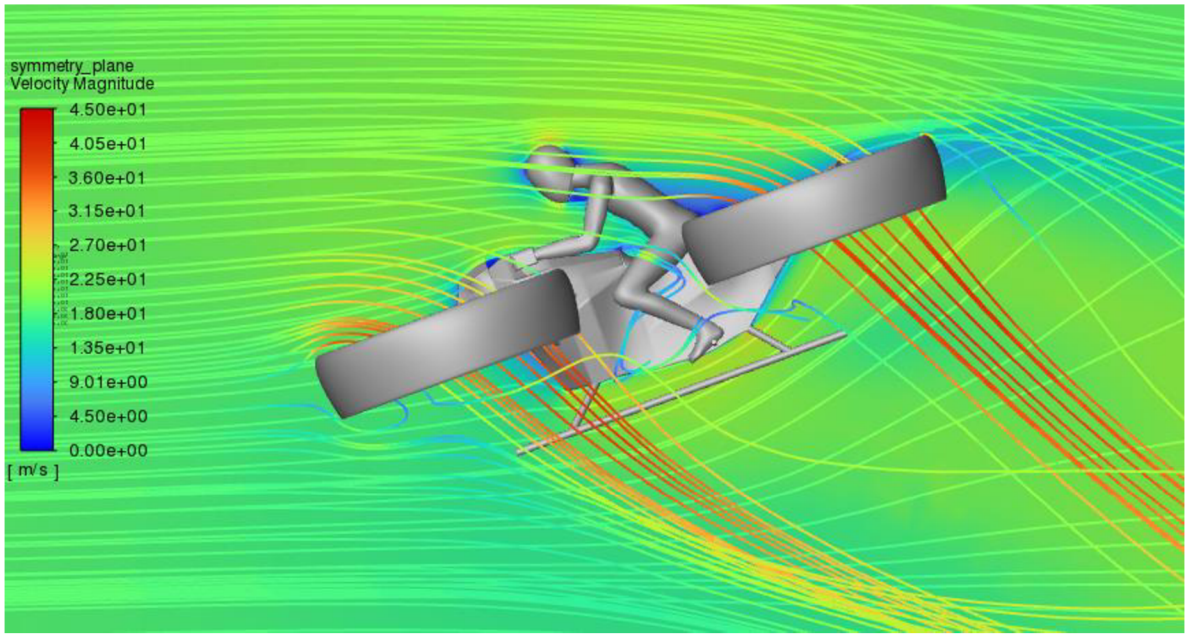

Figure 11.23 Velocity field around multicopter at 20° pitch angle

Distribution of pressure coefficient helps to understand the decreasing drag coefficient with increasing pitch angle. It is obvious that the most significant stagnation is developed in ducts. Increasing pitch angle increases angle of attack and static pressure on ducts decreases.

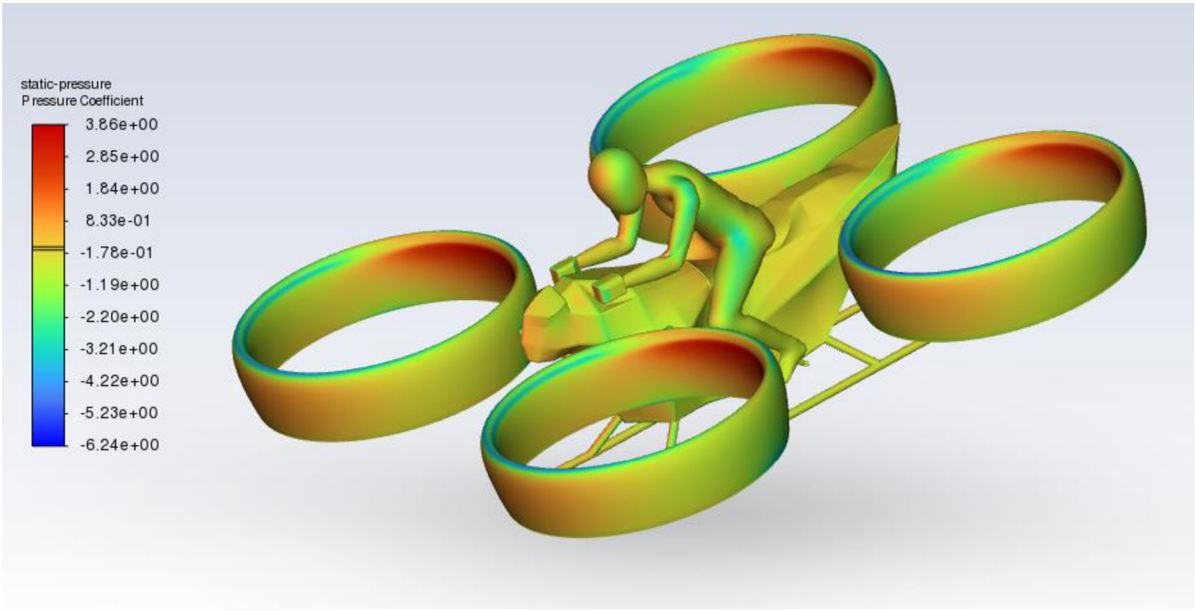

Figure 11.24 Pressure coefficient distribution on multicopter at 20° pitch angle

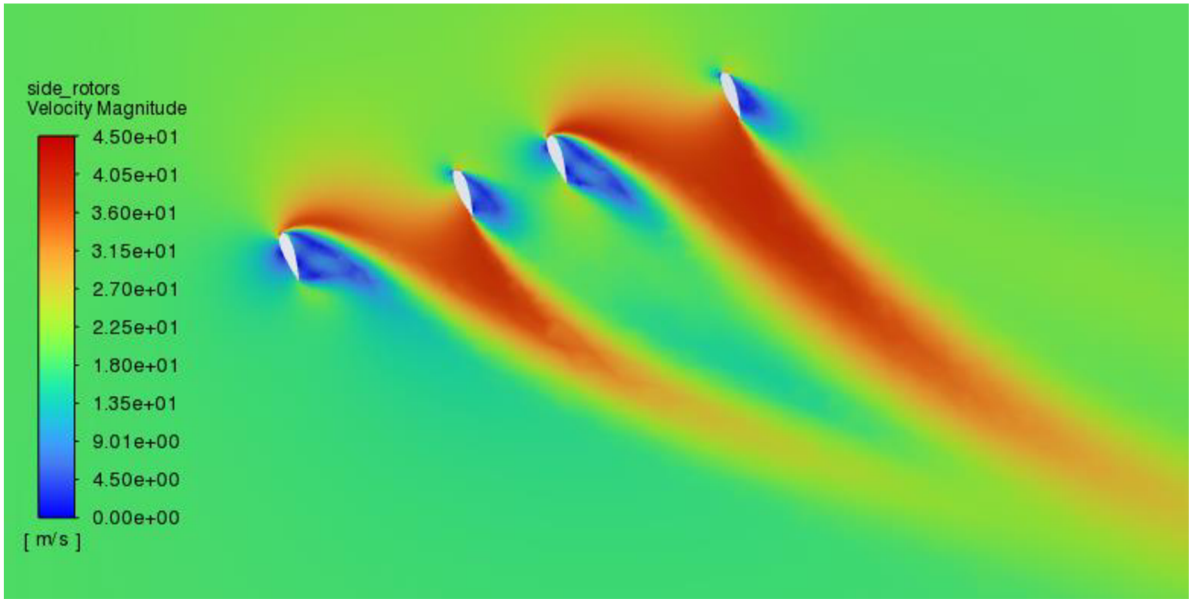

Figure 11.25 Velocity magnitude around ducts at 20° pitch angle

In order to be able compute aerodynamic coefficient, reference area of an object is needed. In case of drag coefficient of multicopter, total area of 3D model was computed in Fluent and used as a reference value for this calculation. This area has a value of 18.2 m^2.

Following table covers the results of drag and drag coefficient.

Table 11.5 Drag and drag coefficients at different pitch angles

Case	Drag [N]	Drag coefficient [-]
10°	532.84	0.2967
20°	1145.69	0.2803
30°	1907.05	0.2570

From the results it is evident, that drag coefficient decreases with increasing pitch angle. This is probably mainly due to the ducts. Angle of attack of the duct inflow increases and hence the drag coefficient decreases. Increasing pitch angle also reduces the frontal area of the ducts and the flow is capable of flowing through ducts.

Obtained data were used for calculation of forward flight performance described in the following chapter. In order to obtain more accurate values of drag, multiple iterations would have to be performed for more pitch angles. This work did not solve sideward flight, which is possible for multicopters. In that case, drag coefficients for different roll angles would have to be computed.

12 FLIGHT PERFOMANCE CALCULATION

Basics of the multicopter flight mechanics were covered in chapter 4. Since multicopter is a rotorcraft hovering is a main flight phase. It can be evaluated mainly by a required hover thrust and maximal achievable thrust. Forward flight of the multicopter was evaluated mainly from the flight endurance point of view, which is dependent directly on the battery and the forward flight speed hence pitch angle. This analysed dependency of flight speed also helped to find optimal pitch angle for maximum flight endurance and to define maximal speed for the given pitch angle, which is set due to the safety.

12.1 Hovering flight mode

As previously described, hovering is a state, when the multicopter does not move in the horizontal manner and hovers at the certain altitude level. It is also a minimal thrust, which is needed for a multicopter to leave the ground during take-off. Calculation of the propeller thrust was discussed in the chapter 7 together with motor model, which was used also in this chapter.

12.1.1 Battery endurance

Flight endurance and also a flight range is dependent mainly on the battery, which should contain enough capacity to fulfil a flight mission. For the most accurate simulation of a battery state of charge, an equivalent circuit would have to be created. However, since the discharge process of Li-ion batteries is nearly linear at the wide range of discharge, it can be estimated by a following relationship stated in [6], from which it follows that endurance depends not only on capacity but also on the current flowing through battery, which is a sum of motor currents computed via motor model.

$$t = \frac{C_b - C_{MIN}}{I_b} \cdot 60 \left[\text{min}\right] \tag{12.1}$$

Initial maximal capacity is denoted C_0 and C_{MIN} is the safety reserve of battery capacity, which should not be crossed either because of the danger of the lack of voltage to motors in the middle of flight or the battery life itself, which could be affected by crossing this minimal capacity. Consumption of the battery power is represented by the current flowing through battery I_b, which is the resultant current of motors, ESCs, control devices and sensors.

Following chart depicts the discharge profile of a Li-ion battery and the stated dangerous drop in voltage at higher state of discharge.

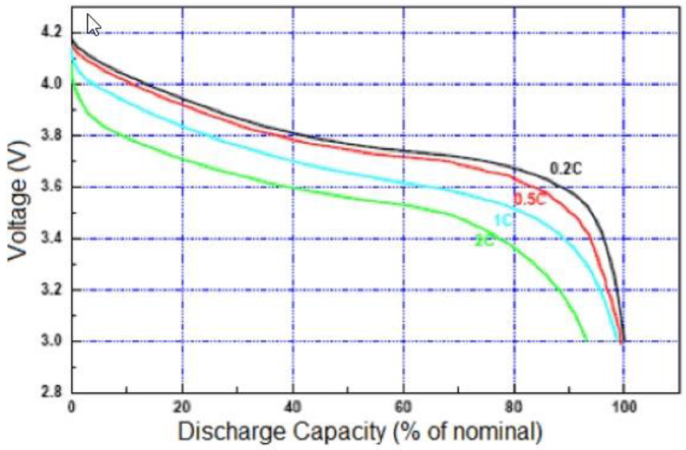

Figure 12.1 Discharge curves of Li-Ion batteries [37]

In the following table one can find the resultant endurance of different weight configurations. Hovering endurance does not depend on the drag coefficients as at the forward flight, so this numbers can be considered more accurate. Hovering endurance is an important flight performance indicator at the conceptual phase of a design to lay down the needed battery capacity.

Table 12.1 Hover endurance OGE with different payload configurations

Payload configuration	Hover endurance [min]
#1 (100 kg)	19.3
#2 (85 kg)	21.7
#3 (60 kg)	23.6

12.1.2 Ground effect influence on hover endurance

In order to evaluate ground effect influence on battery endurance, calculation procedure described in chapter 7 and 12 was used. Ground effect influence was estimated by reducing required hover thrust by a thrust addition due to ground effect. Following chart shows the results for different distances from the ground and different payload configurations.

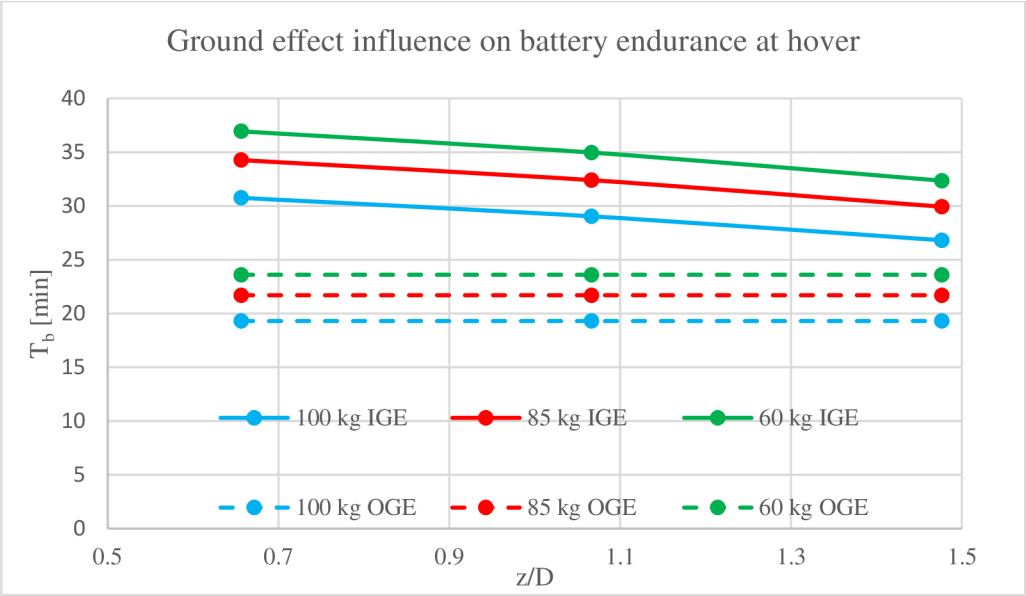

Figure 12.2 Ground effect influence on battery endurance at hover

12.2 Forward flight - Cruise flight mode

12.2.1 Velocity dependency on pitch angle [6]

Multicopter does not only hover and for its maneuvers needs certain amount of extra thrust, which may be generated to accelerate. This maximal thrust was estimated from the propeller manufacturer recommendation to be 60 kgf.

Maximal speed of a multicopter can be calculated for every pitch angle and payload configuration. Speed is determined from the equilibrium of the three main force that act on a multicopter body, which are thrust, gravity and drag, which can be calculated by the following equation.

$$v_{FF}(\theta) = \sqrt{\frac{2G\tan(\theta)}{\rho S c_D}} \tag{12.2}$$

Drag coefficient was obtained via CFD analysis described in the previous chapter. Based on the computed drag coefficients at different pitch angles, interpolated curve was created and used for computation of speed dependency on pitch angle.

12.2.2 Battery endurance

In order to calculate battery endurance of the multicopter, propulsion system model described in the chapter 7 had to be used to determine the power consumption. From the force equilibrium 11.1 and thrust equation 7.5 it is possible to calculate rotational speed of propellers at given pitch angle and weight configuration. Rotational speed of the motors is equal.

$$N = 60\sqrt{\frac{G}{\rho c_T D_p^4 n_r \cos\theta}} \tag{12.3}$$

Beside the rotational speed, mechanical power is also dependent on the propeller torque, which can be calculated using following equation.

$$M = \frac{Gc_M D_P}{c_T n_r \cos\theta} \tag{12.4}$$

Using mentioned motor model at chapter 7, electrical current can be computed using motor characteristics, torque and rotational speed. Motor voltage is taken as constant 75 V. Hour endurance can be then calculated using equation 12.1.

Using mentioned approach, it is possible to compute endurance for different pitch angles, but also for different weight configurations. Following picture represents resultant dependencies.

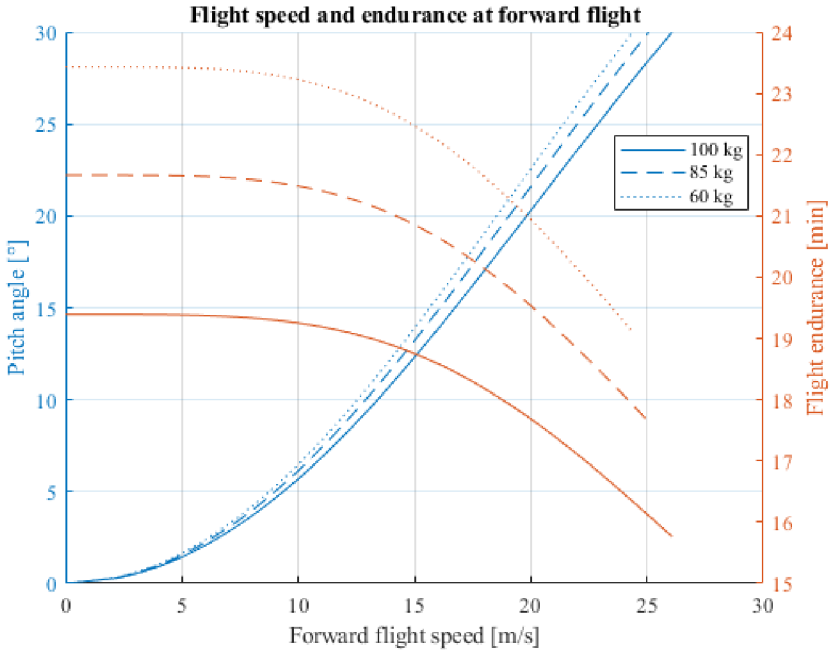

Figure 12.3 Flight speed and endurance dependency on pitch angle

From this dependency it is possible to easily derive reachable flight distance by multiplying previously computed flight endurance and forward speed.

Obviously, the highest endurance is reached in hover, for the forward flight, maximal speed for the highest endurance was deducted from the following chart, which shows the dependency of electric power on flight speed. Ideal speed for maximal endurance was taken as a speed, where the difference of electric power from hover conditions overcame 1 %.

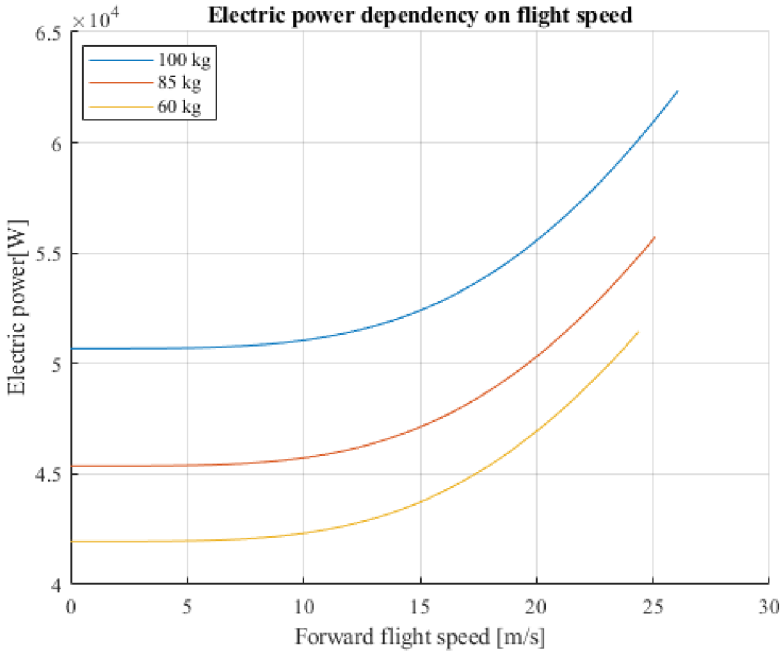

Figure 12.4 Dependency of total electric power on flight speed

Table 12.2 Maximal forward flight endurance

Payload configuration	Ideal speed for maximal endurance [m/s]	Flight endurance [min]
Payload variant 1 (110 kg)	11.10	19.2
Payload variant 2 (85 kg)	10.67	21.4
Payload variant 3 (60 kg)	10.38	23.2

With the heaviest pilot, it is possible to flight for 19.2 min, which almost complies with initial requirement of 20 min. Lighter pilots can fly slightly longer. Ideal speed for maximal endurance is around 11 m/s.

12.2.3 Flight range

Previously computed data may be used to calculate flight range for different forward flight speeds for which battery endurance is determined. Again, flight range was calculated for all three payload configurations. Flight range may be calculated using simple equation as follows.

$$R = 0.06 \cdot v_{FF} \cdot t_B \left[km \right] \tag{12.5}$$

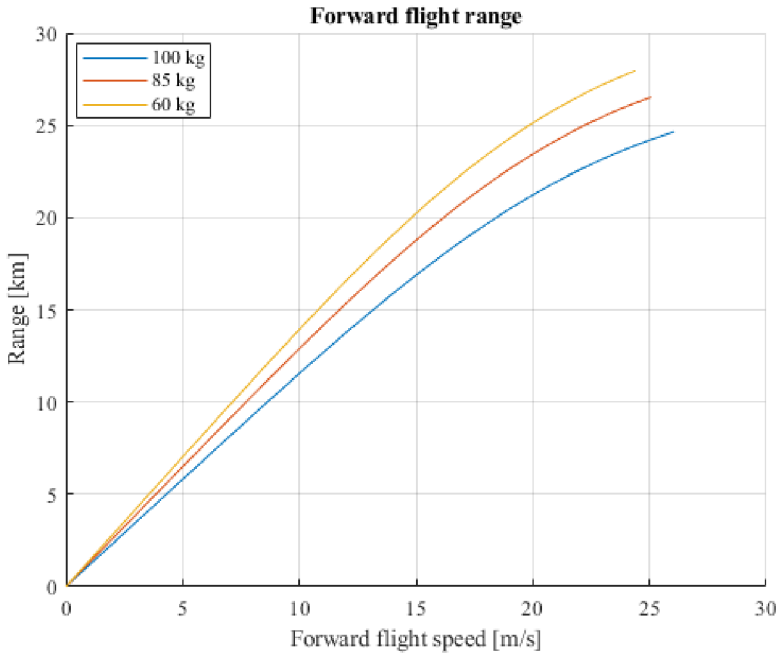

Figure 12.5 Flight range at different payload configurations and speeds

Maximal range is reached with the maximal forward flight speed.

Table 12.3 Maximal flight range of different payload configurations

Payload configuration	Maximal range [km]
Payload variant 1 (110 kg)	24.65
Payload variant 2 (85 kg)	26.54
Payload variant 3 (60 kg)	27.96

12.2.4 Maximum speed in forward flight

Maximal speed of a multicopter is reached at the maximum pitch angle θ, which was determined as 30° to ensure the safety of UAM vehicle since the bigger pitch and roll angles increase the risk of the loss of stability and possibility of pilot falling off. Maximal speeds for payload configurations can be found in the following table.

Table 12.4 Maximal flight speed at 30° pitch angle for different payload configurations

Payload configuration	Maximal speed [m/s]
Payload variant 1 (110 kg)	26.1
Payload variant 2 (85 kg)	25.1
Payload variant 3 (60 kg)	24.4

13 MULTICOPTER CONTROL SYSTEM

Multicopters, as any other aircraft, are highly dependent on its flight control system, since it differentiates rotational speeds of each propeller separately and failure of one propulsion system may lead to a catastrophic event. Conventional UAS are controller via transmitter, which communicates with receiver on the platform. Therefore, direct control of UAS is relatively limited. Designed multicopter carries the pilot, so there is no need to transmit control signals remotely.

13.1 Proposal of flight controller

Controlling multicopter flight may be a challenging task since one has to control compound movement along three axis and also rotations around them. Description of multicopter movement was already discussed in chapter 4. Key element of the flight controller is the flight computer, which has to be semi-automatic since pilot would not be able to manage propulsion systems separately. Second key element is flight controller handles, which can be either considered as joysticks or other way, which allows pilot to control multicopter movement. Two proposals of flight controller are presented. Important design factor should be a rigidity and structural strength of the flight controller since pilot's stability depends on firm grip.

Proposed concept counts with the usage of LCD screen, which would display flight data such as flight speed, attitude angle, altitude, height above ground, battery capacity and possibly also GNNS map.

13.1.1 Flight computer

Multicopter flight is dependent on thrust coupling of multicopter rotors is a complex task, which requires a semi-automatic autopilot, which computes multicopter current attitude state and gives transmits signal to relevant motors to perform given maneuver on pilot's demand. Unfortunately, it was not possible to find a flight computed, which would be fully compatible with designed UAM multicopter, so similar solution for smaller multicopters was chosen for description of connections. As a suitable flight computer, Pixhawk 5 was taken. It is important to mention that this solution should be considered only for experimental prototype and full scale multicopter testing with a pilot would require certified hardware.

Pixhawk 5 is a open-source flight controller, which is suited for RC and drones solutions. It includes several sensors, which help to define multicopter's position in space. It was chosen mainly for its versatility and 8 PWM outputs, which are required for coaxial quadcopter. Connection of GNNS systems is also advantageous. It can be set to fully automatic regime. Battery management is problematic since Pixhawk power module is built for lower voltage, so customized power modul would have to be considered.[38]

13.1.2 Joysticks

First variant of flight controller handles consists of two joysticks, which control tasks are separated. Each joystick defines different movements by tuning the joystick along different axis. Actions of the joystick should be possible to be inverted depending on the pilot's habits. Following picture represents the first proposed concept of flight controller.

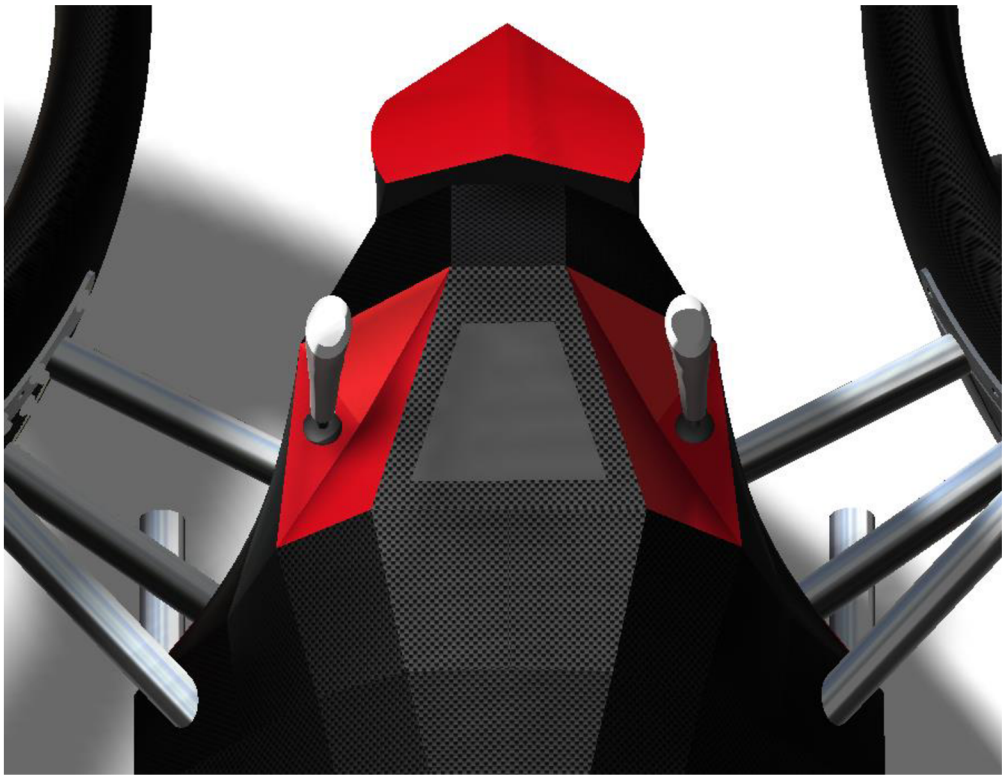

Figure 13.1 Flight control proposal #1 - joysticks

Beside the throttle, hence vertical movement in space, which is usually controlled by up to down movement of left joystick, it also provides the control of yawing, which is defined as a joystick movement from left to right. Right joystick controls rolling and pitching. Rolling is achieved by moving the joystick left to right and pitching by vertical movement of the joystick.[6]

As the conventional multicopter flight controller, the proposed flight controller should contain several buttons with defined functions. One of them could be activating autopilot or automatic stabilization. Another possibility could be automatic landing.

Similarity to conventional flight controllers makes this concept very appropriate. Joysticks also provide enough space for buttons. Unfortunately, main disadvantage of this concept could be its fragile construction. Pilot is dependent on solid grip and joysticks would not have to be the most suitable option.

13.1.3 Handlebars

Another possibility are conventional handlebars similar to the motorbike ones. This can be considered as safer option since it can be welded directly to the aluminium space frame and carry heavier loads. Pilot would have more confident grip. Following picture depicts proposed handlebars with controller buttons.

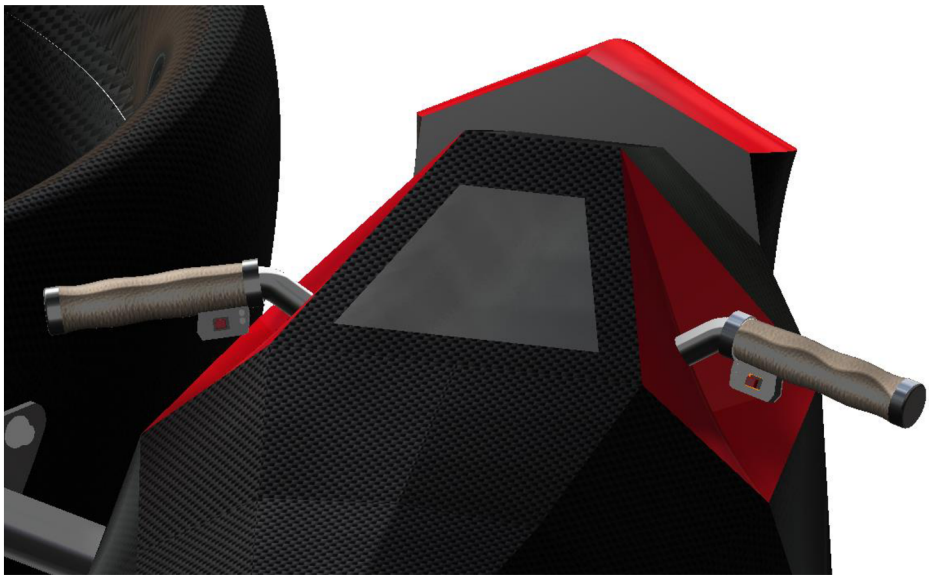

Figure 13.2 Flight control proposal #2 - handlebars

Pilot would have to use his thumb in order to control the multicopter. Concept of flight control would be same as for joysticks but its function would depend only on pilot's finger. This can be considered as disadvantage and this concept would have to be tested and optimized in order to increase ergonomics.

13.2 Sensors

Even though the designed multicopter is controlled by the pilot, who sits on the multicopter and has an overview of the multicopter movement and attitude, it is important to consider including several sensors, which could help the pilot with maneuvering and improve the safety and reliability of flight.

13.2.1 Inertial measurement unit

In order to control aircraft movement, it is nowadays easier to look up for the compact inertial measurement unit (IMU) instead of connecting separate sensors. IMU consists of three axis accelerometer and three-axis gyroscope.[6]

13.2.1.1 Accelerometers

The most common accelerometers used in multicopters are based on MEMS technology. Used accelerometers have to be three-axis to be able measure acceleration in 3D space. Based on the obtained data from accelerometers, angular deviation can be derived. MEMS technology is based on piezoresistive effect or piezoelectric effect. Main advantage of MEMS accelerometers is its low weight and easy implementation to flight control circuit. On the other hand, it is prone to vibrations.[6]

13.2.1.2 Gyroscope

In order to be able to measure angular velocity of the multicopter, gyroscope has to be used. Majority of today gyroscopes is also based on MEMS technology, which is based on Coriolis force principle. Angular deflection results in capacity change, which indicates angular velocity.[6]

13.2.2 Obstacle avoidance

Since the UAM vehicles are expected to operate in the city environment, obstacle avoidance system should be considered. For this purpose, LiDAR sensors could be used since these sensors are able to measure radius of 100 m. These systems are relatively accessible and light, e.g. weigh of the VLP-16 system weights 0.83 kg.[6]

13.2.3 Altitude sensors

Altitude can be measured several ways. Common approach of using Pitot probes require relatively heavy equipment, but offers more accurate results than piezoelectric barometers, which are usually used for multicopters. Performing automatic landing, height above ground has to be measured. For this purpose, ultrasonic sensors may be used. They are based on ultrasonic wave response and may help to perform smooth vertical landing and also provide data during forward flight. Disadvantage of these sensors is its range, which is around 10 m.

14 CONCLUSION

Urban air mobility is a challenging branch of aerospace industry, which is apparently going to emerge even more in the next few years. Control authorities and designers will have to focus on defining more specific regulations, which will make a frequent air traffic safe. In the range of smaller personal UAM platforms already exist plenty of concepts, which were covered in the statistical research. Obtained statistics helped to estimate several parameters, which were useful for the first iteration of the design.

The first important phase of designing process was the choice of propulsion system. Lists of available components were created and out of them were chosen suitable ones based on several criterions. In this phase was made a decision of using contra-rotating propellers, which have several advantages. Besides choosing the propellers, motors and ESCs, proposal of battery pack was created.

Initial idea of flying motorcycle was a supporting element of construction design since the pilot astride. From the beginning it was clear that X configuration of multicopter had to be used. Rotors were placed in the middle vertical position, which combines the benefits of ground effect and safety of the pilot and propulsion system during landing. In order to increase safety of the pilot, propellers were placed into composite ducts, which have also beneficial effect on thrust generation. Central space frame was designed from aluminium circular profiles and was covered by CFRP parts, which has also aesthetic aspect. Internal structure of composite ducts was designed hand in hand with structural analysis.

Strength of the designed multicopter frame was checked by performing FEM analysis. Results showed weak spots and helped to optimize the construction to withstand given load and minimize weight. Aluminium central frame of the multicopter was designed safely and further reduction of weight could be done. However, central frame with the landing gear would be the most loaded part during landing and drop test. From this point of view, landing gear would have to be redesigned and dampers would have to be used. Current design counts with a possibility of guided landing by flight controller. Design of the composite ducts and also their inner structure was also checked for the given load with corresponding high safety factor including possible technological and environmental impacts on laminate. Most critical part of composite duct are mechanical joints, which were secured by an aluminium plate, which helped to increase overall strength of the laminate. Other parts of the duct do not suffer from high stresses. Nevertheless, results of FEM analysis of composite materials are highly dependent on the used material characteristics, which are difficult to predict and in order to obtain the most accurate data, it would require data from testing samples, which are not available during initial phase of design. Two connecting plates in the duct assembly were also checked for their structural strength. Results with higher safety factor showed that these part should be reinforced. However, with conventional safety factor for isotropic materials, these parts can be considered as safely designed.

Flight performance of the multicopter depends on several factors. Since the multicopter is a rotorcraft, influence of ground effect was analysed via CFD simulation. Thrust increment in ground effect was examined in three distances from the ground. Analysis results showed that multicopter flight movement near ground can increase achievable thrust and reduce the power consumption. However, simulation showed highly non-linear behaviour and it would be wise to verify results using transient approach of the simulation. Another aspect which could

influence results was a usage of actuator disks, which neglected the influence of contra-rotating propellers.

In order to calculate forward flight speed dependency on pitch angle and battery endurance, evaluation of multicopter drag had to be performed. Based on the CFD analysis of three different pitch angles, dependency of drag coefficient on pitch angle was created and made forward flight performance calculations possible. Multicopter flight performance met initial requirement of battery endurance, but achievable maximal speed is slightly lower than expected due to the pitch angle limit. Further work could focus on sideward flight and hence estimation of drag coefficients for different roll angles.

Last part covered possible options of flight control. Two proposals of flight controllers were presented together with suitable sensors, which would increasing flight safety. First flight controller variant uses joysticks, which is a better solution from the control point of view but less rigid for pilot's grip. On the other hand, handlebars are more rigid, but controllability could be worse from ergonomic point of view.

15 REFERENCES

[1] LEISHMAN, J. Gordon. Principles of helicopter aerodynamics. Second edition. Cambridge: Cambridge University Press, 2008. Aerospace Series (Cambridge). ISBN 978-1-107-01335-3

[2] Curtiss-Wright VZ-7. Wikipedia: the free encyclopedia [online]. San Francisco (CA): Wikimedia Foundation, 2021, 2021 [cit. 2021-11-22]. Available from: https://en.wikipedia.org/wiki/Curtiss-Wright_VZ-7

[3] EASA a MCKINSEY & COMPANY. Study on the societal acceptance of Urban Air Mobility in Europe. EASA Report [online]. 2021, 19th May 2021, , 162 [cit. 2021-11-23]. Available from: https://www.easa.europa.eu/sites/default/files/dfu/uam-full-report.pdf

[4] PATTERSON, Michael D., Kevin R. ANTCLIFF a Kohlman LEE W. A Proposed Approach to Studying Urban Air Mobility Missions Including an Initial Exploration of Mission Requirements. Annual Forum and Technology Display. Phoenix, AZ, USA: NASA, 14 May 2018n. l., 19. NASA report number: NF1676L-28586.

[5] NEXTGEN OFFICE, FAA, US DEPARTMENT OF TRANSPORTATION. Concept of Operations: Urban Air Mobility (UAM). V1.0. Washington DC: FAA, US Department of Transportation, 2020, 49 s. Available at: https://nari.arc.nasa.gov/sites/default/files/attachments/UAM_ConOps_v1.0.pdf

[6] QUAN, Quan. *Introduction to Multicopter Design and Control*. Imprint: Springer, 2017. ISBN 9789811033827.

[7] Assen Aerospace A2 Avenger. THE VERTICAL FLIGHT SOCIETY. Electric VTOL News: Assen Aerospace A2 Avenger [online]. [cit. 2022-04-02]. Available from: https://evtol.news/assen-aerospace-a2-avenger/

[8] Hover Scorpion. Electric VTOL News [online]. Virginia, USA: The Vertical Flight Society [cit. 2022-04-02]. Available at: https://evtol.news/hoversurf-scorpion/

[9] EUROPEAN UNION AVIATION SAFETY AGENCY. Second Publication of Proposed Means of Compliance with the Special Condition VTOL. MOC-2 SC-VTOL. EASA, 2021, 94 s. Available at: https://www.easa.europa.eu/downloads/128938/en

[10] EUROPEAN UNION AVIATION SAFETY AGENCY. Special Condition for small-category VTOL aircraft. SC-VTOL-01. EASA, 2019, 31 s. Available from: https://www.easa.europa.eu/sites/default/files/dfu/SC-VTOL-01.pdf

[11] Certification Specifications, Acceptable Means of Compliance and Guidance Material for Small Rotorcraft: CS-27. Amendment 9. EU: EASA, 17 December 2021 1n. l.

[12] BICZYSKI, Marcin, Rabia SEHAB, James F. WHIDBORNE, Guillaume KREBS a Patrick LUK. Multirotor Sizing Methodology with Flight Time Estimation. Journal of Advanced Transportation. Wiley Online Library, vol.2020(9689604), 14. ISSN 01976729. Available at: https://doi.org/10.1155/2020/9689604

[13] MAISEL, Martin D., Demo J. GIULIANETTI a Daniel C. DUGAN. The History of The XV-15 Tilt Rotor Research Aircraft: From Concept to Flight. NASA, Office of Policy and Plans, NASA History Division, Washington DC: NASA, 2000, 222 s. The NASA History Series: Monographs in Aerospace History #17: Monographs in Aerospace History #17, NASA SP-2000-4517. ISBN 1493648683. Available from: https://www.researchgate.net/publication/24295050_The_History_of_the_XV-15_Tilt_Rotor_Research_Aircraft_from_Concept_to_Flight

[14] Are more propeller blades better? Hartzell propeller [online]. One Propeller Place, Piqua, Ohio, USA: Hartzell propeller, 2015, 28th August 2018 [cit. 2021-11-24]. Available from: https://hartzellprop.com/are-more-propeller-blades-better/

[15] VEPA, Ranjan. Electric aircraft dynamics: A systems engineering approach. Broken Sound Parkway NW, Suite 300, Boca Raton: CRC Press, 2020. ISBN 978-0367194246.

[16] MILLETT, Pete. Brushless Vs Brushed DC Motors: When and Why to Choose One Over the Other. Monolithic Power Systems [online]. Monolithic Power Systems, 2021 [cit. 2021-11-24]. Available at: https://www.monolithicpower.com/en/brushless-vs-brushed-dc-motors

[17] ESTINGOY, Lee. Inside the Electronic Speed Control. Model Aviation [online]. Academy of Model Aeronautics, 2022, 2010 [cit. 2022-04-03]. Available from: https://www.monolithicpower.com/en/brushless-vs-brushed-dc-motors

[18] DEJAN. How Brushless Motor and ESC Work. How to Mechatronics [online]. [cit. 2022-04-03]. Available at: https://howtomechatronics.com/how-it-works/how-brushless-motor-and-esc-work/

[19] PIERRI, Erika, Valentina CIRILLO, Thomas VIETOR a Marco SORRENTINO. Adopting a Conversion Design Approach to Maximize the Energy Density of Battery Packs in Electric Vehicles. Energies. MDPI, 2021. ISSN 1996-1073. Available from: doi:https://doi.org/10.3390/en14071939

[20] BOHORQUEZ, Felipe. *Rotor Hover Performance and System Design of an Efficient Coaxial Rotary Wing Micro Air Vehicle*. Maryland, College Park, 2007. Dissertation. Faculty of the Graduate School of the University of Maryland. directed by Prof. Darryll Pines.

[21] GUR, Ohad, Jonathan SILVER, Radovan DÍTĚ a Raam SUNDHAR. Optimal Design of Hovering Contra-Rotating Propulsion System. AIAA SCITECH 2022 Forum. Reston, Virginia: American Institute of Aeronautics and Astronautics, 2022, 2022-01-03, -. ISBN 978-1-62410-631-6.Available at: doi:10.2514/6.2022-0145

[22] LEI, Yao, Yue BAI, Zhijun XU, Qingjia GAO a Changjun ZHAO. An experimental investigation on aerodynamic performance of a coaxial rotor system with different rotor spacing and wind speed. *Experimental Thermal and Fluid Science*. Elsevier, 2013, **44**, 779-785. ISSN 0894-1777.

[23] WEI, Zhang, Fan NINGJUN, Wang ZHENGJIE a Wu YANXUAN. Modeling and Aerodynamic Analysis of a Ducted-Fan Micro Aerial Vehicle. International Conference on Modelling, Identification and Control [online]. Wuhan, China, 2012, 2012 [cit. 2022-04-03].

[24] AKTURK, Ali and Cengiz CAMCI. Tip Clearance Investigation of a Ducted Fan Used in VTOL UAVS: Part 1—Baseline Experiments and Computational Validation. Volume 7: Turbomachinery, Parts A, B, and C [online]. ASMEDC, 2011, 2011-01-01, 331-344 [cit. 2022-04-03]. ISBN 978-0-7918-5467-9. Available from: doi:10.1115/GT2011-46356

[25] BAILIE, J. A, R. P. LEY and A. PASRICHA. A SUMMARY AND REVIEW OF COMPOSITE LAMINATE DESIGN GUIDELINES: NASA Contract NAS1-19347. Final Report. Hampton, Virginia: NASA, 1997. NAS1-19347.

[26] GALIŃSKA, Anna and Cezary GALIŃSKI. Mechanical Joining of Fibre Reinforced Polymer Composites to Metals—A Review. Part II: Riveting, Clinching, Non-Adhesive Form-Locked Joints, Pin and Loop Joining. Polymers [online]. 2020, 12(8) [cit. 2022-04-03]. ISSN 2073-4360. Available at: doi:10.3390/polym12081681

[27] CAMANHO, P.P., C.M.L. TAVARES, R. DE OLIVEIRA, A.T. MARQUES a A.J.M. FERREIRA. Increasing the efficiency of composite single-shear lap joints using bonded inserts. Composites Part B: Engineering [online]. 2005, 36(5), 372-383 [cit. 2022-04-03]. ISSN 13598368. Available at: doi:10.1016/j.compositesb.2005.01.007¨

[28] CAMANHO, P.P., A. FINK, A. OBST a S. PIMENTA. Hybrid titanium–CFRP laminates for high-performance bolted joints. Composites Part A: Applied Science and Manufacturing [online]. 2009, 40(12), 1826-1837 [cit. 2022-04-03]. ISSN 1359835X. Available at: doi:10.1016/j.compositesa.2009.02.010

[29] LIU, G.R, S. S QUEK and G R LIU. *Finite Element Method*. Oxford: Elsevier Science & Technology, 2003. ISBN 0750658665. Available at: doi:10.1016/B978-0-7506-5866-9.X5000-2

[30] ASM HANDBOOK COMMITTEE. ASM Handbook Volume 2: Properties and Selection: Nonferrous Alloys and Special-Purpose Materials. Volume 2. ASM International, 1990. ISBN 978-0-87170-378-1.

[31] JONES, Robert M. Mechanics of Composite Materials. 2nd Edition. Boca Raton: Taylor & Francis Group, 2018. ISBN 9781315272986.

[32] BAKER, Alan, Stuart DUTTON a Donald KELLY. Composite Materials for Aircraft Structures. 3rd edition. AIAA American Institute of Aeronautics & Ast, 2016. ISBN 978-1624103261.

[33] COLLINGS, T. A. a STRUCTURES DEPT., R.A.E., FARNBOROUGH HUNTS. The Strength of Bolted Joints in Multi-Directional CFRP Laminates. *ERONAUTICAL RESEARCH COUNCIL CURRENT PAPER*. London: PROCUREMENT EXECUTIVE, MINISTRY OF DEFENCE, **I977**(Cp. 1380), 75.

[34] HEIMBS, Sebastian, Sebastian SCHMEER, Jörg BLAUROCK a Stefan STEEGER. Static and dynamic failure behaviour of bolted joints in carbon fibre composites. Composites Part A: Applied Science and Manufacturing. 2013(Volume 47), 91-101. Available from: https://doi.org/10.1016/j.compositesa.2012.12.003

[35] TU, Jiyuan, Guan Heng YEOH a Chaoqun LIU. Computational fluid dynamics: a practical approach. Third edition. Oxford: Butterworth-Heinemann, [2018]. ISBN 978-0081011270.

[36] ALEXANDROV, V.L. Letecké vrtule. Praha: Statní Nakladatelství Technické Literatury, 1954.

[37] ANEIROS, Eva, David LOBO, Alberto LOPEZ a Roberto ALVAREZ. A proposed mathematical model for discharge curves of Li-Ion batteries. *2013 International Conference on New Concepts in Smart Cities: Fostering Public and Private Alliances (SmartMILE)*. IEEE, 2013, 2013, 1-6. ISBN 978-1-4799-2911-5. Available from: doi:10.1109/SmartMILE.2013.6708177

[38] Holybro Pixhawk 5X. PX4 User Guide [online]. Pixhawk, 2008, 23.3. 2022, 6:31:04 AM [cit. 2022-05-20].
Available at: https://docs.px4.io/master/en/flight_controller/pixhawk5x.html

16 Symbols and abbreviations

Roman letters

Symbol	Unit	Explanation
A	-	Propeller aspect ratio
B_p	-	Number of propeller blades
C_b	kWh or Ah	Battery capacity
C_{min}	kWh or Ah	Minimal battery capacity
c_D	-	Drag coefficient
c_T	-	Thrust coefficient
c_M	-	Torque coefficient
D	N	Drag
D_p	m	Propeller diameter
DL	kg·m^{-2}	Disk loading
e	-	Oswald factor
E	MPa	Elastic modulus of isotropic material
E_1	MPa	Elastic modulus parallel to fibres
E_2	MPa	Elastic modulus traverse to fibres
FI	-	Failure index
G	N	Gravity
G_{12}	GPa	Shear modulus
G_{ϕ_t}	Nm	Gyroscopic moment of top propeller
G_{ϕ_b}	Nm	Gyroscopic moment of bottom propeller
$G_{\phi_{Ut}}$	Nm	Ultimate gyroscopic moment of top propeller
$G_{\phi_{Ub}}$	Nm	Ultimate gyroscopic moment of bottom propeller
H_p	m	Propeller pitch
I_b	A	Battery electric current
I_m	A	Motor electric current
J_p	kg·m^2	Propeller moment of inertia
M	Nm	Torque
M_U	Nm	Loading torque
$MTOW$	kg	Maximal Take-Off Weight
n	-	Load factor
N	RPM	Rotational speed
P_e	W	Electric power
P_{iron}	W	Motor internal power
P_{prop}	W	Propeller mechanical power
R	km	Forward flight range
RF	-	Reserve factor
R_{im}	Ω	Motor internal resistence
R_m	MPa	Ultimate strenght
R_e	MPa	Yield strenght
t	s	Time
t_B	min	Battery endurance
T_p	N	Propeller thrust
T_{req}	kgf	Minimal required thrust
U_m	V	Motor voltage
V_{TOSS}	m·s^{-1}	Take-off safety speed
V_{FF}	m·s^{-1}	Forward flight speed

Greek letters

Symbol	Unit	Explanation
α_0	°	Correction angle
γ		Correction angle
θ	°	Pitch angle
λ	-	Correction coefficient
ρ	$kg \cdot m^{-3}$	Air density
σ_v	MPa	Von Mises strength
σ_{PtL}	MPa	Longitudinal tensile stress
σ_{PcL}	MPa	Longitudinal compressive stress
σ_{PtT}	MPa	Traverse tensile stress
σ_{PcT}	MPa	Traverse compressive stress
ω_p	$rad \cdot s^{-1}$	Propeller rotational speed
ω_θ	$rad \cdot s^{-1}$	Pitching precession speed

Abbreviations

BLDC	Brushless Direct Current
CFD	Computational Fluid Dynamics
CFRP	Carbon Fibre Reinforced Polymer
ConvTO	Conventional Take-Off
EASA	European Union Aviation Safety Agency
ESC	Electronic Speed Controller
FAA	Federal Aviation Administration
FEM	Finite Element Method
GNNS	Global Navigation Satellite System
IGE	In Ground Effect
LiDAR	Light Detection And Ranging
MEMS	Micro Electro Mechanical Systems
MTOW	Maximal Take-Off Weight
MPC	Multiple Point Constraint
NASA	National Aeronautics and Space Administration
PAV	Personal Aerial Vehicle
PWM	Pulse Width Modulation
SF	Safety Factor
RBE	Rigid Body Element
RF	Reserve Factor
UAM	Urban Air Mobility
UAS	Unmanned Aircraft Systems
VTOL	Vertical Take-Off and Landing

17 APPENDIX

17.1 List of component weights and positions of CoG

Table 17.1 Component weights and position of CoG with different payloads

Part number	Part name	Estimated weight [kg]	x[mm]	y [mm]
1	Frame	18.29	1133.3	159.9
2	Covering	10.1	1070.0	162.7
3	Landing gear	4.52	1031.8	650.3
4	Propeller duct front left	11.36	0.0	36.8
5	Propeller duct front right	11.36	0.0	36.8
6	Propeller duct rear left	11.36	2000.0	36.8
7	Propeller duct rear rear	11.36	2000.0	36.8
12	Motor Front Upper left	3.6	0.0	60.0
13	Motor Front Bottom left	3.6	0.0	-60.0
14	Motor Front Upper rear	3.6	0.0	60.0
15	Motor Front Bottom rear	3.6	0.0	-60.0
16	Motor Rear Upper left	3.6	2000.0	60.0
17	Motor Rear Bottom left	3.6	2000.0	-60.0
18	Motor Rear Upper rear	3.6	2000.0	60.0
19	Motor Rear Bottom rear	3.6	2000.0	-60.0
20	Propeller Front upper left	0.35	0.0	110.0
21	Propeller Front bottom left	0.35	0.0	-110.0
22	Propeller Front top right	0.35	0.0	110.0
23	Propeller Front bottom right	0.35	0.0	-110.0
24	Propeller Rear upper left	0.35	2000.0	110.0
25	Propeller Rear bottom left	0.35	2000.0	-110.0
26	Propeller Rear top right	0.35	2000.0	110.0
27	Propeller Rear bottom right	0.35	2000.0	-110.0
28	Flight controller + avionics	0.4	510.0	-20.0
29	ESC Front left Top	0.58	523.0	55.0
30	ESC Front left Bottom	0.58	523.0	55.0
31	ESC Front right Top	0.58	523.0	55.0
32	ESC Front right bottom	0.58	523.0	55.0
33	ESC Rear left top	0.58	1750.0	60.0
34	ESC Rear left bottom	0.58	1750.0	60.0
35	ESC rear right top	0.58	1750.0	60.0
36	ESC rear right bottom	0.58	1750.0	60.0
37	Battery	105	895.7	278.3
38	Pilot 100 kg	100	1076.2	262.0
	Pilot 85 kg	85	1076.2	262.0
	Pilot 60 kg	60	1076.2	262.0
	Total weight (pilot 100 kg)	320	1001	203
	Total weight (pilot 85 kg)	296	1027	206
	Total weight (pilot 60 kg)	280	991	194

17.2 Lay up of composite parts

Table 17.2 Duct shell layup

Ply number	Material	Thickness [mm]	Orientation [°]
1	CFRP	0.32	+45
2	CFRP	0.32	-45
3	CFRP	0.32	0
4	CFRP	0.32	-45
5	CFRP	0.32	+45

Table 17.3 Rim of omega beam layup

Ply number	Material	Thickness [mm]	Orientation [°]
1	CFRP	0.32	+45
2	CFRP	0.32	-45
3	CFRP	0.32	0
4	CFRP	0.32	0
5	CFRP	0.32	-45
6	CFRP	0.32	+45
7	CFRP	0.32	+45
8	CFRP	0.32	-45
9	CFRP	0.32	0
10	CFRP	0.32	-45
11	CFRP	0.32	+45

Table 17.4 Omega profile flange layup

Ply number	Material	Thickness [mm]	Orientation [°]
1	CFRP	0.32	+45
2	CFRP	0.32	-45
3	CFRP	0.32	0
4	CFRP	0.32	0
5	CFRP	0.32	-45
6	CFRP	0.32	+45

Table 17.5 Omega profile web layup

Ply number	Material	Thickness [mm]	Orientation [°]
1	CFRP	0.32	+45
2	CFRP	0.32	-45
3	CFRP	0.32	0
4	CFRP	0.32	0
5	CFRP	0.32	-45
6	CFRP	0.32	+45
7	CFRP	0.32	+45
8	CFRP	0.32	-45
9	CFRP	0.32	0
10	CFRP	0.32	0
11	CFRP	0.32	-45
12	CFRP	0.32	+45

Table 17.6 Motor connector layup

Ply number	Material	Thickness [mm]	Orientation [°]
1	CFRP	0.32	+45
2	CFRP	0.32	-45
3	CFRP	0.32	0
4	CFRP	0.32	90
5	CFRP	0.32	90
6	CFRP	0.32	0
7	CFRP	0.32	-45
8	CFRP	0.32	+45

Table 17.7 Inner surface rim reinforcement

Ply number	Material	Thickness [mm]	Orientation [°]
1	CFRP	0.32	+45
2	CFRP	0.32	-45
3	CFRP	0.32	0
5	CFRP	0.32	-45
6	CFRP	0.32	+45
7	CFRP	0.32	90
8	Al 7075	3	-
9	CFRP	0.32	90
10	CFRP	0.32	+45
11	CFRP	0.32	-45
12	CFRP	0.32	0
13	CFRP	0.32	0
14	CFRP	0.32	-45
15	CFRP	0.32	+45

17.3 Static pressure distribution at ground effect (symmetry plane)

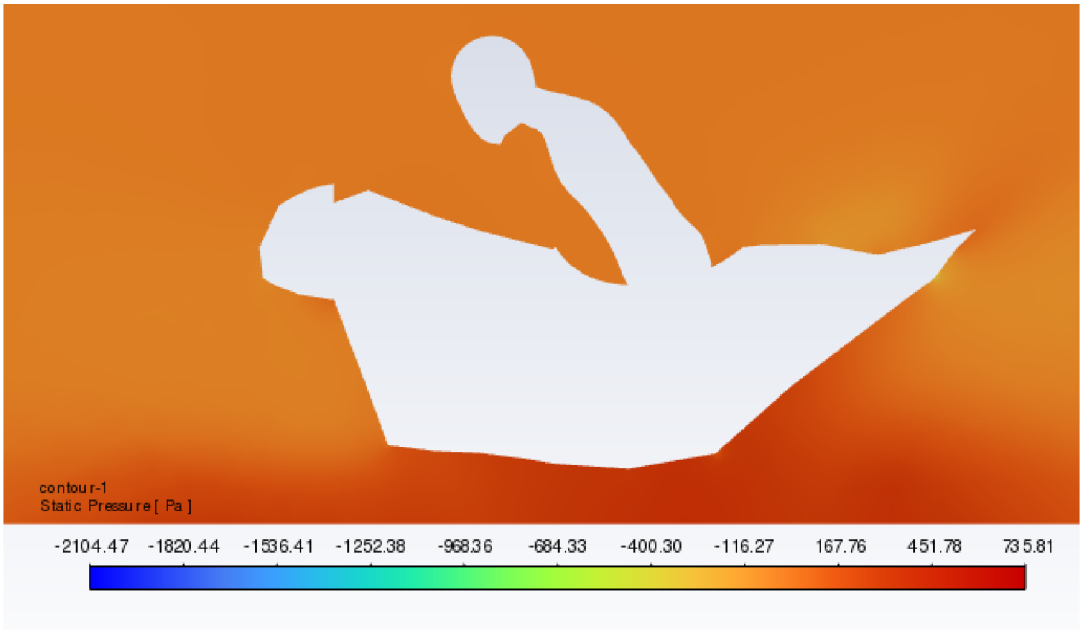

Figure 17.1 Static pressure distribution at 0 m above ground (symmetry plane)

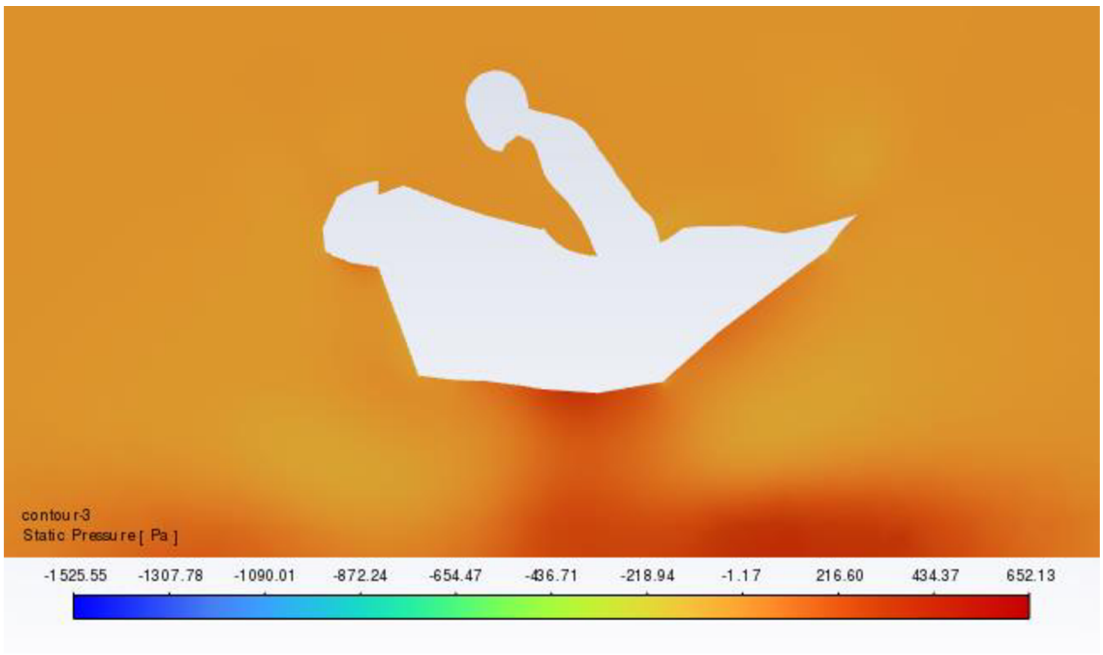

Figure 17.2 Static pressure distribution at 0.5 m above ground (symmetry plane)

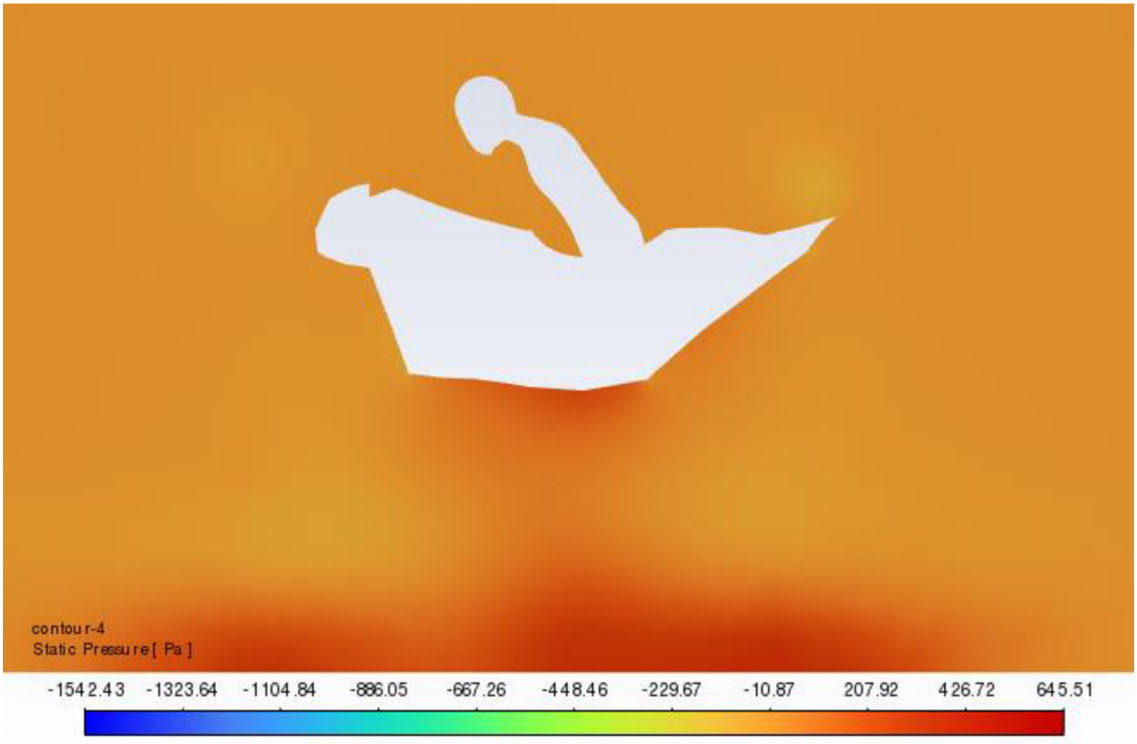

Figure 17.3 Static pressure distribution at 1 m above ground (symmetry plane)